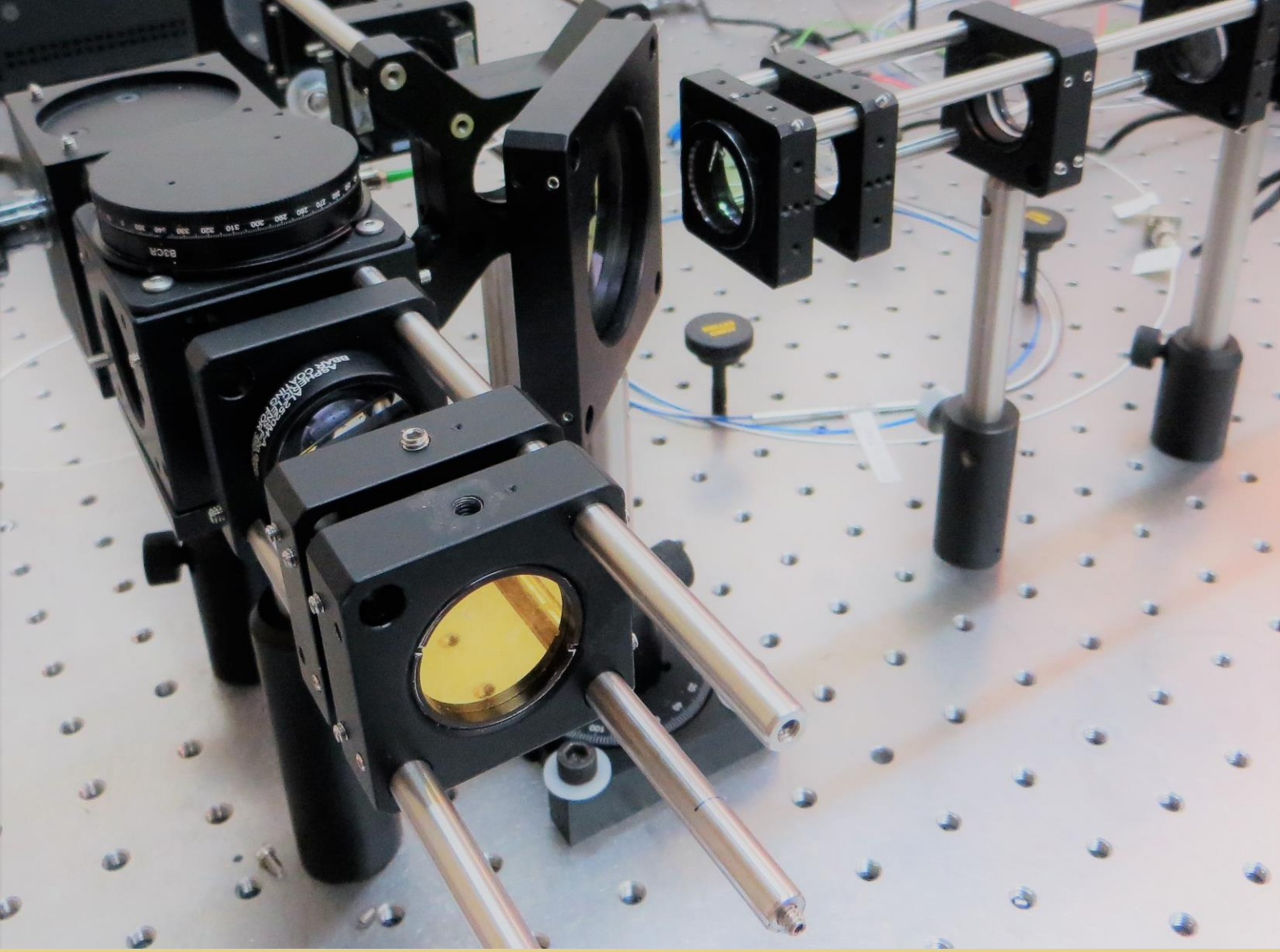

Andoni Calvo y Santos

DEVELOPMENT OF AN IMAGE CAPTATION SYSTEM USING SIMPLE REFLECTIVITY AND SCANNING CONTROL IMPROVEMENTS IN SS-OCT

Master's degree dissertation in Physics Engineering under the supervision of Professor José Paulo Domingues and Professor Rui Bernardes, presented at the Department of Physics of the Faculty of Sciences and Technology of the University of Coimbra

September 2017

· U C ·

UNIVERSIDADE DE COIMBRA

Abstract

Optical Coherence Tomography (OCT) is a technology commonly used in medical fields for diagnosis and research. It allows to retrieve data *in vivo* about the 3-dimensional structure of a translucent sample, such as the human eye. The resolution of the structural data is typically under 10 μm.

An OCT device dedicated to imaging the eyes of small animals for research purposes is currently under active development at IBILI. The work hereby presented is integrated in the development of this system, as it is a step forward toward improving its performance and usability.

The purpose of this work is on the implementation of two improvements to the existing setup. The first is the creation of a module to enable previewing the target area of the OCT in real time, ideally being able to see the retinal fundus of the small animals to be studied. This would greatly improve the current process to aim the OCT and align the targets with the apparatus. The second improvement is the integration of the module developed to replace the current control system for the positioning of the OCT beam.

Acknowledgements/Agradecimentos

Em primeiro lugar gostaria de agradecer aos professor José Paulo Domingues e Rui Bernardes pela oportunidade de trabalhar neste projecto e por todos os incentivos e orientação no desenvolvimento deste trabalho.

Ao professor Miguel Morgado e à Susana Silva, pela ajuda e informações que tiveram a gentileza de providenciar quando precisei.

Ao professor Custódio Loureiro, pela partilha de conhecimentos relativamente ao trabalho que desenvolveu para este projecto, e pela disponibilidade para ajudar na resolução de problemas.

À Quantunna e aos elementos com quem tive o prazer de partilhar palcos e histórias, por tudo o que proporcionaram e ensinaram no decorrer da minha passagem por lá.

Aos meus colegas de casa, Daniel Mano, Diogo Figueiredo, Emanuel Barata e Xavier Carvalho, pela amizade e pela paciência que demonstraram para comigo enquanto vivemos juntos.

Ao Mário Ribeiro, pela amizade e pelos bons conselhos.

Ao Luís Antunes e à Natacha Leite, pela ajuda com a tese e por todos os bons momentos.

Ao André Gonçalves, pela amizade e companhia ao longo de todos estes anos.

À minha família, pelo apoio incondicional.

Aos meus pais, pelo esforços que fazem diariamente, por tudo o que me ensinaram e por me terem ajudado a tornar quem sou.

À Rita, por tornar os dias mais agradáveis.

Contents

Contents v

List of Acronyms ix

List of Figures xi

1 Introduction 1
1.1 Motivation . . . 1

2 Optical Coherence Tomography 3
2.1 Historical overview . . . 3
2.2 The Michelson interferometer . . . 8
2.3 Physical principles . . . 9
2.3.1 Interference . . . 9
2.3.2 Coherence . . . 12
2.3.3 Interaction of Light with Matter . . . 14
2.4 Optical Coherence Tomography . . . 17
2.4.1 Time Domain OCT . . . 19
2.4.2 Spectral Domain OCT . . . 22
2.4.3 Swept-Source OCT . . . 23
2.5 OCT scans . . . 23
2.6 Performance Parameters . . . 25
2.6.1 Axial Resolution . . . 25
2.6.2 Lateral Resolution . . . 25
2.6.3 Depth of Field . . . 26
2.6.4 Signal to Noise Ratio . . . 27
2.6.5 Sensitivity . . . 27
2.6.6 Dynamic Range . . . 27
2.7 Imaging Speed . . . 27
2.8 OCT Comparison . . . 28
2.9 State of the Art . . . 28

3 Experimental setup **31**
3.1 Initial Setup . . . 31
3.2 Laser source . . . 33
3.3 Balanced detector . . . 36
3.4 DAQ board . . . 38
3.5 Galvanometer Scanning System . . . 40
3.6 Deprecated devices . . . 42
3.6.1 Signal generator . . . 42
3.6.2 Digital delay and Pulse generator . . . 42

4 Illumination and camera module **45**
4.1 Options considered . . . 45
4.1.1 Existing setup . . . 45
4.1.2 Infra-Red Camera . . . 45
4.1.3 Near-camera lighting with Color Camera . . . 46
4.1.4 Near-target lighting with Color Camera . . . 47
4.1.5 Perpendicular lighting with Color Camera . . . 47
4.2 Experimental setup . . . 48
4.2.1 Thorlabs DMLP950 . . . 50
4.2.2 Thorlabs AL2520M-A . . . 50
4.2.3 Edmund Optics IR Cut-Off Filter . . . 52
4.2.4 Melles Griot Non-Polarizing Plate Beamsplitter 03BTL023 53
4.2.5 Microsoft® LifeCam VX-500 . . . 54
4.2.6 Mounted Lens Kits . . . 56
4.3 sec:arlens . . . 57
4.4 Testing and Performance . . . 58
4.5 Impact on the OCT . . . 61

5 Control Module **65**
5.1 General description . . . 66
5.2 Operation . . . 67
5.3 Usage . . . 69
5.4 Improvements . . . 72

6 Software Integration **75**
6.1 Data acquisition and reconstruction . . . 76
6.1.1 Direction tracking . . . 76
6.1.2 Unmatched sequential B-Scans . . . 81
6.2 Galvanometer control . . . 87
6.3 Live preview . . . 92

7 Conclusions **97**
7.1 Future Work 98

Bibliography **101**

List of Acronyms

CMMR Common Mode Rejection Ratio.

DAC Digital-Analog Converter.

DAQ Digital Acquisition.

FD-OCT Fourier Domain Optical Coherence Tomography.

FFT Fast Fourier Transform.

FWHM Full-Width at Half-Maximum.

IBILI Institute for Biomedical Imaging and Life Sciences.

IFT Inverse Fourier Transform.

IR Infra-Red.

LED Light Emitting Diode.

MPSSE Multi-Protocol Synchronous Serial Engine.

MTF Modulation Transfer Function.

OCT Optical Coherence Tomography.

OpenCV Open Source Computer Vision Library.

PSF Point Spread Function.

SD-OCT Spectral Domain Optical Coherence Tomography.

SNR Signal to Noise Ratio.

SS-OCT Swept-Source Optical Coherence Tomography.

TD-OCT Time Domain Optical Coherence Tomography.

List of Figures

2.1 First optical coherence tomograph and corresponding histological section . . . 6
2.2 Michelson interferometer diagram and typical interference pattern . . . 9
2.3 Superimposed Waves . . . 10
2.4 Light absorption in water . . . 15
2.5 Diagram of a Time Domain OCT . . . 19
2.6 Optical Coherence Tomography (OCT) signal examples . . . 21
2.7 Diagram of a Spectral Domain OCT . . . 22
2.8 Depth of field, NA and lateral resolution . . . 26

3.1 Initial OCT Setup . . . 32
3.2 Laser Source Optical Power Spectrum . . . 35
3.3 Laser source Trigger, optical power and Clock signal . . . 36
3.4 PDB145C wavelength response . . . 37

4.1 Camera and illumination diagram . . . 48
4.2 Transmission and reflectance curves for the DMLP950 . . . 51
4.3 Transmission curve for the IR filter . . . 53
4.4 Transmission curve of the Melles Griot Non-Polarizing Plate Beamsplitter 03BTL023 . . . 55
4.5 Zemax diagram of the light focusing lenses . . . 57
4.6 Zemax diagram of the camera's zoom lenses . . . 58
4.7 Modulation transfer function of the system . . . 60
4.8 Plot and histogram of luminous intensities through a reflection free area of the target . . . 61
4.9 Plot and histogram of luminous intensities through an area of the target containing reflections . . . 62
4.10 Histogram of luminous intensities in the whole testing image . 62

5.1 General architecture of the control module . . . 67

5.2 Scanning waveforms generated by the control module 68
5.3 Laser Source Optical Power Spectrum 71

6.1 Part of two sequentially acquired B-Scans of a solid, opaque reflecting surface from a coin. The one from the top, a), was acquired first, and corresponds to an odd B-scan. The bottom image, b), corresponds to an even B-Scan, acquired while the galvanometer is scanning in backward toward its initial position. A clear lateral shift can be seen between the two. 81
6.2 Rotations on a line of colored pixels 82
6.3 Rotations on a matrix of colored pixels 82
6.4 Expected behavior when acquiring consecutive B-Scans. 83
6.5 Observed behavior when acquiring consecutive B-Scans. 83
6.6 User interface of the OCT software 91

1 | Introduction

This chapter provides an overview on the general contents and structure of this thesis, the motivation behind the work done and the main objectives of this work.

1.1 Motivation

Optical Coherence Tomography (OCT) is a technology which allows three-dimensional optical imaging of the structures of translucent samples by measuring the interference pattern generated from the superposition of the reflection of a light beam incident on the sample with a beam reflected by a reference mirror. This technology is nowadays commonly used in several medical fields, particularly in ophthalmology, due to the translucent nature of the human eye.

An OCT system for studying the eyes of small animals has been under development at the Institute for Biomedical Imaging and Life Sciences (IBILI) for the past few years. The system is currently operational, but still requires further work and improvement in order to achieve the same degree of usability as currently available systems. Two important steps toward this goal are the implementation of a real-time targeting system and the creation of an alternative control module as an alternative to the current unpractical control setup.

A real time targeting system is an important addition to the OCT system, as it is very difficult to properly target the OCT laser beam to the proper area without having any feedback. This is particularly true for small animals, as the size of their eyes are only a few millimeters wide. Accurately aiming at the desired area can be a time consuming and inaccurate process, and it is almost impossible to target a particular area inside the eye without proper feedback.

The currently implemented control setup for the laser positioning system heavily relies on manual intervention. Such a dependence is undesirable,

as it makes the process of setting up the system take longer, particularly due to the constant need of fine-tuning some parameters. In addition, the positioning system is not currently set up for working at its full speed, which could be solved by changing the way it is controlled.

The objectives of this work are twofold:

- The development of a real time previewing system for the target area of the OCT, easily accessible through the software installed on the system's host computer;
- The testing and integration of a new module responsible for controlling the positioning system and synchronizing it with the laser source and the acquisition system.

The structure of this document is as follows:

- Chapter one describes the scope of the work and the document structure;
- Chapter two provides an historical overview of OCT, an introduction to the concepts of OCT, a description of relevant physical phenomena and describes the current state of the art on commercial OCT systems.
- Chapter three presents the initial setup used at IBILI, its working process, a description of the used hardware and components, and an explanation of why some of them were replaced.
- Chapter four focuses on the implementation of the live preview of the target area of the OCT, a module responsible for illuminating the target and streaming images from it to the host computer;
- Chapter five presents a module to replace the current setup for controlling the positioning system. This was not developed in this work, but is nonetheless relevant information, as it helps to better understand the changes in operation and the adjustments needed on the software to integrate this module;
- Chapter six focuses on the integration of the changes made to the OCT system with the software on the host pc;
- Chapter seven discusses the conclusions of this work, and future work that should be done in the future;

2 | Optical Coherence Tomography

Optical Coherence Tomography (OCT) is an imaging technique which provides high resolution imaging of the structure of a non-homogeneous sample based on the refraction index of its layers. It is capable of obtaining cross-sectional or 3-D representations of the sample with a typical accuracy of a few μm.

In order to understand this technology several topics need to be addressed. Firstly, a brief history of the ideas and works that led to the development and evolution of OCT will be presented, along with the usefulness and applications of this technology nowadays. The Michelson Interferometer is then briefly introduced, as understanding its workings provides a relatively simple introduction to interferometry, and it is intuitive to compare it to OCT. Next, a few physical concepts and phenomena fundamental to understanding OCT will be explored. Before entering a technical explanation about the process by which OCT works, an overview of the data it usually provides and the different types of scans will be presented. With all the necessary concepts established, the different modalities of OCT can finally be approached with reasonable understanding. To end this chapter, the strengths and weaknesses of these modalities are compared, and the current capabilities of existing state of the art machines are presented.

2.1 Historical overview

In 1971, Duguay and Mattick [21] proposed for the first time using optical echoes in order to see through biological tissue. Using an ultrafast shutter based on the Kerr effect, which was able to achieve picoseconds or femtosecond speeds, it was possible to obtain pictures of ultra short light pulses "in flight", while propagating through a water and milk solution. The authors were able to achieve a resolution of about 1 mm, and it was suggested that seeing through human skin could be feasible using subpicosecond pulses, allowing submillimeter resolution. However, it required high intensity laser

pulses to work, a very undesirable requirement.

Bruckner [13] was later able to achieve a resolution of 0.5 μm on the study of cataract microstructure of an albino rabbit *in vivo*, by using picosecond range-gated light scattering. Light pulses of approximately 10 ps were used to illuminate the eye. The backscattered light was collected at several angles by an array of fiber optics and sequentially sampled by a multichannel picosecond Kerr shutter. Only pulses scattered from the desired depth in the eye were transmitted, blocking anything from the foreground or background.

In the following years, several techniques were developed for optical range gating using nonlinear cross correlation, gated amplification and others. However, light pulses with very high temporal resolution were needed for investigations in biological and medical systems. Taking advantage of advances made in the generation of ultrashort laser pulses, Fujimoto et al. [29] proposed in 1986 the use of femtosecond laser pulses to perform optical ranging using nonlinear cross-correlation gating as a way to investigate the optical properties and microstructure of biological systems. In this approach, a reference beam is cross-correlated with the sample pulses by focusing with a crossed-beam geometry into an anglephase-matched potassium dihydrogen phospate second harmonic generator crystal. Measuring the integrated second harmonic energy as a function of the temporal delay between the signal and reference provides the cross-correlation. A resolution of approximately 15 μm was obtained using pulses with an approximate duration of $65fs$. This setup was used to perform an *in vivo* study on the eyes of rabbits as an example of its usage in transparent media, and to perform measurements on a sample of human skin *in vitro* to test its performance in nontransparent media. Sensitivities of $-70dB$ were achieved, which was still rather far from satisfactory.

In 1988, Fercher et al. [27] published the first application of low-coherence interferometry to the imaging of biological tissues, in order to achieve noninvasive measurement of human eye length. Low-coherence interferometry was already used in photonics to measure optical echoes and backscattering in optical fibers and waveguides [28]. This is where research started turning in the direction that would come to produce OCT, as the OCT is, in a way, an extension of low-coherence interferometry.

Interferometry is a technique which correlates the light backscattered from a sample with a known reference that travels a well defined path. The Michelson interferometer, used originally to detect potential differences in the relative speed of light [54], is the precursor of modern interferometry, and is described in Section 2.2. A lengthier explanation of this device and the interference phenomenon is also included in Sections 2.2 and 2.3.1.

Fercher et al. [27] were able to determine the axial length of the eye

with a precision of 0.03 mm, comparable to results obtained with acoustic instruments. They suggest that results could potentially be improved with a lower coherence length, as long as it retained good spatial coherence.

Soon after, in 1991, OCT Huang et al. [40] announced the development of a technique called Optical Coherence Tomography which allowed non-invasive cross-sectional imaging in biological systems. OCT used low-coherence interferometry to create bidimensional images of both transparent and highly optically scattering media. This was demonstrated with *in vitro* samples of tissue from both the retina and the coronary artery, which are medically relevant examples of transparent and turbid media.

The authors describe the OCT as an extension of the low-coherence reflectometer [33], which used the coherence data to find information about the time-of-flight delay from the backscattering sites in the sample. The reference arm is mobile, allowing to vary the delay between the beam reflected from the sample and the reference mirror. This mobility is then used to determine the location of backscattering sites on the sample, by knowing that interference can only occur when the path difference is smaller than the coherence length.

The process described was used by the authors to test the optical properties of optical fibers. Huang et al. adapted the idea to be used as an imaging apparatus, by adding scanning capabilities to the sample arm, in order to alter the position on the sample at which the laser is directed to. Put simply, it is a fiber optic Michelson interferometer where the movement of the reference mirror provides the ability to get axial information on the sample's structure, and the scanning along a transversal axis allows to collect that data in a line, thus creating a cross-sectional image of the sample. The lateral resolution is limited by the light beam diameter, and the axial resolution is related to the wavelength and bandwidth. They reported a Full-Width at Half-Maximum (FWHM) of 17 μm in air, but claim they were able to systematically locate sample reflections with a resolution of less than 2 μm due to the different refraction index of the analyzed tissue. As demonstrated in figures 2.1, the structure of the samples can be distinguished fairly well, which encouraged the use of this technology for new possibilities in *in vivo* imaging.

Following its introduction, development and usage of OCT technology in ophthalmology evolved steadily. Soon, the first *in vivo* images of the retina were acquired [24, 72], and by the mid nineties, several clinical studies were already investigating the use of OCT for diagnosis and monitoring of various macular diseases, such as macular edema [39, 66], central serous chorioretinopathy [38], glaucoma [70] and age related macular degeneration and choroidal neovascularization [37]. The application of this technology to other tissues was also being studied, as its application potential went beyond

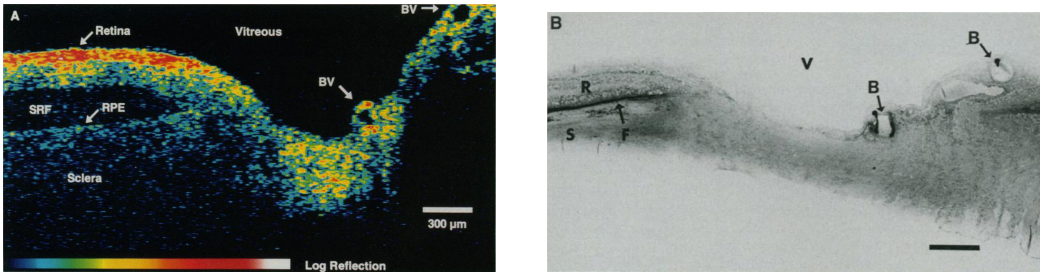

(a) (b)

Figure 2.1: (a) First optical coherence tomograph of an *in vitro* human retina and optic disk on the left. (b) Corresponding histological section of the same specimen. **BV** and **B** are blood vessels. **V** is the vitreous. **R** is the retina. **SRF** and **F** is the subretinal fluid, **S** is the sclera. **RPE** is the retinal pigment epithelium. [40]

imaging the eye, and could be used for imaging even difficult highly scattering tissues, such as urologic tissue [73], respiratory tracts [74], gastrointestinal tissue [74, 47], human skin [78] and intra-arterial imaging [31].

In 1996 this technology was introduced commercially for ophthalmic diagnostics, by Carl Zeiss Meditec [28]. It has since become a standard in ophthalmologic diagnosis.

The method presented by Huang et al. [40], which resorts to a movable reference mirror, is known today as Time Domain Optical Coherence Tomography (TD-OCT). This name refers to the fact that in this variant the encoded information about the sample structure is retrieved by varying the path-length of the reference beam, and consequently the delay relative to the sample beam. However, other methods have since been developed that rely on low coherence interferometry but take advantage of different wavelengths to get data about the sample structure. These are generally known as Fourier Domain Optical Coherence Tomography (FD-OCT).

FD-OCT works in similar fashion to the TD-OCT approach, but with key differences. In TD-OCT, axial imaging data is acquired by varying the position of the reference mirror, thus varying the path length of the reference beam, which allows the extraction of the axial structure of the sample by analyzing the interference at different distances, due to the small coherence length. In FD-OCT, the reference mirror is fixed, and the axial structure imaging is instead done by analyzing interference at different wavelengths, instead of different distances.

The first practical example of spectral interferometry was presented by Fercher et al. [26] in 1995. This was developed as an alternative to partially coherent interferometry [27], where no moving parts are required. Given

the greater speed and the fact that it provides the distribution of scattering potential in the object along the illuminating beam axis, the author suggests its usage in partial coherence tomography. However, this modality was not adopted right away. The first instance of a FD-OCT was in 2000, when Leitgeb et al. [50] demonstrated its use. While the authors were trying to simultaneously gather spectroscopic data, they arrived at the conclusion that there was a trade-off between longitudinal resolution and spectral resolution, and that a smaller light bandwidth increased the prominence of noise effects, which made difficult the acquisition of tomographic and spectroscopic data at the same time. However, they also concluded that FD-OCT still provided a fast and simple method to perform OCT.

In 2003, several groups independently concluded that FD-OCT has a clear sensitivity advantage over TD-OCT [49, 17, 18], and that consequently it is a better choice for high speed imaging. Two varieties of FD-OCT are generally recognized: Spectral Domain Optical Coherence Tomography (SD-OCT) and Swept-Source Optical Coherence Tomography (SS-OCT).

SD-OCT uses a broadband light source, which is scattered by the sample's structures and interferes with the reference beam. But, unlike in TD-OCT, the mirror's position is fixed, and the resulting beam is directed toward a spectrometer, which breaks light into its spectral components. The light is then directed to a detector array, where the interference signal is acquired for each spectral component simultaneously.

Wojtkowski et al. presented the first retinal imaging obtained through SD-OCT [80], which showed high sensitivities. Its performance raised interest in this technology, particularly after the several papers that appeared in the following year [49, 17, 18]. Soon after, several groups started demonstrating this technology's capabilities by achieving resolutions lower than 6 μm with speeds of up to 29000 axial scans per second. Here, a trade-off can be seen between resolution and scanning speed: Cense et al. reported a resolution of 3.5 μm at a speed of 14600 axial scans per second [15]; Nassif et al. reported a resolution of 6μm at 29000 axial scans per second [56]; Wojtkowski was able to achieve a resolution of 2.1 μm while scanning at a rate of 16000 axial scans per second [81]. However, even the slowest of these experiments is much faster than the time-domain devices of the time, with the authors estimating them being around 59 to 100 times faster than their TD-OCT counterparts [81, 15].

SS-OCT is similar in principle to SD-OCT: both measure interference signals for a somewhat large interval of frequencies. In fact, the signal acquired is similar between them. The difference, however, lies in how the signal for the different frequencies is measured. While SD-OCT uses a broadband laser source which emits a broad range of wavelengths simultaneously, SS-OCT

uses a laser source with narrow bandwidth, whose frequency is continuously swept across a given range. There is no need to use a spectrometer to separate the resulting beam, requiring only a single photodetector instead of an array. It can be said that in SD-OCT the obtained information is encoded in space, and in SS-OCT it is encoded in time.

By the time OCT appeared, similar frequency domain reflectometry techniques were already used for several years to determine the properties of optical systems and their components, particularly optical fibers [34, 6, 23]. In 1997, the first usage of SS-OCT was first demonstrated by Chin et al [16], but the advantages of this method were not recognized at first, with performance being limited by existing laser technology. They used an external cavity laser with a superluminescent Light Emitting Diode (LED) with peak gain near 840 nm and about 25 nm of bandwidth, capable of sweeping the full frequency range at $10Hz$. The low speed was a severely limiting factor to the technology. A few years later, in 2003, Yun et al. showed more promising results, being able to acquire images with a resolution of $13-14$ nm at 19000 axial scans per second [83]. These values would keep improving in the following years, while the popularity of SS-OCT grew. In 2006, Huber et al. published a paper where they claim to achieve speeds of 370000 axial scans per second, with reasonable image quality [41]. This is made possible by buffered Fourier Domain Mode Locking, a technique that allows increasing the sweep rate of Fourier Domain Mode Locked Lasers.

All these OCT variants will be further explored in Section 2.4. A brief review of current state of the art commercial systems will also be available in Secion 2.9.

2.2 The Michelson interferometer

The working principle of OCT is based on the Michelson interferometer, which was developed by the end of the nineteenth century to disprove the existence of the luminiferous aether [54]. The aether was a theorized substance that appeared as a way to explain the propagation of electromagnetic radiation. This hypothesis was disproved by the Michelson-Morley experiment, which showed that the speed of light is independent of the direction of movement, therefore not being subject any material medium of propagation.

In this device, whose schematic representation can be seen in Figure 2.2, a low-coherence light source is used to produce a collimated beam. The light then passes through a beamsplitter and is divided in two beams, one which crosses the splitter and another that is reflected in a perpendicular direction. Both beams are reflected by mirrors and return to the beamsplitter. There,

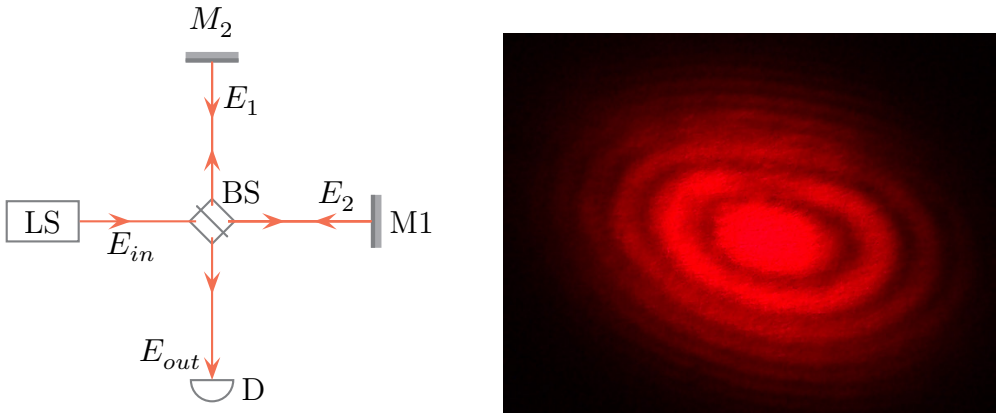

(a) (b)

Figure 2.2: (a) Diagram of a Michelson interferometer. LS: Light Source; BS: Beamsplitter; M1: Mirror 1; M2: Mirror 2; D: Detector. (b) Fringe pattern created by a Michelson interferometer using a red light source.

they are both directed toward the detector. If the overall paths taken by the light beams differ slightly in length (including the distance travelled inside the beamsplitter), a fringe pattern can be Seen in the detector. This pattern occurs due to constructive and destructive interference between both beams, which are similar in almost every aspect, but are out of phase. The superposition of waves that gives rise to the interference phenomenon is represented in 2.3, and is explained with greater depth in Section 2.3.1.

Variations of the Michelson interferometer continue to be used today in diverse fields. OCT in all its forms is a descendant from this apparatus. Another of its current incarnations is currently a part of large scale physics experiment to detect gravitational waves, the Large Interferometer Gravitational-Wave Observatory [7], which managed to detect for the first time cosmic gravitational waves from the merger of two black holes [1].

2.3 Physical principles

2.3.1 Interference

The Superposition Principle states that when two or more separate waves arrive at the same place in space where they overlap, they add or subtract one another without permanently destroying either wave. The resulting wave is the algebraic sum of the individual constituents of each wave at that location. Optical interference is a consequence of the application of this principle to

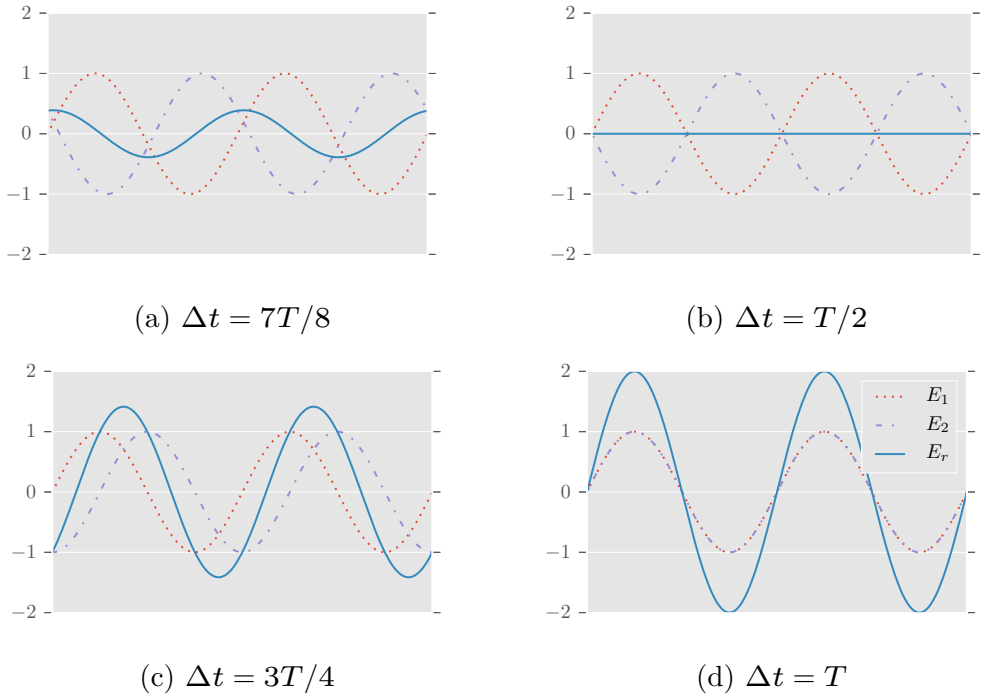

(a) $\Delta t = 7T/8$ (b) $\Delta t = T/2$

(c) $\Delta t = 3T/4$ (d) $\Delta t = T$

Figure 2.3: The result of superimposing a wave with a delayed version of itself. Δt describes the delay as a function of the wave's period T. E_r is the result of the superposition of the other two waves.

lightwaves. It can be described as an interaction between two waves at the same point in space where the overall resulting irradiance differs from the sum of the component irradiances.[36]

The Michelson interferometer can be used to better understand this phenomenon and why it happens. The exponential formulation of the electric field of a planar polarized light wave can be written as follows:

$$E(\omega, t) = s(\omega)e^{-i\omega t + kz} \tag{1}$$

In this expression, $s(\omega)$ is the source field amplitude spectrum, ω is the angular frequency of the wave, t is the time variation, k is the wavenumber and z is the distance to the source. The second term of the exponential, kz, accounts for the phase accumulated in distance travelled through the wave. At any given time, the phase of the emitted light is arbitrary, and only the relative phase difference between the beams is measured by the interferometer, so this term can be dropped for now.

The variables E_{in}, E_{out}, E_1, and E_2 denominate the optical field of the input, output, and mirrored beams, respectively. The beamsplitter trans-

mittance into each of the arms is T_s and T_s, for the sample and reference arm, respectively, and are related in such way that $T_s + T_r = 1$. Lastly, the mirrors at the end of the arms are considered to be ideal, with the mirror M_2 being slightly more distant from the beamsplitter than the mirror M_1, with a length difference of Δz. The beams can then be described in the following way:

$$E_{in}(\omega, t) = s(\omega)e^{-iwt} \tag{2}$$
$$E_1(\omega, t) = (T_r T_s)^{1/2} E_{in}(\omega, t) \tag{3}$$
$$E_2(\omega, t, \Delta z) = (T_r T_s)^{1/2} E_{in}(\omega, t)e^{-i\phi(\Delta z)} \tag{4}$$
$$E_{out}(\omega, t, \Delta z) = E_1(\omega, t) + E_2(\omega, t, \Delta z) \tag{5}$$

The term $\phi(\Delta z)$ is the overall phase shift caused by the difference in path length Δz between the first and second beam. Knowing that $\phi(\Delta t) = \omega \Delta t$ and $\Delta z = \Delta t c / n_{air}$, where c is the speed of light in a vacuum and n_{air} is the refractive index of air, the difference in phase is described by:

$$\phi(\Delta z) = \frac{2\omega n_{air} \Delta z}{c} \tag{6}$$

The factor of 2 is caused by each of the mirror beams travelling the distance twice, once toward the mirror and again after being reflected. This equation assumes that the beams only propagate through air. The relative irradiance measured at the detector can be given by:

$$I = \langle E_{out}^2 \rangle_T \tag{7}$$

Substituting by Equation (5) leads to:

$$I(\omega, \Delta z) = \langle (E_1 + E_2)^2 \rangle_T \tag{8}$$
$$I(\omega, \Delta z) = \langle E_1^* E_1 \rangle_T + \langle E_2^* E_2 \rangle_T + 2\Re \langle E_1^* E_2 \rangle_T \tag{9}$$

Here, the first two terms refer to self-interference, whereas the last term represents the real part of the interference between both superimposed beams. Substituting the optical spectrum for an intensity spectrum, $S(\omega) = |s(\omega)|^2$ and expanding, it becomes:

$$I(\omega, \Delta z) = 2T_r T_s S(\omega)(1 + \Re\{e^{-i\phi(\Delta z)}\}) \tag{10}$$

This is the general expression for the irradiance on the detector for a Michelson interferometer. Although the end-result and purpose is different,

the process and reasoning for working with OCT is somewhat similar to this device, and thus this makes a good starting point.

As can be seen in Equation (10), the irradiance varies with the difference in length between paths. This is the source of the typical circular fringe pattern associated with these experiments. The light takes a longer path to reach the outer part of the incidence surface, and the phase difference varies continuously with the increasing path difference among both beams.

2.3.2 Coherence

Coherence is a property of light waves that is necessary (but not sufficient) to produce interference patterns. In general terms, two light sources are considered coherent if the phase difference between them remains constant.

Light can be coherent in space and in time. Spatial coherence describes the ability of two light sources maintaining their phase relationship throughout their wavefronts. Temporal coherence, on the other hand, is related to maintaining a constant phase relation at the same point, continuously through time.

In the context of this work, the production of light typically occurs when electrons in atoms or molecules descend from an excited state to another state of lower energy. The energy released as electromagnetic radiation is the same of the difference in the energy levels of the electron.

$$E = hf \tag{11}$$

Here, E stands for energy, f for frequency and h for the Planck constant. This transition is not instantaneous, but takes a very small amount of time, during which a wavetrain is produced. Wavetrains are classical descriptions of short oscillatory directional pulses, which usually last less than $10^{-8}s$. Their frequency is not necessarily well defined, as is required of photons, and as such are different from them and more useful to this explanation.

A continuous and perfectly monochromatic light source would always be coherent with itself as it would continuously maintain the same phase relation between any two points in space or time. However, light sources are not perfectly monochromatic. In solids and liquids, atoms interact with each other, creating a broad range of emission frequencies. Even in gases, where the large distances between atoms allow them to operate independently and produce very narrow frequencies of light, there is always some broadening of the emission lines due to motion, collisions and other factors. The natural linewidth of the emitted light should also be considered. This phenomenon

is caused by the inherent uncertainty derived from the uncertainty principle.

$$\sigma_E \sigma_t \geq \frac{\hbar}{2} \tag{12}$$

Here, σ_E is the standard deviation in energy, σ_t is the standard deviation in time and $\hbar$ is the reduced Planck constant. It states that the uncertainty in energy is greater for states with shorter lifetimes. The process of light generation has a duration in the order of 10^{-8} to 10^{-9} s, which causes a natural broadening for each light emission. All of this amasses to the light produced having a bandwidth $\Delta\mu$ rather than one single wavelength λ.[36]

For a non-monochromatic light source, coherence is not guaranteed throughout time and space. However, it is possible to maintain a beam's coherence with a delayed version of it in certain conditions, namely when the difference in paths is smaller than the coherence lenght. The coherence length is the extent in space over which the wave oscillates in a regular, predictable way, maintaining a certain reliable degree of coherence [36]. This metric can be defined in a number of ways, with the most commonly used one being the FWHM of the source's self-coherence function multiplied by the speed of light. The self coherence function is the inverse Fourier transform of the source's intensity spectrum. Assuming the source's spectrum is Gaussian, which is a fairly accepted approximation, the coherence length is [75]:

$$l_c = \frac{4\ln(2)}{\pi} \frac{\lambda_0^2}{\Delta\lambda} \tag{13}$$

λ_0 is the centre wavelength of the source, and $\Delta\lambda$ is the wavelength range. Another important value which is related to the coherence length is the coherence time:

$$t_c = \frac{1}{c} \frac{4\ln(2)}{\pi} \frac{\lambda_o^2}{\Delta\lambda} \tag{14}$$

The coherence time is related to the temporal extent of the wavetrain. [36]. It's worth noting that the coherence length is the coherence time divided by the speed of light. Both these values are related to temporal coherence, as the coherence length is simply the distance over which light propagates during the coherence time.

As it was already mentioned, in order to obtain interference patterns in interfometry, the path difference between both beams has to be smaller than the coherence length, or the delay between beams has to be lower than the coherence time. However, the choice of these values has more to it than this.

As will be explained in Section 2.4, the coherence length is directly related to the resolution of OCT devices.

2.3.3 Interaction of Light with Matter

Some concepts related to the interaction between light and matter are ubiquitous when doing optical imaging. As these are key points of data acquisition, particularly in the case of OCT, they often define the constraints and choices associated with a given experimental setup. The topics most relevant to OCT will then be here presented, with a brief discussion of their importance and implications.

The first important phenomenon to consider is dispersion. Dispersion corresponds to the phenomenon whereby the index of refraction is frequency dependant. This phenomenon is observable in all media except vacuum [36]. Depending on the application to consider, dispersion can produce desirable or undesirable effects.

One famous consequence is the separation of the different components of white light when it travels through a prism. When white light is directed at an angle to the surface of a prism, the angle at which light leaves the prism is dependent on the refraction indexes, which are themselves dependent on the light's frequency. Thus different components leave at different angles. The decomposition of a non-monochromatic beam into its components is achievable through this method.

An example of a negative consequence is its effect on group velocity. Light with a variety of wavelengths travels with a group velocity. When it crosses a medium, it undergoes dispersion, with greater bandwidths being subject to greater dispersion. In the case of OCT, if the sample beam is too dispersed, it will not interfere in a way which does not allow ranging. Compensation for dispersion is usually required in these cases [12].

Considering now the process of analyzing the sample, it's important that the light to be used is capable of penetrating the sample's tissue and getting back out in order to travel the inverse path, so that interference with the reference beam can occur. However, due to different propagation media, this can be difficult, even in transparent media. Absorption and scattering are the two phenomena that impact this process the most.

An atom can react to incoming light in one of two ways: either by redirecting the incoming photon without altering it, or by absorbing it, in case the photon's energy is equal to the energy necessary for the atom to be excited to a higher energy state. The first way of dealing with light roughly refers to scattering, while the latter deals with absorption.

When an atom absorbs incoming light in the conditions mentioned above,

it can return to a lower, more stable energy level, and produce another photon to get rid of the excess energy. However, this is more likely to happen in certain conditions, such as in a vacuum, where the atom is somewhat isolated. In a scenario of bulk matter, where the atom is not isolated but is instead close to other atoms, such as in solids, liquids or high pressure gases, the outcome is likely to be different. The absorbed energy can quickly be "shared" with the receiving atom's surroundings before a photon ends up being emitted. This happens due to collisions, which convert the energy to random atomic motion, thermal energy. The described phenomenon is called dissipative absorption [36].

There is a relation between absorption and dispersion. At the resonant frequency, absorption occurs. However, as the frequency approaches that value, the refractive index changes rapidly near the absorption peak. This is because energy is absorbed and re-radiated at a different phase, and dispersion becomes prominent [12].

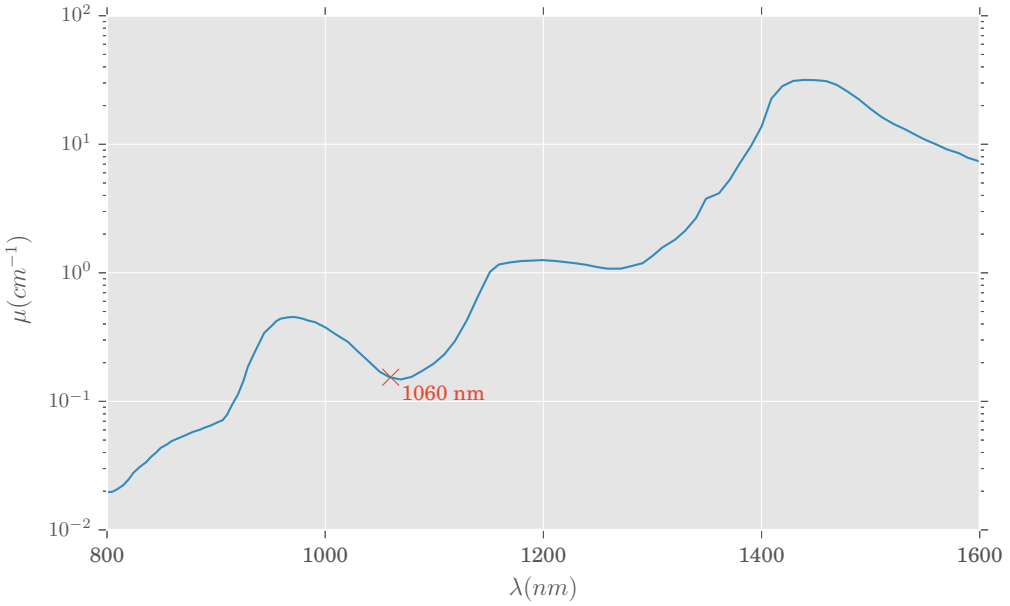

Figure 2.4: Absorption coefficient for water as a function of the wavelength.[65, 71]

The variation of the absorption coefficient of water as a function of the incident wavelength is represented in Figure 2.4, with the data determined experimentally by Segelstein [71]. The overall shape is rather complex, but it can be seen that within the near infrared spectrum the overall trend is for absorption to increase with the wavelength. However, several local minima

exist. These minima are values which could be considered for the center wavelength of the light source used in OCT, as they grant reduced absorption in comparison with other values. However, other requirements also have to be considered, in part related with other phenomena.

The other possible interaction between light and matter mentioned before is called non-resonant scattering, and occurs when the light's frequency is lower than the resonance frequency, which cannot excite the atom. In this case, the atom's electronic cloud oscillates slightly with the energy of the incident radiation, which causes the emission of a photon with the same energy but different direction.

Several scattering processes exist, which are dependent on several factors, but only elastic scattering will be considered here, which means there is no energy difference between the incident and scattered photons. Most of the scattering is due to relatively large particles (compared to the wavelength of the incident radiation), composed of groups of oscillators, with a different refractive index than its surroundings. It is the degree of mismatch, size and shape of the particles relative to the wavelength, and their density that determines light scattering [12].

Scattering can normally be accounted for with its coefficient [48]:

$$\mu_s = \frac{\mu_s'}{1-g} \tag{15}$$

In this expression, μ_s' is the reduced scattering coefficient, and g is the anisotropy factor, which accounts for the average effect of the scattering angles [8]. This factor can in most cases be considered to be 0.9, as it is a common value for many tissues in the visible and infrared light range [76]. The reduced scattering coefficient is a different matter, and can be approximated by a power law [8]:

$$\mu_s' = a\lambda^{-w} \tag{16}$$

The wavelength λ can be normalized by a reference wavelength, typically 500 nm. Parameter a is related to the concentration of particles in the media, and w characterizes the average size of the particles and defines the spectral behaviour of the scattering coefficient [8]. These parameters are obtained empirically.

Scattering is different for different tissues, and the fitting parameters for different biological tissues have been extensively studied by different authors [8, 48, 76]. However, one factor common to all, as can be seen from Equation (16), is that usually light with shorter wavelengths is associated

with a higher reduced scattering coefficient and, consequently, is more susceptible to scattering.

The absorption and scattering coefficients are two important values that impact the sensitivity and penetration depth of OCT, and as seen, respond differently to shorter and longer wavelengths. Therefore, a balance has to be achieved in the light source in order to minimize losses through absorption and scattering and optimize imaging potential. In Figure 2.4 one of the local minima mentioned before is marked at 1060 nm. This value meets a good compromise between a relatively large wavelength, as to minimize scattering, and a relatively low absorption coefficient, in the order of $0.15cm^{-1}$ [65, 71]. This is the center wavelength of the light source used in the experimental system described in this work.

2.4 Optical Coherence Tomography

With the necessary concepts explained to form a suitable background, Optical Coherence Tomography and its different modalities can now be properly introduced. Three main modalities exist: Time Domain Optical Coherence Tomography, Spectral Domain Optical Coherence Tomography, and Swept-Source Optical Coherence Tomography. First the common ground to OCT will be laid, picking up from the explanation on interference and the Michelson interferometer in Section 2.3.1. After that, the several modalities will be presented, and posteriorly compared, with their strengths and weaknesses.

Picking up the example of the Michelson interferometer, Equations (3, 4, 5) refer to the corresponding reflected and resultant beams if there are perfect mirrors in each arm, at slightly different distances. However, in OCT, one of the arms contains a target sample to be analyzed, which means the reflected beam will be significantly different, containing relevant data about its structure.

The additional complexity originating is treated by abstracting the sample as an object which induces a transformation in the input signal, the incident beam, and returns the transformed signal. In these circumstances, the sample's structure can be described through a mathematical expression that represents the light which is reflected from the sample as a function of the incident beam. For the purpose of this explanation, all optical losses due to absorption and dispersion shall be ignored.

The reflectivity of the whole sample can be considered its frequency do-

main response function $H(\omega)$:

$$H(\omega) = \int_{-\infty}^{\infty} r(\omega, z) e^{i2n(\omega,z)\frac{\omega z}{c}} dz \tag{17}$$

Here, c is the speed of light, $r(\omega, z)$ is the electric field reflectivity of a surface at depth z for light of frequency ω, and $n(\omega, z)$ is the frequency dependent, depth varying refractive index.

An approximation of this response can made by considering a simplified description of the sample. Assuming the sample is composed of M reflective surfaces, its reflectivity, which is usually a continuous complex function, can be approximated by [46]:

$$r_s(z) = \sum_{m=1}^{M} r_m \delta(z_s - z_m) \tag{18}$$

Considering the reflectivity as a discrete function, and assuming that the beam is perpendicular to each of the sample's layers, r_m can be defined the following way, through the refractive indexes of adjacent surfaces, from the Fresnel Equations [36]:

$$r_m = \frac{n_{m+1} - n_m}{n_{m+1} + n_m} \tag{19}$$

This way, having defined the sample's reflectivity as a function of each surface's reflectivity (r_m) and its respective depth reflectivity of each surface (z_m), it's possible to obtain a simpler, discrete version for the frequency domain response function [46]:

$$H(\omega) = \sum_{m=1}^{M} r_m e^{i2\frac{\omega}{c}\sum_{l=1}^{m} n_l z_l} \tag{20}$$

The power reflectivity of each of the reflecting surfaces is $R_m = |r_m|^2$. The purpose of the interferometry in OCT is the reconstruction of the function $\sqrt{R_m(z)}$.

With the domain response function $H(\omega)$ Equation (3) can then be adapted to represent the beam reflected from a sample's structure.

$$E_s(\omega, t) = (T_r T_s)^{1/2} H(\omega) E_{in}(\omega, t) \tag{21}$$

From now on, E_2 referenced in Equation (4) will be referred to as E_m, as it represents the beam reflected from the reference mirror. Also, $\Phi(\Delta z)$ now refers to the total phase difference acquired by the reference beam along its path. Recalling Equation (9) and adjusting it yields:

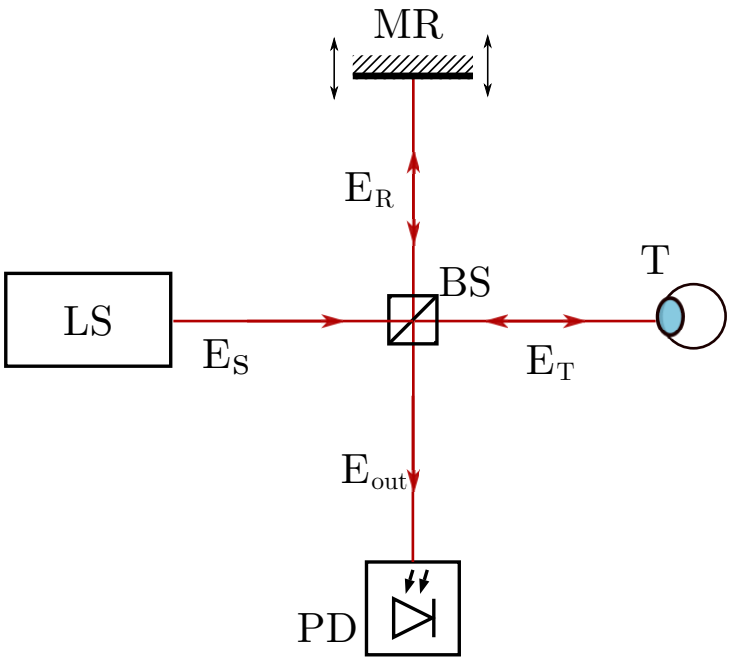

Figure 2.5: Diagram of a Time Domain OCT. LS represents the laser source, MR is the reference mirror, T is the target (an eye in this case), BS is the beamsplitter and PD is the photodetector.

$$I(\omega, \Delta z) = T_r T_s (S(\omega)|H(\omega)|^2 + S(\omega) + 2\Re\{S(\omega)H(\omega)e^{-i\Phi(\Delta z)}\}) \quad (22)$$

Equation (22) represents the general expression for an OCT signal. It contains contributions from several signal sources, mainly cross-interference between the sample and reference beams, self-interference between the different layers of the sample beam, and a DC component.

2.4.1 Time Domain OCT

Time Domain Optical Coherence Tomography was the first OCT method to be developed. Unlike in Fourier Domain methods, the axial data is extracted by varying the delay in the reference arm. As explained before, interference can only occur when the path difference is shorter than the coherence length. If for some position of the reference arm there exists a corresponding scattering surface in the sample whose reflection travels a similar path length, interference can be detected in the detector. TD-OCT is based around this relation between interference and the path-length difference. The reference mirror is scanned perpendicularly to the beam while the sample remains

n	$z(\mu m)$
1.0	5
1.3	15
1.5	30
1.0	0

Table 2.1: Refraction index and length for the sample's layers.

static. This way, the path-length of the reference beam is varied across a fixed range, which can then interfere with the reflections from the different scattering surfaces in the sample.

The signal acquired at the photodetector can be described by integrating Equation (22) over the source spectrum [75]. In these conditions, the irradiance on the sample is described by:

$$I(\Delta z) = \Gamma_0 + \Re\{\Gamma(\Delta z)\} \tag{23}$$

Here the first term corresponds to the contribution from self-interference:

$$\Gamma_0 = \frac{1}{4}\int_{-\infty}^{\infty} S(\omega)(|H(\omega)|^2 + 1)d\omega \tag{24}$$

The second term corresponds to cross-interference:

$$\Gamma(\Delta z) = \frac{1}{2}\int_{-\infty}^{\infty} S(\omega)H(\omega)\cos\{\phi(\Delta z)\}d\omega \tag{25}$$

Figure 2.6(b) provides an example of the signal acquired during a TD-OCT axial scan of a sample with four refracting layers, as displayed in Table 2.1. The sample contains three reflecting interfaces, one between each pair of layers. The plots are from a simulation which uses a 1060 nm light source with a 100 nm bandwidth. Each of the envelope's peaks in the graphic corresponds to one of those interfaces, and the distance between each of the envelope's peaks is proportional to the corresponding layer thickness and its refraction index. As such, the first peak should be near $1 \times 5 = 5$ μm, the second should be near $5 + 1.3 \times 15 = 24.5$ μm and the third should be around $24.5 + 30 \times 1.5 = 69.5$ μm. As can be seen, the peaks are where they are expected, and their magnitude grows with the reflectance of the interface.

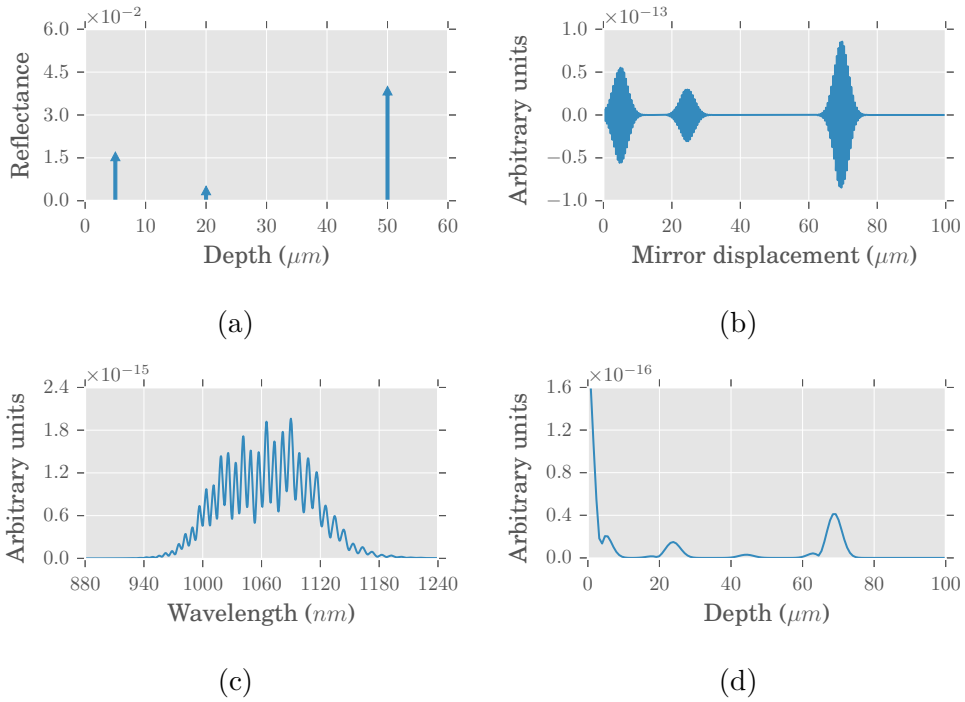

Figure 2.6: (a) Position and reflectance of the layers from the sample. (b) Time Domain Optical Coherence Tomography interference signal. (c) Fourier Domain Optical Coherence Tomography interference signal (d) Inverse Fourier transform of a FD-OCT signal. Adapted from [75]

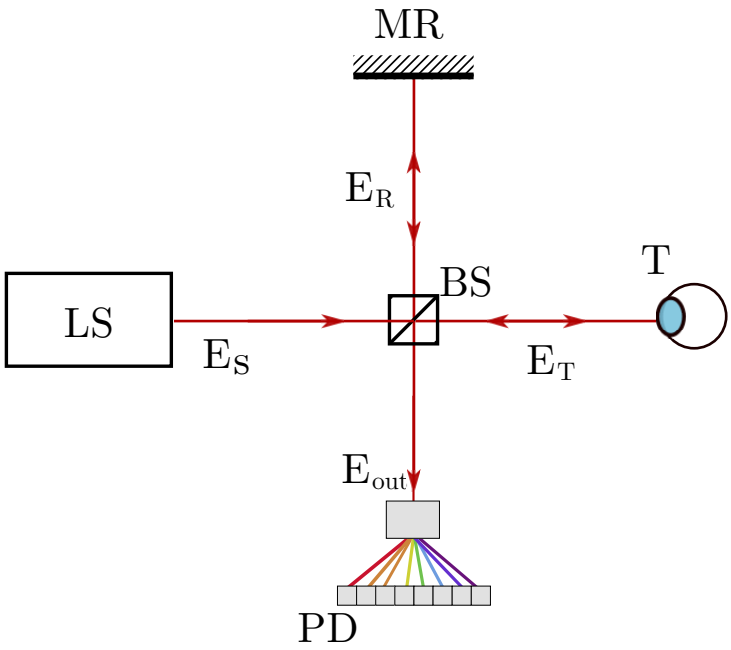

Figure 2.7: Diagram of a Spectral Domain OCT. LS represents the laser source, MR is the reference mirror, T is the target (an eye in this case), BS is the beam-splitter and PD is the photodetector array. The colors in the light incident on the photodetector array is merely for illustrative purposes.

2.4.2 Spectral Domain OCT

From Equation (22), it can be seen that, for the same path length, interference still varies with the optical frequency. This allows an alternative approach, in which the reference mirror is kept at a fixed distance, and data is instead acquired by watching for interference with different wavelengths. With $\Delta z = 0$, the expression for the detected frequency spectrum becomes:

$$I(\omega) = \frac{1}{4} S(\omega)\{H(\omega) + 1\}^2 \tag{26}$$

The structural data can be acquired by transforming $I(\omega)$ into the time domain interference pattern through an inverse Fourier transform, providing a signal similar to the TD-OCT one [75].

$$I(t) = FT\{I(\omega)\} \tag{27}$$

In SD-OCT a large bandwidth light source is used to provide wide range of wavelengths. After the beam is backscattered by the sample and the

reference mirror, E_{out} is split by a diffraction grating. This causes the beam to split into its component frequencies, which are then collected at a linear detector array. $I(\omega)$ is acquired discreetly, and constituted by a finite number of data points. This allows the use of a Fast Fourier Transform algorithm.

One important difference in comparison to TD-OCT is that, as the mirror is fixed, the axial scanning range is not determined by its movement [10]. Instead, it is determined by the light source. Assuming it has a Gaussian spectral distribution, a reasonable and commonly accepted approximation of the scanning length in SD-OCT is:

$$l_D \approx l_C \frac{\Delta\lambda}{\delta\lambda} \approx \frac{0.44\lambda^2}{\delta\lambda} \tag{28}$$

2.4.3 Swept-Source OCT

Swept-Source Optical Coherence Tomography is similar in theory to SD-OCT, in the sense that it uses a wide range of wavelengths to extract structural data from the sample. A similar mathematical treatment can be used to process the acquired data. However, its practical implementation is fairly different.

SS-OCT typically uses a narrowband tunable frequency-swept laser source to create the beam for studying the sample[10]. This is a laser which is capable of producing a wide range of frequencies, such as the light source needed in SD-OCT. However, instead of producing a single constant beam with a large bandwidth, it cyclically sweeps through the entire range of frequencies in sequence. The signal produced at the detector is acquired for one wavelength at a time.

No additional diagram of an SS-OCT is provided because it is similar to the previous one, with the difference it the different wavelengths are emitted at different times, so only one wavelength is detected at a time and therefore the photodetector array is replaced by a photodetector.

2.5 OCT scans

Different types of scans can usually be acquired through an OCT. The most basic one, and already mentioned several times in so far, is the axial scan. Commonly know as A-scan, it refers to an axial measurement of the sample's structure, perpendicular to the surface targeted by the beam. It provides the one-dimensional reflectivity profile of the sample in the depth

direction [46]. In different modalities it is associated with a different physical process:

- In TD-OCT it is done by scanning the reference mirror in a direction parallel with the beam, in order to measure interference at different distances. An A-scan corresponds to the entire range scanned by the mirror.
- In SD-OCT, the A-scan is acquired by separating the resulting beam into its components and measuring interference in each of them, using a detector array. Each acquisition on the detector array corresponds to an A-scan.
- In SS-OCT this is achieved by sweeping the light source through its entire range of frequencies, measuring interference for each of them sequentially. Each entire sweep of the light source is a single A-scan.

As the beam is laterally scanned across the sample, a linear sequence of A-scans is acquired. This sequence is then processed, creating a 2-dimensional image composed of a sequence of depth profiles, where one dimension follows depth, and the other is orthogonal to the axis direction. This is called a B-scan. [46]

As it is possible to acquire a 2-dimensional image of a cross-sectional surface by juxtaposing consecutive A-scans, it is also possible to create a 3-dimensional volume by acquiring B-scans sequentially [46]. This can be referred to as a Volume Scan.

A less frequently mentioned scan modality is the M-scan, in which A-scans are acquired sequentially at the same spot during a given period of time, creating a depth profile as function of time.[46]

A different type of basic scan is the T-scan, which is a transversal scan at fixed depth, as opposed to the A-scan. It prioritizes lateral scanning instead of depth scanning. Due to its nature, it's only viable in TD-OCT, which is able to maintain a fixed reference mirror position while scanning the sample in a transversal direction. As SD-OCT and SS-OCT acquire the full range of axial structural data at any time, it is not physically possible to only scan at a fixed depth. It can however be done while processing, by discarding any data that is not from a specific depth, but it brings no benefits. In TD-OCT, however, it does provide interesting applications. For instance, creating a 2-dimensional image of a surface at fixed depth, which is commonly known as C-scan (constant depth) or en-face scan. To do the same in the other OCT modalities would require that a whole volume be acquired just to be able to see a fixed-depth surface.[69, 61, 64, 53]

2.6 Performance Parameters

2.6.1 Axial Resolution

Axial resolution or depth resolution describes minimum distance in depth for which two different interfaces can be distinguished by the system. It is dependant on the light source and its coherence length, which can be found in Equation (13)[25, 75].

Spatial resolution of an imaging system is usually assessed through the magnitude of the Inverse Fourier Transform (IFT) of the Point Spread Function (PSF)[25]. For a Gaussian source spectrum, the axial resolution needs to be:

$$\sigma_z = \frac{2\ln 2}{\pi}\frac{{\lambda_0}^2}{\Delta\lambda} \tag{29}$$

This is the equation that defines the resolution of OCT in free space [12], where λ_0 is the central wavelength of the source, and $\Delta\lambda$ is its spectral width at half maximum. For biomedical applications, the axial resolution needs be good enough in order to enable drawing conclusions from the acquired images. Usually it can be considered adequate if it is lower than 10 μm [79].

2.6.2 Lateral Resolution

The lateral resolution in OCT systems is independent from the axial resolution. It refers to the ability to distinguish two points in the direction perpendicular to the beam axis, and does not depend on the coherence length.

Lateral resolution can be determined by the diffraction limited spot size of the optical beam, which is inversely proportional to the numerical aperture of the objective, NA_{obj} [28].

$$\sigma_x = \frac{4\lambda}{\pi}\frac{f}{d} \tag{30}$$

Knowing that $f/d = 1/(2\mathrm{NA})$ [36], it can be approximated to:

$$\sigma_x = 1.22\frac{\lambda}{2\mathrm{NA}_{obj}} \tag{31}$$

This allows the optimization of lateral scanning without compromising the axial resolution [75].

However, there is a trade-off exists between axial resolution and depth penetration, as will be seen in Section 2.6.3. Therefore, a compromise should be reached in order to optimize the device to its function.

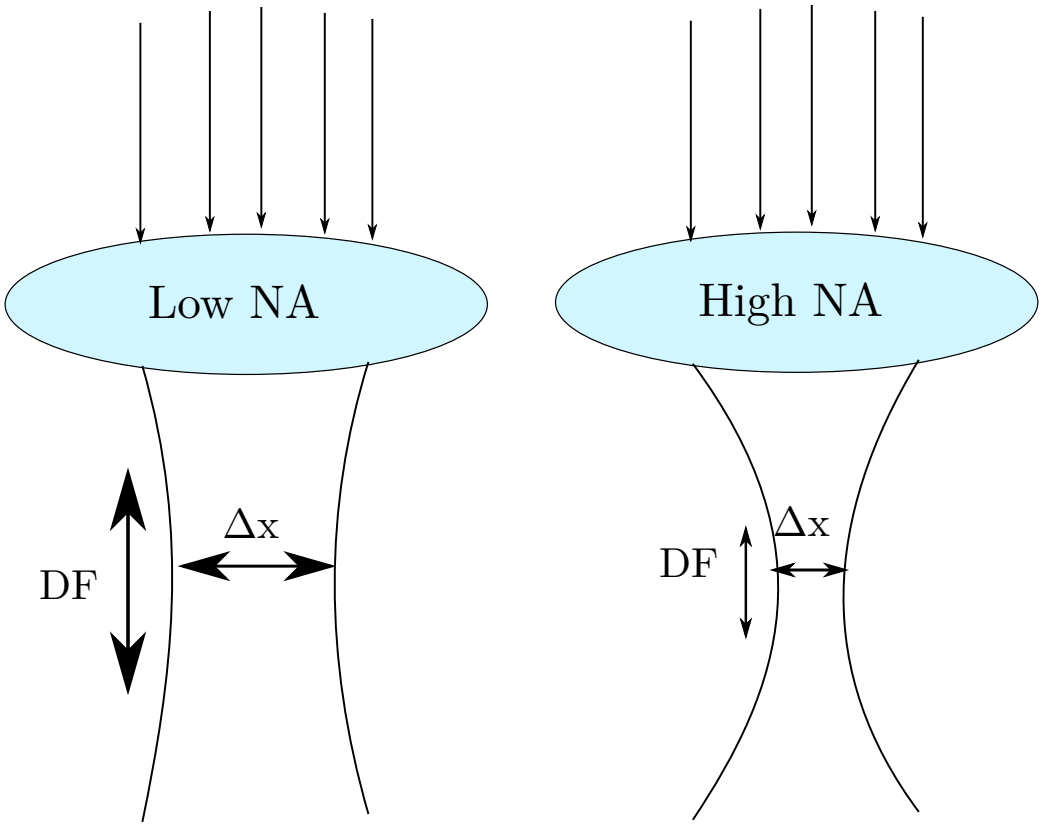

Figure 2.8: Relation between depth of field, NA, and lateral resolution.

The speed of lateral scanning and A-scan acquisition rate should be taken into account when deciding on the mentioned compromise. The beam displacement during the acquisition of an A-scan should be 1.5 to 2 times smaller than the lateral resolution of the device [11].

2.6.3 Depth of Field

The depth of field measures the length of the focus in the axial direction [12]. As such, it imposes a limit on the depth of the sample that can be acquired with good quality. It is defined by the confocal parameter b, which is twice the Rayleigh range [28]:

$$b = \frac{\pi {\sigma_x}^2}{\lambda} = 2\frac{\lambda n}{\mathrm{NA}_{obj}^2} \tag{32}$$

As mentioned before, improving the lateral resolution by increasing the numerical aperture leads to a smaller depth of field. However, other factors

affect the maximum depth observable, such as the sensitivity.

In order to choose a suitable numerical aperture, a value should be found that does not increase lateral resolution beyond what is practical according to acquisition times, and that does not compromise lateral resolution for unneeded depth of field, as depth imaging may be limited by other factors.

2.6.4 Signal to Noise Ratio

Signal to Noise Ratio (SNR) is the ratio of amplitude of the maximum obtainable signal to the amplitude of noise signals at a given point in time [12].

2.6.5 Sensitivity

Sensitivity is defined as the minimum input signal required to produce a given signal with a specified SNR. In OCT, the SNR chosen is usually 1. In these conditions, the signal that defines the sensitivity, typically the minimum sample reflection intensity, produces the same amount of output as noise [12].

For good image quality in biomedical applications, sensitivity should be above $95dB$ [79].

2.6.6 Dynamic Range

Dynamic range typically defines the ratio of the maximum value of a parameter, such as signal intensity, or sample reflectivity, for instance, in relation to its minimum detectable value, within the same acquisition. Biomedical OCT images often have around -35dB of dynamic range, so at least 40 to 50dB should be provided by the system [12, 79].

2.7 Imaging Speed

Imaging speed can be quantified in several ways. For instance, it can describe the number of A-scans per second, the number of B-scans per second or the number of voxels per second. All of these can be useful to describe imaging speeds in different circumstances and for different purposes. They can also be somewhat subjective, as opting to reduce the number of pixels often results in an overall speed up of the acquisition of A-scans, B-scans or volumes, even if it compromises image quality. Thus, the most objective way to quantify imaging speed is by measuring the average data output per second, usually pixels per second or voxels per second [79].

Imaging speed directly affects the quality of the resulting images. As OCT is a technique used *in vivo*, low acquisition speeds greatly increase the likelihood of finding artifacts in the images due to motion in the analyzed sample.

2.8 OCT Comparison

SS-OCT, when compared to SD-OCT, presents a much deeper tissue penetration and wider imaging depth, collection rate (100,000 A-scans/s) and better penetration in non-transparent media.[5]

2.9 State of the Art

Even though it is a relatively recent technology, with the first experiment appearing only around 25 years ago, Optical Coherence Tomography has become a standard in medical imaging. This is due mainly to the continuous improvements that allow sub-micron resolutions and great imaging speeds. Since its creation, resolution has improved by a significant factor, and imaging speeds are around 500000 times faster. While the resolution improvements were achieved by using ultra-broadband light sources, the improvements on imaging speed are in great part due to the appearance of new techniques which allowed the process to be significantly sped up. While the original TD-OCT had its imaging speed limited by its moving parts, SD-OCT is limited by the readout of the camera, and SS-OCT by the sweep time of the used light source. The development of new swept sources has been a decisive factor for the evolution of OCT [20].

Currently SD-OCT is the standard in ophthalmology, even though SS-OCT is capable of better performance. The adoption rate of the latter in this field is limited due to the comparably higher costs, lack of clinical and normative data and uncertainty about the future of OCT. However, adoption of SS-OCT in other clinical specialties is much better, such as cardiology, dermatology, and gastroenterology [30]. The versatility and continuing growth of OCT capabilities justifies its importance in the variety of fields its used in. Sesearch has presented devices capable of demonstrating acquisition speeds superior to 1000000 A-Scans per second [67] Current commercial OCT systems have also come a long way, and are currently able to achieve retinal imaging with 5 to 6 μm resolution at 200000 A-Scans per second [51], and a wide-field retinal and choroidal imaging using SS-OCT at 580,000 A-scans per second [35]. At this acquisition speed, a volume with 1000 A-Scans and

1000 B-Scans can be imaged in around 2 seconds.

OCT development show no sign of slowing down, and the technology grows increasingly relevant for medical diagnosis and research.

3 | Experimental setup

An overview of the system's setup at the moment this work started will now be presented. The initial experimental setup and components have been described in previous works [3, 14, 63, 77, 9, 57, 68], but the system underwent important changes recently, as will be shown in the following chapters. However, it's also important to get a basic understanding of the previous setup, its components and working process to comprehend the relevance of the changes made.

A presentation of the system components will follow the overview, with only a brief description in the parts and devices which are no longer used. The additions and changes to this setup will be presented in their relevant chapters, namely Chapter 4 for the new illumination and camera module and Chapter 5 for the new Control Module.

As it has been mentioned, the initial setup has been thoroughly described in previous works. The information shown in this chapter compiles information from these works and from the manuals and datasheets of the utilized components and devices.

3.1 Initial Setup

The system uses a Swept-Source Laser to perform measurements. This source provides three signals: the Laser Output, the Sweep Trigger and the Clock. The laser source is split in a 90:10 fiber coupler after exiting the source. In this split, 10% of the optical power is directed to the reference mirror and 90% to the sample. In both cases, the light then passes through separate 50:50 fiber couplers, which act as circulators to separate light propagating in different directions. Before exiting the fibers, light passes through a polarization controller, to match the polarization of the beams from the reference mirror and the sample. This creates optimal conditions for interference, improving the system's sensitivity.

In the reference arm, the light exits through a collimator and passes

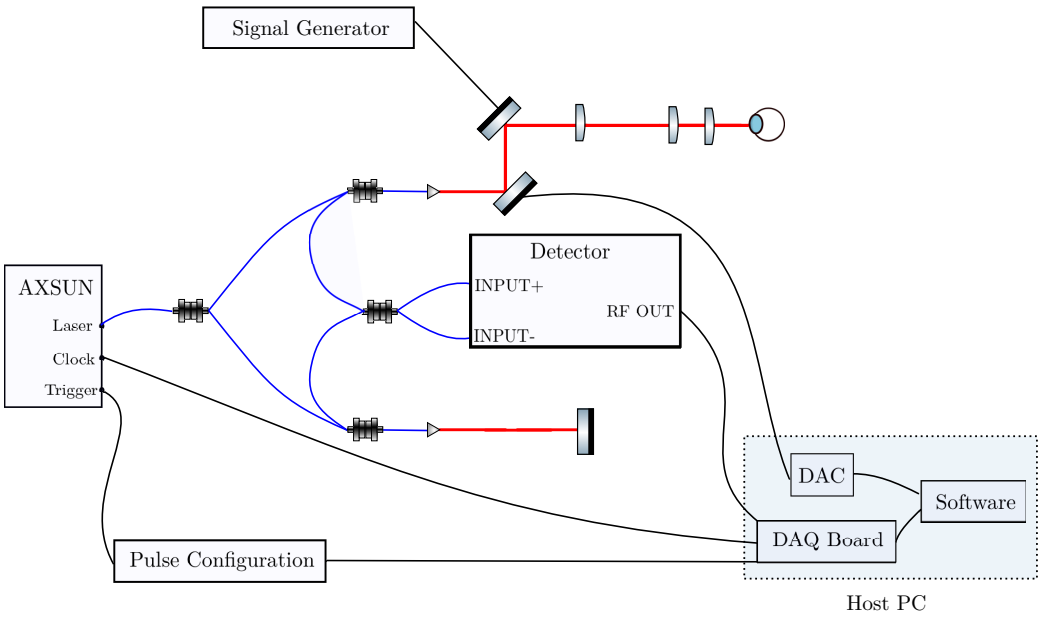

Figure 3.1: Initial OCT setup at the start of this work.

through an objective lens, which focuses the beam on a gold-coated mirror. The light is then reflected back through the same path, until it reaches the 50:50 coupler, where it is redirected to a different 50:50 fiber coupler.

In the sample arm, the light also exits through a collimator, and is directed to a bi-directional galvanometer scanning system. The beam is then focused on the sample after passing through two lenses which focus the beam on the sample. The backscattered beam then follows the inverse path, until it reaches the 50:50 coupler. It is then directed to the same 50:50 coupler where the reference beam is directed to. This coupler is then connected to a balanced photodetector, where the optical path finally ends.

The data produced in the photodetector is acquired by an acquisition board, which also receives signals from the Sweep Trigger and the Clock. These indicate the timings for the board to acquire the data, where the trigger signals the beginning of the acquisition, and the clock provides information on the wavelength emitted by the source. Further processing and display is then performed on the computer connected to the acquisition board. This completes the process for the acquisition of an A-Scan.

To acquire B-Scans, a signal generator is used to control the horizontal galvanometer movement through the ouput of a sawtooth wave, performing sequential A-Scans in a given horizontal range. This is a manually controlled process, requiring human intervention to setup and fine-tune the parameters.

Lastly, in order to acquire complete volumes, B-Scans are sequentially

acquired in a given vertical range, where the vertical galvanometer movement is controlled by a DAQ board connected to the computer software.

3.2 Laser source

The laser source is the core component of an OCT system, as it defines many of the system's performance capabilities and limitations. For instance, the rate of A-Scan acquisition cannot be higher than the laser sweep frequency.

The swept laser source used in this setup is an Axsun Technologies Swept Source Engine Model SSOCT-1060 [4]. As mentioned previously, this type of lasers sweep across a given range of wavelengths, and interference within this range is the source of depth information in this modality of OCT. The range of wavelengths this particular model produces is between 985 nm and 1095 nm, with a center wavelength at 1060 nm, and this range is swept at a rate of 100 kHz. These wavelengths are achieved through the use of a Fabry-Perot tunable filter placed at one end of the laser cavity. The center wavelength is not the middle value between the extremities of the swept range, but rather an average of weighted on the optical power, given by:

$$lambda_0 = \frac{1}{P} \int p(\lambda) \lambda \delta \lambda \tag{33}$$

Here, P represents the total power output of the laser, and $p(\lambda)$ power for each wavelength.

In Section 2.3.3 the relation between absorption, scattering and the wavelength of incident light was presented, and it was mentioned that good compromise between scattering and absorption needs to be met. These two phenomena vary differently with wavelength. Its worth noting that the center wavelength of the source is located at a local minimum for the absorption coefficient, as signaled in Figure 2.4. Also to be pointed out is the fact that there are other minima. However, they are either of a higher wavelength, and therefore less prone to scattering, but significantly more prone to absorption (the closest local minimum has an absorption coefficient nearly one order of magnitude higher than at 1060 nm); or can be found at a lower wavelength, and are therefore more susceptible to scattering.

Another fundamental aspect of OCT which depends on the wavelength is the axial resolution of the system. Recalling from Section 2.6.1, it depends on the coherence length of the source, which is proportional to $\frac{\lambda_0{}^2}{\Delta\lambda}$. For this

Parameter	Value
Wavelength Range	985 - 1095 nm
Central Wavelength	1060 nm
Sweep Frequency	100 kHz
Average Output Power	15 mW
Minimum Coherence Length	10 mm
Typical Coherence Length	12 mm
Scan Range in Air	3.7 mm
Maximum Samples	1510
Selected number of samples	1376
% of Bandwidth used	91 %
Duty Cycle	45 %
Estimated clock frequency	310 MHz (±20 % variation)

Table 3.1: Axsun Technologies Swept Source Engine Model SSOCT-1060 specifications

source, the theoretical axial resolution provided is:

$$\sigma_z = \frac{2\ln 2}{\pi}\frac{{\lambda_0}^2}{\Delta\lambda} = \frac{2\ln 2}{\pi}\frac{1060^2}{110} \approx 4.51\ \mu m \tag{34}$$

Using 1376 samples, as is the case, the maximum theoretical depth is:

$$\Delta_z = N_{points} \times \sigma_z \approx 1376 \times 4.51 = 6.2\ mm \tag{35}$$

These are quite decent values, and fit the purpose of the device well. It is of no interest to achieve much higher axial depths. The purpose of the device is to study the eye of small animals, mice and rats. The average eye of rats, the largest animal of the two, has a complete axial length around 5.98 mm [52]. This is smaller than the maximum depth achievable with this laser source. In addition, the theoretical maximum resolution is quite good, using a lower wavelength to improve the resolution would mean increased susceptibility to scattering together with lower maximum depth. As such, this source achieves a good balance in both aspects.

The laser source provides two other signals in addition to the laser output. These are the Sweep Trigger and Clock signals.

The purpose of the Sweep Trigger is to enable the synchronization of the beginning of each A-Scan at the laser source with the rest of the acquisition process. It is a TTL wave which changes from low to high state when the sweeping process begins, and returns to the low state after nearly 10 μs, to

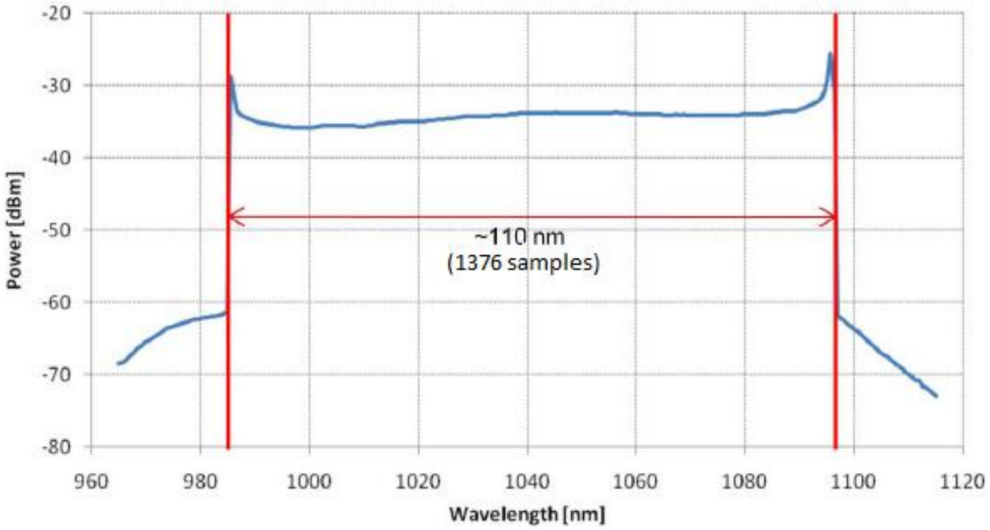

Figure 3.2: Power spectrum from the Axsun Technologies Swept Source Engine Model SSOCT-1060. [4]

return almost immediately to high state, signaling the beginning of a new sweep. This signal is repeated at 100 kHz, similarly to the sweeping frequency of the source, and dictates the A-Scan generation rate.

The clock signal provides additional input on the wavelength sweeping. It's this signal that controls the acquisition of each individual sample by signalling the correct times for acquisition to occur. It oscillates with an average frequency of 310 MHz, varying $\pm 20\%$ on its frequencies to linearize the acquisition in the k-space, and matching the 110 nm swept range to the acquired samples. This is necessary because the generated interference signal is evenly distributed in time, (λ space), but non-linearly distributed in the k-space. In order to perform the inverse Fourier transform, the distribution needs to be corrected to be evenly distributed in the k-space, which is achieved by resorting to the non-linear clock to signal acquisition times. After all the samples have been acquired, the clock signal falls back to a slower, constant behaviour, a dummy clock, which fills the gap between the end of one acquisition and the start of another.

Figure 3.3 shows the Trigger, optical power and Clock signal throughout two full sweeping periods.

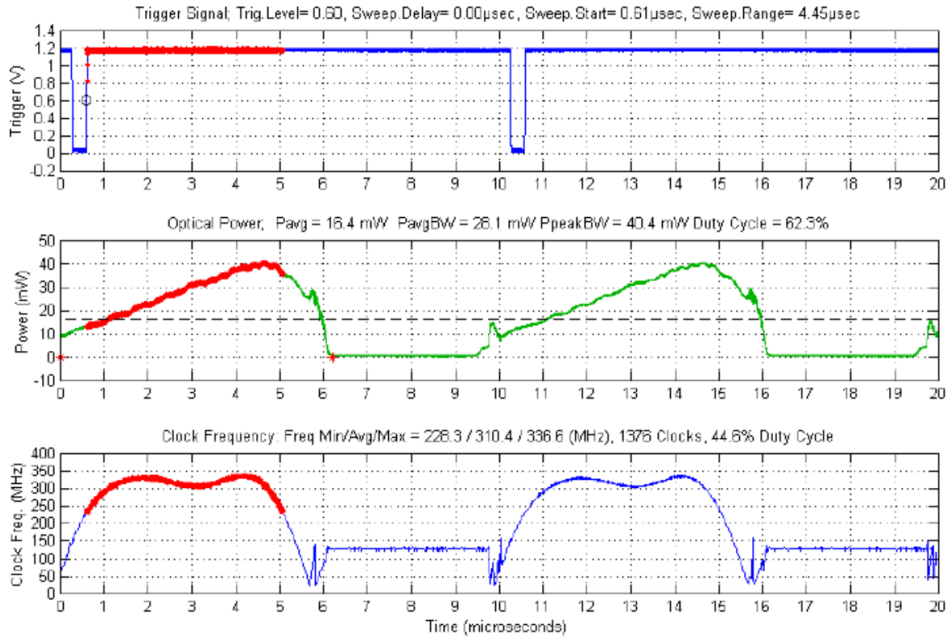

Figure 3.3: From top to bottom: Trigger, optical power spectrum and clock signal from the Axsun Technologies Swept Source Engine Model SSOCT-1060. [4]

3.3 Balanced detector

The main process by which OCT is able to acquire three dimensional data about a given translucent structure is by analysis of the interference pattern generated by the backscattered light from a given sample and a reference mirror. This pattern can be accessed by means of a photodetector continuously measuring incident light during the duration of a laser sweep. For this purpose, the Thorlabs PDB145C Balanced Amplified Photodetector is used [62]. It consists of two well-matched photodiodes and a low noise, high speed transimpedance amplifier. The produced output is a voltage proportional to the difference between the two generated photocurrents, originating from two input optical signals.

The photodetector has two input connections, *INPUT+* and *INPUT-*, two removable FC adapters, through which the optical input fibers are connected to the photodiodes.

Three different output connections are available, namely *MONITOR+*, *MONITOR-*, and *RF OUTPUT*. *MONITOR+* and *MONITOR-* are useful to monitor the *INPUT+* and *INPUT-* power levels. They are low frequency outputs and not suitable for measuring fast changes.

Parameter	Value
Operating Wavelength Range	900 - 1400 nm
Photodiode Responsivity at 1060 nm	0.72 A/W
RF OUTPUT Bandwidth	0 - 400 MHz
RF OUTPUT Transimpedance Gain	10×10^3 V/A
RF OUTPUT Voltage Range (High impedance loads)	±3.8 V
RF OUTPUT Voltage Range (50Ω loads)	±1.6 V
RF OUTPUT Impedance	50 Ω
Common Mode Rejection Ratio (CMMR)	> 25dB
Overall Output Voltage Noise	< 2.0 mV (RMS)
Damage Threshold	5mW

Table 3.2: Thorlabs PDB145C Balanced Amplifier Photodetector specifications

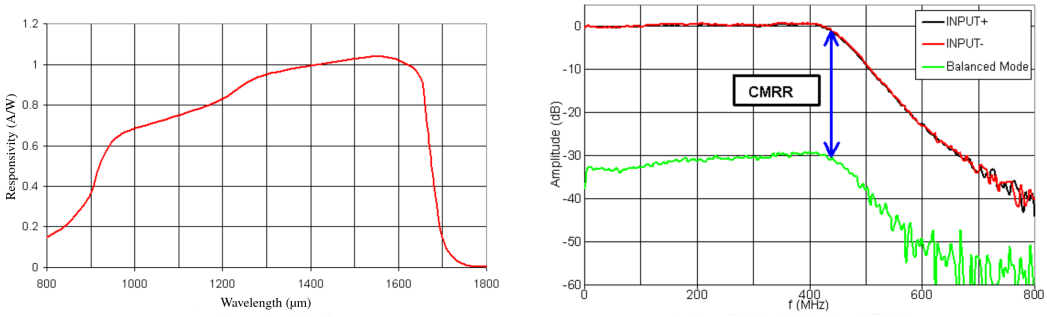

(a) (b)

Figure 3.4: PDB145C wavelength response (a) and CMMR (b). [62]

RF OUTPUT provides a voltage proportional to the difference between the photocurrents in the photodiodes, with a maximum voltage range of ±3.6 V or ±1.8 V, for high impedance or 50 Ω impedance loads, respectively. The voltage produced is given by:

$$U_{RFOUTPUT} = (P_{opt,INPUT+} - P_{opt,INPUT-}) \times \Re(\lambda) \times G \qquad (36)$$

In this equation, $P_{opt,INPUT+}$ and $P_{opt,INPUT-}$ are the optical input power at *INPUT+* and *INPUT-*, respectively; $\Re(\lambda)$ is the responsivity of the detector at the wavelength at the inputs; and G is the transimpedance gain.

Using a balanced detector has several advantages in this case, such as greatly diminishing the DC component of the acquired signal, due to a high CMMR. It also strongly attenuates the excess photon noise.

The performance of the balanced photodetector can potentially impact the maximum axial range of the OCT system, if the bandwidth of the detector is not adequate for detecting the changes in the interference signal. The maximum frequency of the OCT signal is proportional to the frequency of the source's sweep frequency f_{sweep}, the sweep interval Δk and the maximum path length difference z_{max}. The maximum signal frequency is given by:

$$f_{max} = \Delta k \times f_{sweep} \times \frac{z_{max}}{\pi} \tag{37}$$

The sweep frequency is given by the source, 100 kHz. The maximum length can be calculated from the source's specifications, as shown in Equation (35). All that is left is to find Δk, which can be found by considering the full swept range $\Delta\lambda$, 110 nm, and the center wavelength λ_0, 1060 nm, through the expression [68]:

$$\Delta k = 2\pi \left(\frac{1}{\lambda_0 - \frac{\Delta\lambda}{2}} - \frac{1}{\lambda_0 + \frac{\Delta\lambda}{2}} \right) = 6.17 \times 10^{-4}\ rad/nm \tag{38}$$

Using equation (37) yields a maximum frequency of 122.0 MHz for the OCT signal, which is far below the limit of the detector's bandwidth, 400 MHz.

3.4 DAQ board

The Digital Acquisition (DAQ) board is responsible for acquiring the analog data from the photodetector, converting it to digital form and sending it to be processed and stored in the host computer. It needs to be fast and reliable to keep up with the acquisition speed without losses. Assuming that A-Scans are generated at 100 kHz, and each one contains 1376 samples, that means 137.6 million samples are generated every second while the system is working.

The Innovative Integration X5-400M XMC Module is used to handle all acquisition tasks [82]. It is coupled with a PCI Express Host Interface to connect the host PC and the X5-400M board. This interface provides an 8-lane interface, with 2.5Gb/s full duplex link to the host computer per lane, allowing for sustained transfer speeds of 1 GB/s. It is completely compatible with standard PCI Express connections, present is most modern PCs.

As seen from Table 3.3, the board is capable of acquiring a large enough number of samples and of transmitting data to the host PC memory at high speed. These are crucial characteristics. If the data is produced at a higher rate than that of transmission, the board memory may become full before

Feature
Xilinx Virtex5 SX95T FPGA
512 MB DDR2 DRAM
4 MB QDR-II SRAM
Two 400 MSPS, 14-bit A/D channels
Two 500 MSPS, 16-bit DAC channels
SMA inputs and outputs, + 1V, 50 Ω
Internal or External Clock and Trigger
8-lane PCI Express Host Interface
Data transfer to host memory >1GB/s

Table 3.3: Innovative Integration X5-400M specifications

the end of the acquisition, limiting the amount of data that can be acquired in one sitting. If, however, the data is transferred at high enough speed, the size limit is instead defined by the host, which typically has a much larger amount of available memory. Also important is the fact that it allows both external trigger and clock, as it is required for syncing acquisition with the laser source.

Data packaging can be performed in either continuous acquisition or framed acquisition. In the first case, acquisition is enabled whenever the trigger is enabled, with samples being acquired when the trigger is true and the clock signal presents a rising edge. In the second case, each frame contains a preset amount of samples to be acquired. When a rising edge of the trigger appears, acquisition becomes enabled, and samples are acquired when the clock rises. However, acquisition stops after the predefined number of samples is acquired, until the trigger presents another rising edge. It's important to notice that, in framed mode, acquisition depends only on the rising edges of the trigger. If the trigger is set to false and the samples are not yet collected, the acquisition still does not stop until all the samples are ready.

Framed mode is useful for this OCT system, as the number of samples in an A-Scan is always the same, 1376. A frame will always contain a complete A-Scan. However, 1376 is not a multiple of 256. This means that the framed mode must be set to acquire the next multiple of 256, which is 1536. Thus, each frame needs to have 160 extra samples, which are of no use, as they are acquired after the Clock has stabilized at a lower , constant pace, waiting for the laser to start again. This is not a problem, as it can be corrected in software after the physical acquisition of data.

3.5 Galvanometer Scanning System

The laser source itself can only retrieve data in the axial direction of the the bem. In order to acquire data on 2 or 3-dimensional structures, the beam needs to be scanned in two transversal directions. The mechanism responsible for this needs to be capable of handling this task with speed and precision. This can be done by redirecting the beam using two mirrors whose position is controlled by a two-axis galvanometer system, which allows the beam's position to be controlled in the vertical and horizontal directions, thus making possible the acquisition of B-Scans and volumes.

In this work this task is handled by making use of a Thorlabs GVS002 Dual Axis Galvanometer System. It consists of two galvanometers acting as motors, each controlled by a driver card and joined with a protected silver mirror and individual photo-detector. The photodetector is used to generate information about the current position of the mirrors. The silver mirrors' reflectance is around 97% for wavelengths between 970 and 1100 nm.

Parameter	Value
Scan Angle Range	$\pm 12.5^{o}$
Input Position Signal Range	± 10 V
Input Position Signal Scale Factor	0.5 V/^{o}, 0.8 V/^{o} or 1.0 V/^{o}
Full Scale Bandwidth:	
Square Wave	100 Hz
Sine Wave	250 Hz
Sawtooth Wave	175 Hz
Small Angle Bandwidth:	
Sine Wave	1 kHz
Small Angle Response	300 μs
Resolution	0.0008^{o}
Linearity	99.9 %
Output Position Scale Factor	0.5 V/^{o}

Table 3.4: Thorlabs GVS002 Galvanometer System specifications

Galvanometers are instruments used to detect and measure small electric currents. They use a coil of wire and a permanent magnet. When a current is sent through the wire, the coil is forced to turn, with the angle being proportional to the current. Being easily programmable to achieve different

scanning resolutions, Galvanometer Scanners are frequently used in commercial and medical applications, such as laser etching, laser measurements and confocal microscopy [22].

The galvanometer's speed can be a bottleneck in the acquisition process. The rate of A-Scan acquisition is limited by the laser source, however for B-scans and volumes that is not the case. The mirrors need to change position between consecutive A-Scans, and if this motion takes more than 10 ms, it is slow enough to prevent acquiring consecutive A-Scans. A good example of this is the process used to acquire volumes and or B-Scans when this work started. The horizontal galvanometer was controlled by a signal generator. This generator provided a sawtooth wave as input. Ideally, it should be a wave with a rising phase duration corresponding to all the A-Scans acquired in a B-Scan, 10 $\mu s \times N_{A-Scans}$, and an almost instantaneous drop, that would allow another B-Scan to be acquired immediately. However, the galvanometers do not move instantaneously. In fact, the GVS002 specifications indicate that even for small angles the response time is $300\mu s$, which is enough time to perform 30 A-Scans. When scanning larger angles the response time is even higher, as shown by [77]. It takes approximately $1ms$ for the galvanometers to return to their initial position after a full range scan. This process wastes enough time to perform 100 A-Scans, and is repeated for every B-Scan. For a B-Scan containing 512 B-Scans, this extends the time needed to perform consecutive B-Scans by almost 20%.

Lateral resolution can also be dependent on the galvanometers' performance, as it cannot be better than the beam's smallest lateral displacement. In this case, the smallest angle the galvanometers can move is 0.0008^{o}. The resulting minimum lateral displacement is dependent on the optical components along the beam path. However, this is likely a limit too small to be of any concern. For instance, assuming that a range of 5 degrees completely scans across an object of with 25 mm, the distance associated with the minimum step mentioned above would be 4 μm, even smaller than the axial resolution of the device. In practice, the full scale of 5 degrees typically allows scanning a distance smaller than 25 mm, so this would be an upper limit to the minimum step that the galvanometers can provide. In a previous evaluation of the performance of this system, the lateral resolution was found to be around 10 μm [9], where the author compared the result to the theoretical value of 6.5 μm. This means that the resolution of the galvanometers should not affect the lateral resolution, as it is less than half of the estimated lateral resolution, and less than 1.5 times the theoretical lateral resolution.

3.6 Deprecated devices

3.6.1 Signal generator

The signal generator was used to control the horizontal galvanometers. It is no longer of use, and has been replaced by the new control module, as will be explained in Chapter 5.

As mentioned before, the galvanometers are controlled by an input voltage which is proportional to the position to which they are to be moved. This means that generating voltage waveforms allows for continuously varying their position, thus scanning through a given range. This was the purpose of the AFG3101 Arbitrary Function Generator by Tektronix [2].

Parameter	Value
Sampling Rate	1 GS/s
Frequency Range	1 mHz to 100 MHz
Frequency Resolution	1 Hz
Amplitude Range	20 mV_{pp} to 10 V_{pp}
Amplitude Resolution	$0,1$ mV_{pp}
Symmetry Range	0.0% to 100.0%
Phase Range	$-180°$ to $180°$
DC Offset Range	± 5 V

Table 3.5: Tektronix AFG3101 Arbitrary Function Generator specifications.

As can be seen form Table 3.5, this device is more than capable of producing the needed waveforms to manage the horizontal galvanometer movement. However, it was replaced in its functions not for improper specifications, but for a matter of usability. Using a module which controls both galvanometers and synchronizes them with the Trigger signal has substantial advantages, particularly taking into account that the interaction with said module can be performed from within the software in the host computer. Thus, the developed technical solution described in Chapter 5 replaced this component, in order to achieve a better overall synchronization among components and to a more practical way to control the acquisition process parameters.

3.6.2 Digital delay and Pulse generator

The Sweep Trigger which leaves the Axsun laser source is a TTL signal with voltages of 0 V and 1.2 V. On the other hand, the X5-400M board

accepts input triggers with voltages of 0 V and 5 V. This range is a few times higher than the Trigger the laser source outputs. Therefore, a need to amplify the outgoing Trigger exists, so it conforms to the requirements of the DAQ board. In addition, while the Trigger and Optical output are synchronized as they leave the Axsun source, the path the light makes as it travels through the system takes time, and so a delay is needed on the trigger to keep them synchronized. This delay was determined in a previous work to be $\Delta t = 90\ ns$ [3].

The Digital Delay and Pulse Generator DG535 from Stanford Research Systems [19] was used to to account for both these issues, as it receives the original trigger from the Axsun Source and outputs a similar signal, but delayed and amplified.

This device is no longer needed as the module described in Chapter 5 acts as the bridge between the laser source and the DAQ board for the Trigger, applying all necessary changes.

4 | Illumination and camera module

4.1 Options considered

In order to figure the best course of action, several options were considered. Some of them were meant to take advantage of existing hardware, while others focused merely on the best and simplest way of achieving the goal of having a live video feed of the OCT target. Several options considered are presented in this section.

4.1.1 Existing setup

As an infra-red light source was already present in the initial OCT setup (the Axsun Laser source), one possibility was to use it to get a front facing image of the OCT target area. One method of doing this was already implemented in the existing software, where it summed over each acquired A-Scan Fast Fourier Transform (FFT), to present a flat reflectivity profile of the target. However, this could not be done in real time, as the processing needed to do this takes a long time. Even using a low number of A-Scans and B-Scans to accelerate the process was not enough, and besides being slow it also caused a strong loss of quality in the image.

Another issue is that while the system is generating images in this process, the galvanometers have necessarily to be both always repeatedly scanning a given area. There is no possibility to keep watching a given A-Scan or B-Scan while using this method to look at the target's positioning.

4.1.2 Infra-Red Camera

Another solution that would take advantage of the pre-existing light source would be to use an Infra-Red (IR) Camera, in order to monitor in

real time the area scanned by the laser.The laser light could serve to illuminate the target area. If vertical scanning was fast enough in relation to the camera frame rate, the scanned area would appear to be illuminated. Assuming a frame rate of 15 fps, which would be enough for the purpose of this work, that would mean that a scan of the target area would have to take at most:

$$T_{frame} = \frac{1}{15} \approx 66\ ms \tag{39}$$

When this work was started, the best case scenario for the time needed to scan a given area was given by:

$$T_{scan} = T_x \times N_{B-Scans} \tag{40}$$

In that eqution, T_x is the time the horizontal galvanometer takes to perform a full sweep, including going back to its starting position, and $N_{B-Scans}$ is the total number of B-Scans. The process of the horizontal galvanometer returning to its initial position takes, by itself, 1 ms. The galvanometers top frequencies at full bandwidth are also known from Table 3.4. Using a sawtooth wave, the top frequency would be, with an ideal sawtooth, 175 Hz, meaning each full-scale horizontal scan would take 5.71 ms. As such, only around 10 B-Scans could occur before the frame ended. This is a very low number, and depending on the size of the beam, and the area scanned, it would most likely not be enough to get uniform lighting.

Other potential problem with this approach is that the camera would have to receive light from the same source as the photodetector, which could possibly require that too much light would have to be redirected from the main beam to capture an image with the camera. This could be done, for instance, with a beamsplitter, but it might require giving up too much quality in the optical signal.

Lastly, this imaging mode, as the one previously mentioned, restricts the behavior of the system while acquiring live images. The galvanometers have to be repeatedly scanning the same area. Focusing on a particular point wouldn't be possible, unless that point was contained in one of the few B-Scans.

4.1.3 Near-camera lighting with Color Camera

To avoid the problems mentioned above, it was decided that the best option would be to use an external light source to illuminate the target.

A dichroic mirror was place in the laser beam's path. The dichroic mirror has a high reflectivity for visible wavelengths, but it's transparent to infra-red

light. The reflection of the target can then be watched by placing the mirror at a 45º angle with the beam, while the beam itself passes through the mirror, one time while going towards the target and another when backscattered by it. With a camera placed aiming at this mirror, it was possible to get a live feed of the target area. However, this approach requires an additional method of illuminating the sample, as the light existing in a room is not enough to get a clear view. This would be particularly true if trying to view the eye of a small animal.

The first tried hypothesis was to place a LED light source near the camera, far away from the target, so that the light would be far away from the target. This way, when the light reached the target it would be approximately perpendicular to it. However, this method produced too much unwanted reflections in the components placed through the path, so it was discarded.

4.1.4 Near-target lighting with Color Camera

The second method considered toward the illumination of the target consisted in placing several LED lights near the target, in circular fashion. This succeeded in allowing to acquire visible images of a target with reasonable quality. However, light was not evenly distributed, and focused on particular points opposed to the LED. Another issue with this method was that the light did not hit the target perpendicularly, so in the case of the eyes of small animals, not much light would be able to enter it. There would also be no way of controlling the size of the illuminated area.

However, this method would still prove useful in different circumstances. When mounting the module described in this chapter from scratch, or when reassembling it, it was useful to be able to look at a given target to find the ideal positions of the components. This method proved to be the most reliable to make this calibration, as it is hard to properly mount the camera without a lighting system and it was far easier to assemble and experiment with the final illumination system with the camera arm fully assembled.

4.1.5 Perpendicular lighting with Color Camera

The final alternative allowed to mostly solve all the problems in the options mentioned above. Between the camera and the dichroic mirror, a 50:50 beamsplitter is placed. Aimed at this beamsplitter is a LED light source, focused by a pair of lenses and with a pupil diagram to control the amount of light and its radius.

This assembly allows for the light to be perpendicularly directed at the target, controlling its area and focus. This solves all the problems of the near

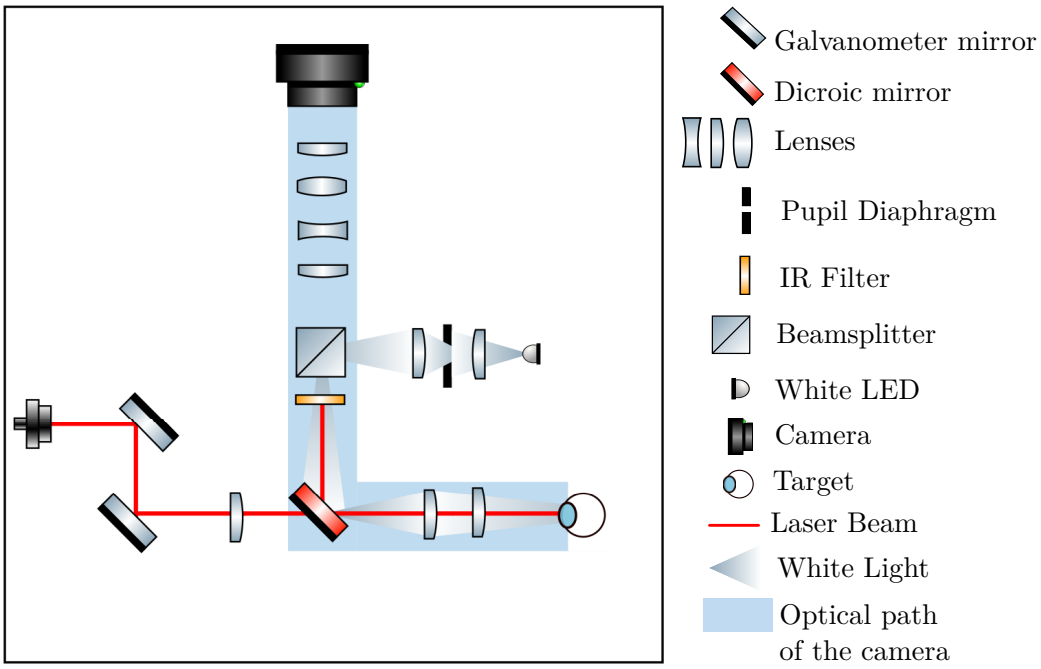

Figure 4.1: Diagram of the camera and illumination module.

target lighting system. On the other hand, by properly and independently controlling the light focus and radius, the problems mentioned in the near camera lighting are mostly solved.

4.2 Experimental setup

The final setup's schematic is represented in Figure 4.1. It is based on the solution described in Section 4.1.5. The main section of the OCT targeting arm remains mostly the same, with two differences: the addition of a dichroic mirror in the path of the OCT laser, and the substitution of one lens for a similar model with anti-reflective coating. The dichroic mirror, described in detail in Section 4.2.1, is placed in the laser beam's path, making with its surface at an angle of 45 degrees with the main axis connecting the target and the beam's exit. This way, the camera can be placed perpendicularly to the beam's path, directed at the mirror, so it can acquire images of the reflection of the target on the dichroic mirror.

Due to the nature of the dichroic mirror, the light reflected to the camera is mostly in the visible spectrum. However, some of the beam is still reflected, and a IR-Filter is needed to prevent it from interfering in the image acquisition.

Lastly, as the camera is somewhat far from the target and it has no inherent capabilities to zoom in on it, the implementation of a system to magnify the image is required. This is achieved by using a set of lenses placed between the IR-filter and the camera.

Illumination is another important part of the setup, as without proper lighting, not much can be seen through the camera. Ambient lighting is hardly enough to allow seeing anything without optimal circumstances. When it comes to the eyes of small rodents, the lighting requirements are far more demanding. Their pupils are typically only a few millimeters wide, which means that if the light is not perpendicular, proper lighting is impossible. In addition, it is desirable to be able to control the size of the illuminated area. If the illuminated area is much bigger than the rodent's pupil, light may be reflected by anything other than the inside of the eye of the rodent. This is not important if what is caught is not particularly reflective, but can otherwise limit the ability to image the inside of the eye.

Achieving perpendicular illumination means that the path the light follows to the eye should be mostly the same as it follows from the eye to the camera. This can be achieved in two ways: by having the light source placed very near the camera, far away from the target, which would mean the light's angle of incidence would be very close to the axis between the camera and target; by having light come from some other direction and mix it in the optical path. The first is the method that was tried in Section 4.1.3; the second is the one used and mentioned in Section 4.1.5. By placing a beamsplitter between the camera and the dichroic, it is possible to have light be directed at the beamsplitter, which then redirects it according to the main axis between the camera and the target. This means the light hits the target perpendicularly and no light strays toward the camera (unless reflected by something along the way).

In order to control the size of the illuminated area, a system of two convex lenses and one pupil diaphragm are used. Currently the source used is a white LED. The LED is directed at a convex lens which focuses the beam toward the pupil diaphragm. The pupil diaphragm provides a controllable opening which can limit the size of the light source as seen from the target. This opening is then focused on the target by a second convex lens.

The focus of both the camera and illumination are dependent on the objective lenses used by the OCT. Due to the current experimental nature of the OCT system, it can be expected that some changes might occasionally be needed. One of the potential changes is related to changing the distances between the optical components of the system. Ideally, the system should be set up optimally and only be subject to small adjustements for maintenance. However, as it may not be the case, the mounted lens assembly allows easily

adjusting the focus of the camera to account for minor adjustments in the optical path of the OCT beam. Likewise, the illumination system can be easily adapted for small changes.

4.2.1 Thorlabs DMLP950

The dichroic is a fundamental piece of the camera and illumination module, as it is the component which enables viewing the target in the camera without compromising the performance of the OCT system.

The dichroic mirror used is a Thorlabs DMLP950 [44]. It is a longpass filter which reflects visible light and includes an anti-reflective coating for the IR range. The specifications for this module can be found in Table 4.1.

Parameter	Value
Cutoff Wavelength	950 nm
Transmission Band	990 - 1600 nm
Reflection Band	420 - 900 nm
AR Coating Range	932-1700 nm
Incident Angle	45º
Substrate Material	UV Fused Silica

Table 4.1: Thorlabs DMLP950 specifications.

The absolute transmission over the transmission band is higher than 85%, and the absolute reflection over the reflection band is higher than 90%.

As mentioned in the previous section, it can be observed that some light of the OCT laser beam ends up being reflected at the dichroic. This can be justified by the fact that neither the transmission nor the reflectance ever reach 100%. Besides that, the specifications are made for an incident angle of 45º, which may be slightly off. Lastly, the transmission band includes wavelengths between 990-1600 nm, but the Axsun Laser Source produces wavelengths starting at 985 nm.

4.2.2 Thorlabs AL2520M-A

A mounted aspheric Thorlabs AL2520M [42] was already present in the OCT system. The used model had no anti-reflective coating, neither for visible light or infra-red. This led to strong reflections visible when illuminating the target, making it impossible to see clearly with the camera a large area of the target. Such behavior is undesirable for the purpose of this work, and

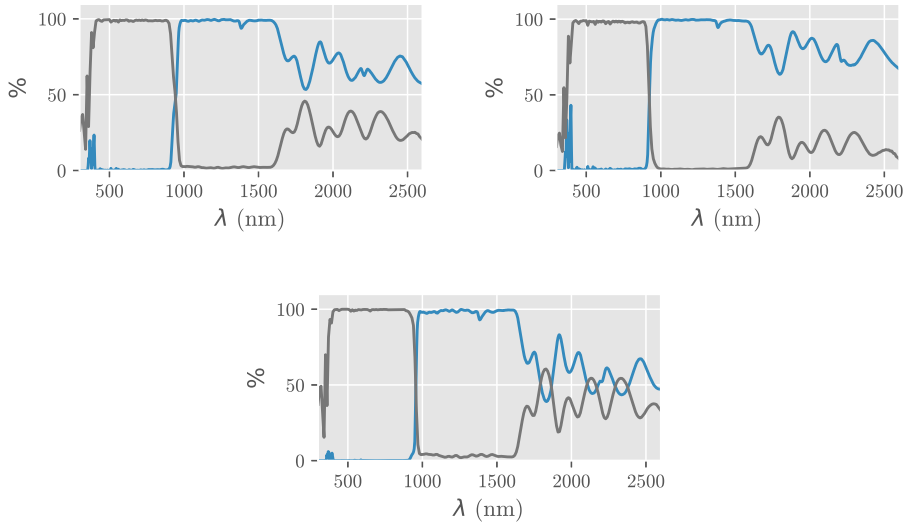

Figure 4.2: Transmission and reflectance curves for the DMLP950. Transmission is shown in blue, and reflectance in brown. [44]

the best course of action was to replace the lens, so that it no longer cripples the ability to see the target clearly with the camera.

The Thorlabs AL2520M-A is a lens with the same characteristics of the Thorlabs AL2520M, but with an additional anti-reflective coating for visible light [43]. This should allow maintaining similar performance in the OCT system while enabling a large quality improvement in the captation of images with the camera.

Parameter	Value
Effective focal length	20.0 mm
AR Coating	350 - 700nm
Numerical Aperture	0.54
Working Distance	12.0 mm
Design Wavelength	780 nm
Glass	S-LAH64

Table 4.2: Thorlabs AL2520M-A specifications.

The reflectance of this lens for wavelengths higher than 850 nm is not specified by the manufacturer. However, it appears to grow linearly with wavelength after 700 nm and at 850 nm it is already around 6%. If the

linear growth continues up to 1100 nm, a reflectance of around 15% should be expected for the range of wavelengths produced by the Axsun laser source. This will likely be higher than the previously used lens, altough no data was found referring to its reflectance.

4.2.3 Edmund Optics IR Cut-Off Filter

As mentioned before, some of the backscattered light from the laser beam ends up being redirected by the dichroic mirror toward the camera. Ideally this would not happen, if the dichroic worked perfectly, but it is not a deal-breaker. The camera was also not made to detect infra-red light, as it was built to serve as a common webcam. However, camera sensors are typically very sensitive to infra-red light, requiring an IR filter to produce decent images in the visible range. It could be the case that the filter in the camera is not good enough to completely filter out IR light with the intensity of the reflection of the backscattered laser beam.

The beam is reflected by the dichroic on its way back toward the photodetector, after being backscattered either by the target or any optical components along the way. If the backscattered light originated only from the target, this could actually be beneficial towards the purpose of the camera and illumination module. The reflection of the current position of the laser would be a simple way to get feedback of the current scanning position in the target. In fact, due to the time it takes the camera to acquire a single frame, which is typically around $1/30 \approx 0.033\ s = 33\ ms$, it should be able capture images highlighting the positions of a few B-Scans. This would in fact be very useful to help targeting the intended areas in samples. The problem is that the lenses along the beam's path also backscatter some of the light, which ends up obfuscating any potential useful information that could be present. Examples of this can be seen in Figures **??**. To find the origin of the laser reflections, the components were removed starting with the target and going backwards in the optical path, until no reflections could be seen in the camera. It was found that the major cause of backscattering were the lenses, particularly Thorlabs AL2520M and AL2520M-A.

The simplest solution for this issue was to simply filter out the IR light before it reached the camera, by including an IR filter in the optical path of the camera. The inclusion of the filter does not affect the loss in the beam intensity reaching the photodetector, nor does it allow filtering only the light reflected from the lenses, as would be ideal. However, it removes any trace of IR light, and provides a clear image of the target, which is good enough for the purpose of this work.

The used filter was a 20 mm Square IR Cut-Off Filter manufactured

Parameter	Value
Coating	Traditional Coated
Cut-off Wavelength	710 nm
Operating Temperature	250 ºC
Wavelength Range	480 - 1200 nm
Transmission average for 480 - 680 nm	$> 85\%$
Transmission average for 680 - 740 nm	50%
Transmission average for 740 - 1200 nm	$< 10\%$

Table 4.3: Edmund Optics' IR Cut-Off Filter specifications.

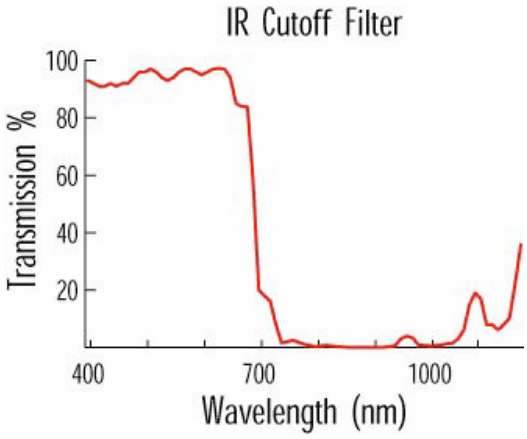

Figure 4.3: Transmission curve for the wavelength range of 400 to 1200 nm.[59]

by Edmund Optics [59]. It filters wavelengths higher than 700 nm, up to 1200 nm, which includes all of the range of the Axsun laser source. The transmission curve is represented in Figure 4.3. As it can be seen, the filter is perfectly suited for filtering the IR light reflected by the dichroic. A comparison of images with and without the filter is available in Figure **??**.

4.2.4 Melles Griot Non-Polarizing Plate Beamsplitter 03BTL023

The beamsplitter is the key for properly directing the light toward the target. It should ideally transmit and reflect 50% of the incident light, both coming from the light source and from the target. The operating range should be for visible light, as that is the lighting used to illuminate the target.

The beamsplitter used for this purpose is the Melles Griot Non-Polarizing Plate Beamsplitter 03BTL023 [58]. This is a beamsplitter designed for use with lasers, working with precision at a given wavelength. It is also designed for maintaining the polarization of incident light, though that is not particularly relevant in this work.

Being optimized for a given wavelength means it will not perform optimally through all the visible range. Some consequences of this fact include improper lighting. However, among the other components at the laboratory, this was the best choice, due to other constraints. The only other viable option would be a cube beamsplitter, but mounting it in the proper position and angle was severely problematic with the available mountings. Thus the choice was made to use a plate beamsplitter, and the 03BTL023 was the most appropriate choice.

The beamsplitter operates at 514.5 nm, and its transmittance curve is shown in Figure **??**. Besides not being designed for working with the whole range of visible light, its wavelength is distant from red. A visible consequence of using this beamsplitter is that the lighting at the target tends to be a bit more green and blue. This is troublesome, as the general colors in the retinal fundus of eyes are usually closer to red than to green or blue.

Parameter	Value
Diameter	50 $\pm$0.25 mm
Wavelength	514.5 nm
Transmission	50 $\pm$5%
Absorption	<0.5%

Table 4.4: Melles Griot Non-Polarizing Plate Beamsplitter 03BTL023 specifications.

Replacing the beamsplitter in the future may provide an improvement in lighting conditions. A good candidate would be, for instance, the 03BTF023 from Melles Griot. It has the same size and reflectance/transmittance ratio, but is designed for working with visible light. Directly replacing the currently mounted beamsplitter by this one would be trivial and fix the lighting color.

4.2.5 Microsoft® LifeCam VX-500

The camera used in this work is a simple webcam. As the main purpose is to create an easy, intuitive and accurate way to aim the OCT beam at the target, the quality requirements of the camera are not particularly high. It

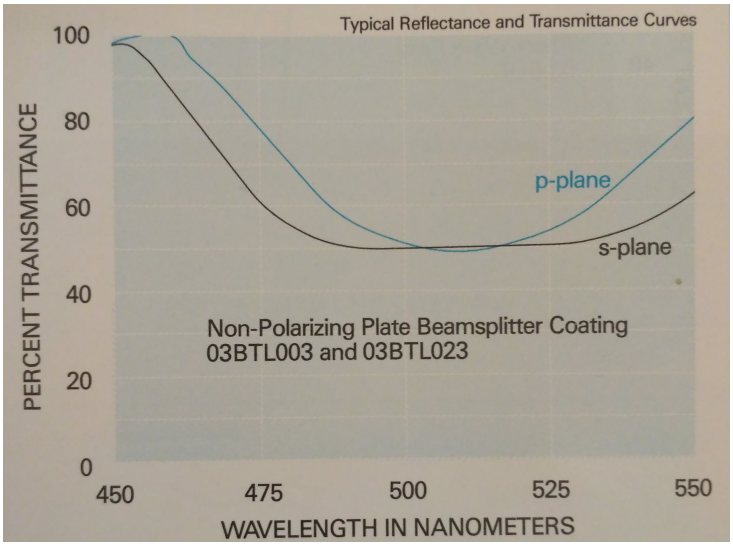

Figure 4.4: Transmission curve of the Melles Griot Non-Polarizing Plate Beamsplitter 03BTL023

just needs to provide images with decent quality at a frame rate high enough to facilitate positioning the target. The model used is the Microsoft® LifeCam VX-500, an inexpensive old model from Microsoft, originally intended for video calls over the Internet. It uses a CMOS VGA sensor, and is capable of providing a video feed at 30 frames per second, at a maximum resolution of 640×480.

Parameter	Value
Interface	USB 2.0
Sensor	CMOS VGA sensor
Video Resolution	640 ×480
Field of View	56º

Table 4.5: Microsoft® LifeCam VX-500 specifications.

The camera includes numerous features, namely automatic control of exposure, white balance and gain. While this could be seen as useful features in a webcam, in this case these features can get in the way. For instance, these features cause the camera to automatically respond to changes in lighting. When replacing targets, or even when removing a target and placing it in position again afterwards, the perceived lighting and colors may be different, due to automatic changes in these settings.

This lack of control over these settings causes multiple images to lack consistency among them, affecting the reproducibility of the same conditions for the acquisition of images. For the intended purpose of previewing the target of the OCT, this issue is not serious. However, in the future this module may be further developed to allow quality imaging of the retinal fundus in small animals. In this case, the lack of control over the imaging parameters would be severely problematic. If this happens, the camera will likely need to be replaced for a better suited device, and likely with better image quality.

4.2.6 Mounted Lens Kits

Lens kits are usually useful for quickly prototyping optical systems. In this work, lenses were required for two purposes: to focus the light into the target, and to magnify the image to be seen on the camera. This was done resorting to two mounted lenses kits from Melles Griot, the Mounted Singlet Lens Kit and the Mounted Achromat Lens Kit [58]. Overall, both kits contain a total of 50 lenses, 40 singlet and 10 achromat. The singlet kit contains 20 plano-convex, 10 bi-convex, 10 plano-concave and 10 bi-concave lenses.

The variety of lenses enables some flexibility in the design of the system.

Parameter	Value
Number of Lenses	40
Design wavelength for plano-convex	587.6 nm
Design wavelength for other lenses	546.1 nm
Design index	1.5187 ±0.001
Transmission range	400 - 2300 nm

Table 4.6: Melles Griot Mounted Singlet Lens Kit Specifications.

Two lenses were used for conveying the light from the LED source into the target, and four were used for the camera to zoom in on the target.

The light focusing lenses are represented on Figure 4.5. Here, light travels from left to right. The leftmost lens is a planoconvex lens with 25 mm focal length, for conveying the light from the LED light source to the pupil diaphragm. The next lens in the path is an achromat with a focal length of 40 mm, and is used to focus the light exiting the pupil diaphragm into to the target. The last lens is the AL2520M-A, already within the optical path of the OCT beam's path.

Parameter	Value
Number of Lenses	10
Design wavelength (blue)	480.0 nm
Design wavelength (green)	546.1 nm
Design wavelength (red)	643.8 nm
Transmission range	400 - 2300 nm

Table 4.7: Melles Griot Mounted Achromat Lens Kit Specifications.

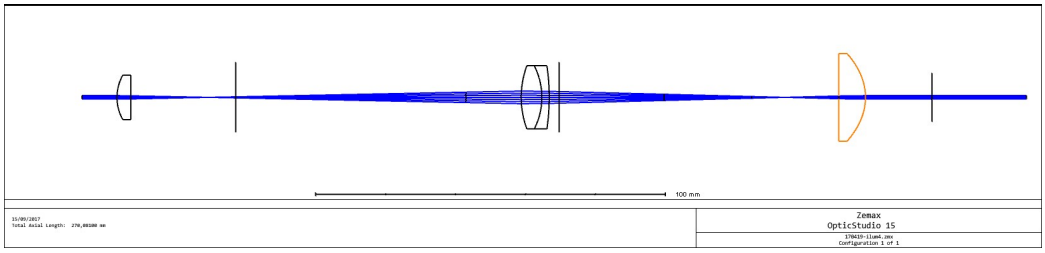

Figure 4.5: Zemax diagram of the light focusing lenses.

The lenses used for zooming the camera in on the target are represented in Figure 4.6. Here, the target is assumed to be on the left end of the diagram, and the camera on the right end. The first lens on the right are a lens with a focal length of 10 mm, which was used in the course of this work to simulate viewing the eye of the small animals, which typically have an total optical power of a few hundred dioptres. In mice, for instance, the total eye power is 520 D [32]. In humans it is 60 D. Although the approximation provided by the lens falls short of the real scenario, it was the best available without resorting systematically to live specimens. The second lens in the path is the AL2520M-A, already presented in

4.3 sec:arlens

. The other four lenses are already outside the OCT beam's path and are responsible for magnifying the images for the camera. Their focal lengths are, from left to right: 60 mm, -75 mm, 40 mm and 40 mm.

The four lenses for magnifying the image, the two used in the illumination system and the one used to add an element of high optical power all came from the two kits by Melles Griot.

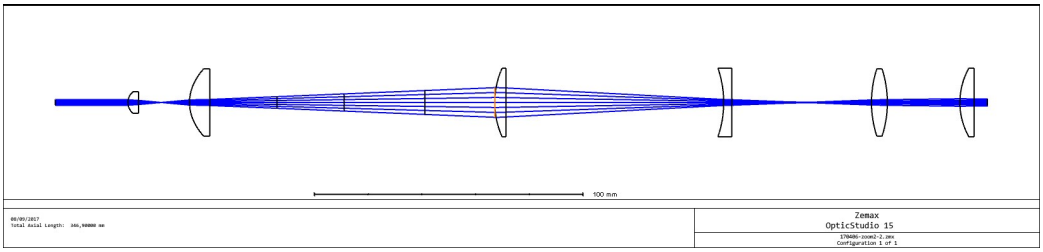

Figure 4.6: Zemax diagram of the camera's zoom lenses.

4.4 Testing and Performance

During the development of the module, testing was constant. It was important to know if the image was distorted, if the illumination was adequate and if the resulting images could be considered adequate for the purpose of previewing the target.

As the targets of the OCT will be the eyes of small animals, it would have been beneficial to test in a mice or rat specimen. Unfortunately, this was not possible to achieve during the course of this work. Therefore, the only tests made were resorting to other targets, such as a Portuguese 0.50€ coin, an OCT fluorescing target[45] and a transparent target with small, parallel stripes. In addition, using a target sheet by Edmund Optics [60], it was possible to estimate the relation between modulation in acquired images and the spatial frequency of the target. While the set of tests run does not replace live testing with an animal target, it still allows knowing if the performance of the module is adequate to its intended purpose.

The three targets (fluorescing, striped and coin) served different purposes during the development, due to their characteristics.

The fluorescent target was used in early stages, mainly for alignment purposes. As it is a bright target with a hole in the center, it was ideal to find and troubleshoot alignment issues, both related to the camera and the illumination.

Alignment was problematic in the early stages of prototyping, due to the mounted setup of the OCT components. This was mainly because the OCT had been mounted in such a way that it could change its vertical angle. Such a setup made it difficult to align components in a way that they could be properly aligned, accompany the mounted arm of the OCT beam when it moved, and not start bending due to limitations in physical support. Ultimately, the setup ended up being changed to a more fixed, robust mounting, which greatly improved the physical stability of the mount and finally allowed achieving proper alignment among all the components.

It no longer can change its vertical angle, but using an adequate multi-axis stand for the small animals is a better way to align the animals with the beam.

The striped target's purpose was different. It was used when setting up the lenses in the camera path, to find the best magnification which did not cause distortion in the image.

Lastly, the coin was used in later stages due to it having a more complex surface structure and patterns, while still being highly reflective. This allowed simultaneously testing the OCT acquisitions while previewing the target with the camera. A different target ideal for testing and troubleshooting the OCT was available, but it was black, and no discernible image could be seen in the camera.

The performance of the illumination and camera system was evaluated in two fronts: experimental determination of the Modulation Transfer Function (MTF) and verification of the uniformity of the incident light on the target.

An important parameter for analyzing the performance of optical systems is the modulation or contrast [36]:

$$M = \frac{I_{Max} - I_{Min}}{I_{Max} + I_{Min}} \tag{41}$$

The MTF relates the spatial frequency of the target and the modulation of the resulting image. Resorting to a series of sinusoidal targets with varying spatial frequencies, the modulation for different spatial frequencies can be determined. The higher the modulation, the better details can be resolved at the given spatial frequency. Thus, the MTF provides a good way to quantify the capability of the system for resolving the details of the image.

As it was already mentioned, a series of sinusoidal targets manufactured by Edmund Optics was used for this purpose. Instead of having lines with sharp edges, these targets use lines made sinusoidal gradients. It was used to test the maximum distinguishable number of line pairs per millimeter. The dimensions and structure of the target are shown in Figure **??**.

After eight line pairs per millimeter it is no longer possible to discern the lines in the image. The chart in Figure 4.7 shows the relation of the contrast between lines and the number of line pairs per millimeter. From this chart, it can immediately be perceived that the contrast is never as high as it would be expected. For a low number of lines per millimeter, the contrast should be near 1. However, it starts at around 0.4. This may be due to several reasons:

- Due to the existing reflections, the area with the image is not one of the most illuminated areas, and as such is particularly susceptible to

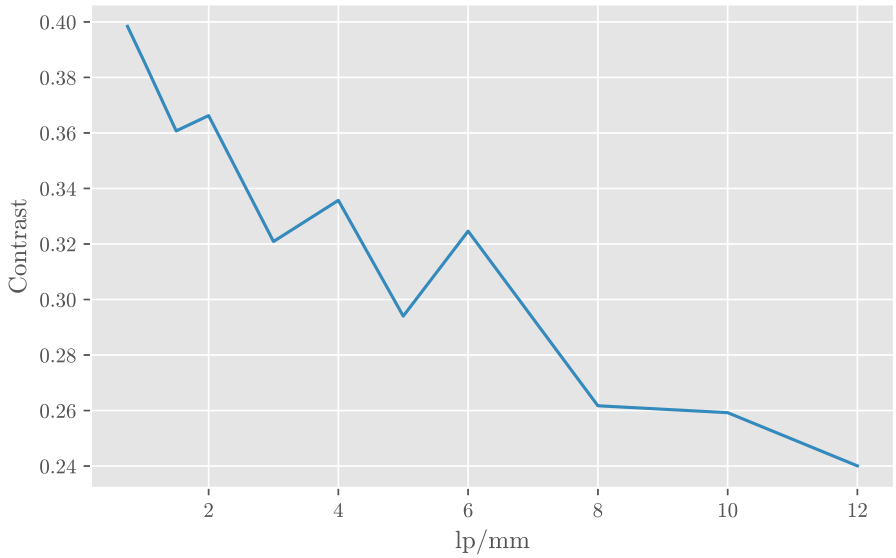

Figure 4.7: Modulation transfer function of the system.

noise. This contributes to the causing details to be lost;

- Using only the grayscale values does not take into account the original image. These values should be normalized against the samples provided on the sides of the target. When imaged, these provide values similar to the ones obtained in the image, and the contrast estimation should be done with these values instead of the grayscale intensities. However, this is difficult to do reliably due to the next item;

- Doing the aforementioned calibration is difficult, particularly due to a problem which also affects the acquisition of the images with different lines. As has been stated, the camera automatically changes settings for optimal viewing, according to its initial design as a webcam. This causes settings to change between the acquisition of different images, making reproducing the same conditions a hard task.

Due to this reasons, it was not possible to get a truly accurate estimation of the MTF. Doing so would likely require a more appropriate camera, which allowed controlling the conditions in order to get reproducible acquisition of images.

As for the uniformity of the light incident on the target, this was tested by capturing and image of a uniform target and measuring the intensity

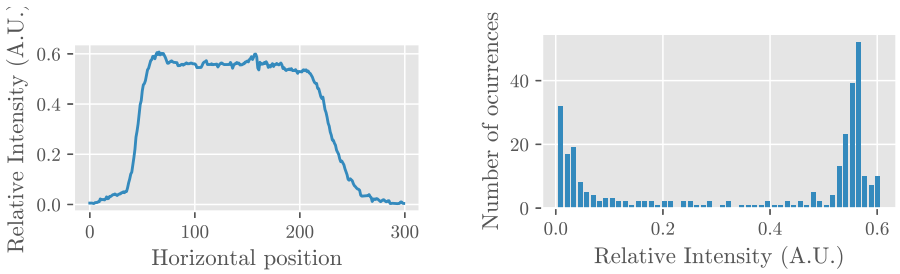

Figure 4.8: Plot and histogram of luminous intensities through a reflection free area of the target.

on the pixels, to see how uniform is the distribution of light. While this measurement is also affected by the reflections, measuring it did not pose much problems.

The measurement was done by targeting a white piece of paper, an studying the relative intensity of the illuminated areas by image processing. To account for the effect of strong reflections, the measurement of uniformity was done in two linear areas that completely crossed through the image: one away from the most intense reflections, an another near it, to compare the effects. The results are shown in Figures 4.8 and 4.9, for the areas without and with reflections. The area on the side is a purposely dark region, as the dichroic and corresponding reflected targets are seen only in the central area of the image. In the image without reflections some small variation in the intensity in the central area can be seen, but lacks a defining shape. Therefore, it is not likely to be due to the lighting. In the image closer to the reflections, a small area of higher intensity can be seen. This is due to the reflection, but otherwise the rest of the light seems evenly distributed. The histograms also show a relatively narrow FWHM for the values related to the illuminated area.

It is fair to say that the uniformity of light distribution seems to be reasonable, and perfectly adequate for its purpose. However, this test only provides an estimation. For proper results, a photodetector should be used to directly determine the distribution of light.

4.5 Impact on the OCT

It is undesirable that the illumination module interferes with the capabilities of the OCT system. However, as some components need to be place in the OCT beam's path, it is unavoidable.

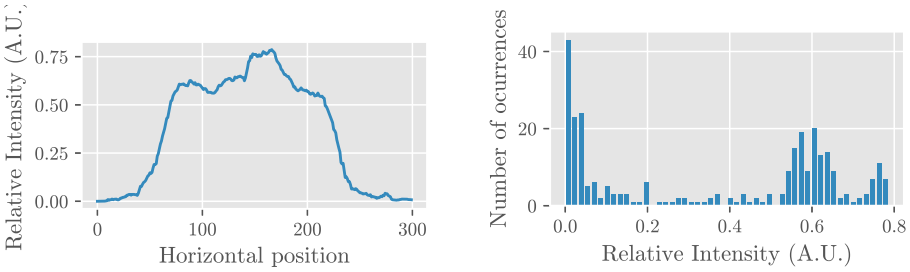

Figure 4.9: Plot and histogram of luminous intensities through an area of the target containing reflections.

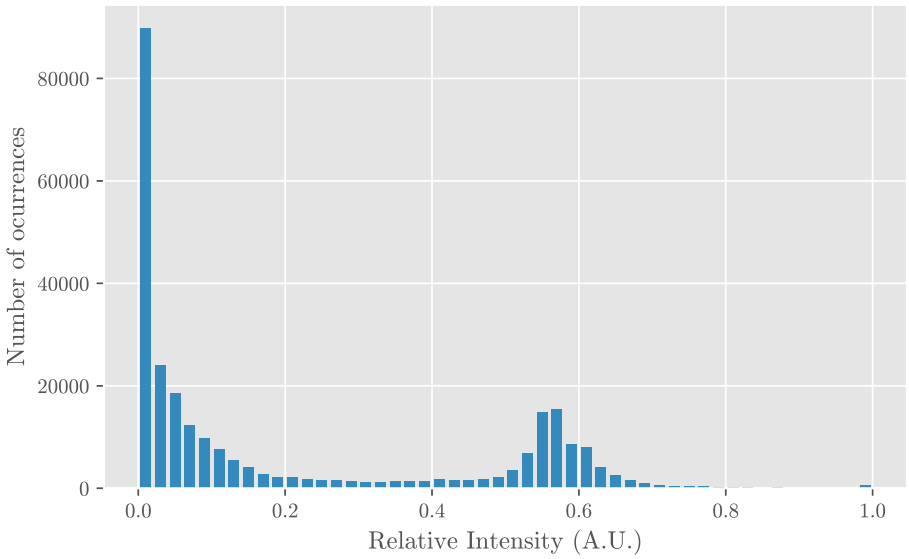

Figure 4.10: Histogram of luminous intensities in the whole testing image.

The use of the dichroic creates an additional object in the laser's path. The amount of light reflected and absorbed should not be significant, as the dichroic was designed for minimizing these phenomena in the wavelenght range of the Axsun laser source. However, it changes the light's path and therefore requires position of the reference mirror to be properly adjusted.

At the same time, the replacement of the AL2520M by its anti-reflective counterpart caused notable losses in the intensity of the beam. Measuring the power output of the beam with the new lens shows signs of significant losses in the beam's optical power. Measurements show that with the original lens, around 7% of the power is lost each time the beam crosses the length. With the anti-reflective lens, this percentage rises to nearly 20%, causing a drop in optical power from 3 mW to 2.37 mW.

Neither of these issues prevents the OCT system from acquiring axial data from a sample. However, there has been a visible decrease in signal quality .

5 | Control Module

The working setup described in Chapter 3 had several issues, particularly related to how the galvanometers were controlled. The horizontal galvanometer required manual setup using a signal generator. This often meant the signal parameters required some manual fine-tuning to perform as expected.

The vertical galvanometer, on the other hand, was controlled by the software on the host computer, with complete independence from the horizontal movement. When acquiring a volume, the vertical galvanometer was made to move when the acquisition of a B-Scan was considered complete. This was made independently from the current status of the horizontal galvanometer. The only considered factor to know if a B-Scan was complete or not was the number of A-Scans acquired. This meant that every time all the required A-Scans were acquired, the vertical galvanometer moved, and it would be considered a new B-Scan. However, this could happen when the horizontal galvanometer was stopped, halfway through the scan, or at any other point, given that it was started at a random time and controlled by an automated and independent device. Due to this situation, the scanning motion of the horizontal galvanometer needed to be manually synchronized with the B-Scan acquisition, by adjusting the phase offset of the generated signal.

This need for human intervention at the hardware level creates friction in the acquisition process, making it harder and slower. Another issue was related to wasting time during acquisitions by using a sub-optimal scanning method. In Section 3.5 it was mentioned that the use of a non-symmetric sawtooth wave wasted 1 ms per B-Scan, increasing the scanning time for a typical B-Scan of 512 A-Scans by nearly 20%. This waste should be corrected in order to improve performance. Even though the capabilities of the previous setup were already quite reasonable, particularly when comparing to previous years when acquisitions were several times slower, it's still worth improving. Reducing acquisition times, particularly when dealing with large volumes, helps reducing artifacts due to movements.

To make the necessary improvements, a control module was developed to be integrated in the system, replacing some of the pre-existing components.

The development of the module was carried out by professor Custódio M. F. Loureiro, from the Department of Physics of the Faculty of Sciences and Technology of the University of Coimbra. The development of said module was not a part of the work carried out in this thesis. Its integration with the OCT system and the existing software, and consequent testing were however carried out as part of this work. As such, the emphasis will be on presenting the practical aspects of the module and troubleshooting, rather than on its hardware and inner programming. For this end, the module will be treated as a black box which accepts inputs from the host computer and the laser source, and provides the expected outputs to the DAQ and the Digital-Analog Converters (DACs) controlling the galvanometers.

Most of the information in this chapter was provided in the documentation which accompanied the module [55].

5.1 General description

The control module communicates with a host computer through an USB-SPI converter (Adafruit FT232H Breakout). A set of Python 2 scripts enables sending programming parameters that control its behavior. The FPGA receives the parameters through SPI from the converter, and then proceeds to start or stop the acquisition process according to the parameters. It does the job of synchronizing the signals sent to the DACs, which control the galvanometers, with the Trigger signal sent to the DAQ in the host computer, which originated from the Axsun laser source.

This way, the module is single-handedly responsible for controlling the galvanometers while at the same time also controlling the trigger signals which enable data acquisition. This allows the module to synchronize the acquisition with the galvanometer's movements, by only enabling acquisition at the desired times when the galvanometers are stopped at the desired positions.

The signals sent to the DACs that control the galvanometers are now controlled by the module. A signal which is better adjusted to the desired galvanometer's behavior can be generated, to avoid wasting time as it was done previously.

The overall impact of the module can then be summed up in a few items:

- The system now uses optimized waveforms to control the galvanometers;
- Control of the whole acquisition process can be done in a single central location, the host computer;

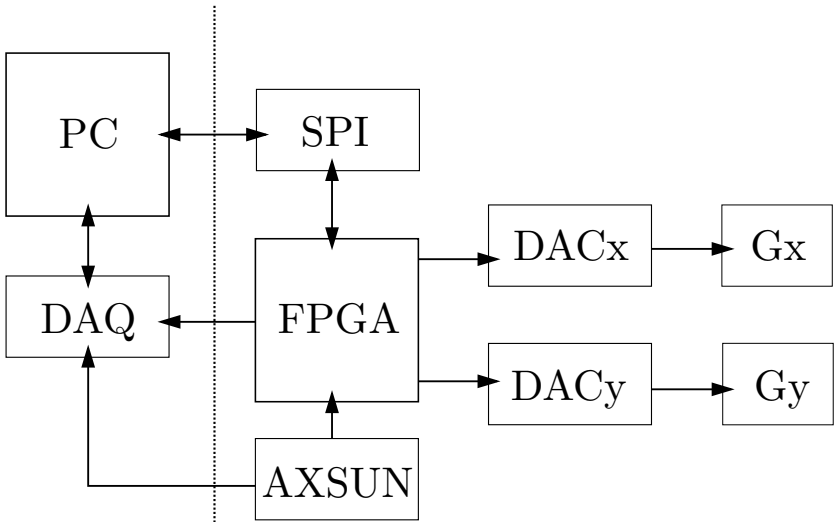

Figure 5.1: General architecture of the control module for data acquisition. Gx and Gy refer the horizontal and vertical galvo, respectively. Adapted from [55]

- Configuration and setup of the acquisition settings now requires less time-consuming human interaction.

5.2 Operation

Four operating modes are made available to control the galvanometers' movement:

- A-Scan;
- Horizontal B-Scan;
- Vertical B-Scan;
- Volume Scan.

In addition, another instruction exists to make the module terminate any currently ongoing operating mode, namely the Stop instruction. A new mode cannot be started while another is operating. In order to update operation parameters or start a different mode, the module needs to be sent the Stop signal prior to the new instructions.

The operating modes are associated with the scans described in Section 2.5. In each of them, the module outputs at its DACs the corresponding voltages needed to move the galvanometers as intended.

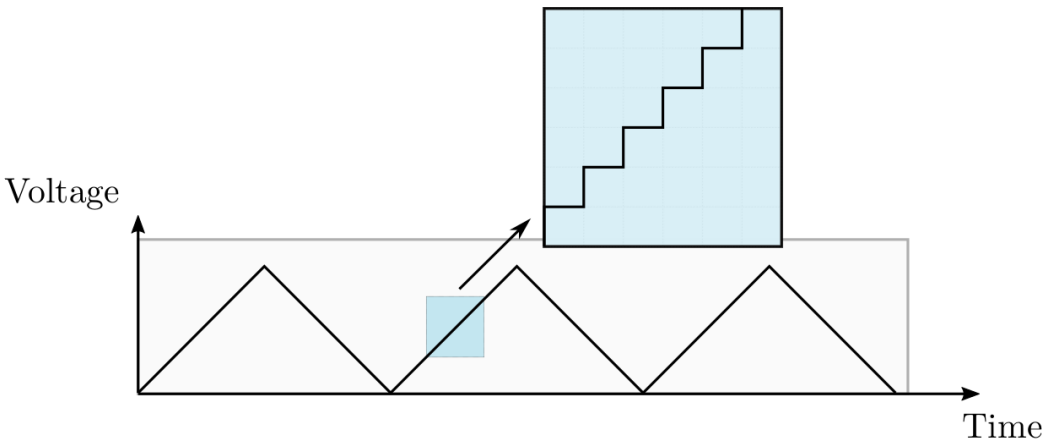

Figure 5.2: Representation of the scanning waveforms generated by the control module to perform B-Scans. The ascending edges make the galvanometer scan in one direction and the descending edges make it scan backwards.

For an A-Scan, as it is an axial scan, the galvanometers should stay still at the desired positions. The voltage that is input to them is a constant value, which varies with the desired scan location and voltage-to-degrees conversion scale. In this mode, the galvanometers and triggers continue indefinitely until the module receives the Stop signal.

For the B-Scans, one of the galvanometers remains still while the other scans the sample in a given range. The galvanometer that remains still is subject to the same voltage as it would be during an A-Scan. The other is controlled through a symmetric quasi-triangular waveform, as shown in Figure **??**. The wave is not really triangular, as it is composed of small steps, with a number of small plateaus equal to the desired number of A-Scans. It is in these plateaus that the acquisition of individual A-Scans takes place. As the wave is symmetric, when the end of a B-Scan is reached, the galvanometer starts scanning at the same rate in the opposite direction. This eliminates the time that was wasted while resetting the galvanometer to its starting position, as acquisition continues at a similar rate in the opposite direction. The modes for acquiring B-Scans also continue indefinitely until the module receives the Stop signal, similarly to the A-Scan mode.

Volume scans are simply a finite sequence of B-Scans. Unlike the other modes, this one requires that the total number of B-Scans be defined, and it stops after that number of lines were scanned. The result composes a three-dimensional volume of data with a fixed number of A-Scans and B-Scans. The waveform that controls the horizontal galvanometer is similar to the triangular one generated for acquiring B-Scans. For controlling the vertical

galvanometer, the signal is an ascending ramp made of small steps. This is similar to the ascending phase of the signal generated for acquiring B-Scans, but each plateau is long enough to allow the acquisition of an entire B-Scan. Also, when the vertical scan is over, the acquisition is considered finished and the module goes back to awaiting instructions.

5.3 Usage

A set of Python 2 scripts were provided together with the control module. These allow to start and stop the galvanometers movement, in a variety of different predefined modes. The scripts communicate through USB with the Adafruit FT232H Breakout board, which then passes on the information to the FPGA through SPI.

In order to use the scripts, several requirements have to be met in the host computer:

- Python 2.7 is required;
- The driver `libusb`;
- The library `libftdi`.

With the requirements met, the module can be connected through USB and controlled through the host computer. Each of the four operating modes described in Section 5.2 can be started by running the appropriate script with the required parameters, as described in Table 5.1.

A total of 10 different parameters can be found in Table 5.1. There are essentially two types of parameters: spatial and temporal.

Spatial parameters are related to the position of each galvanometer and affect the output voltage of the control module, which is used as input voltage for the galvanometers' positions. They include the parameters for `position`, `start`, `increment` and `numberofpoints`.

- `x_position` and `y_position` are meant to define the position at which the given galvanometer is to be kept. They are only available in modes where at least one of the galvanometers keeps steady at the same position, to perform a consecutive B-Scans or A-Scans.
- `x_start` and `y_start` define the starting point for the scanning of the given galvanometer, defined by the starting voltage for the scan.

Mode	Arguments
A-Scan	x_position y_position galvanometer_setup_time daq_valid_time
Horizontal B-Scan	y_position x_start x_increment x_numberofpoints galvanometer_setup_time daq_valid_time
Vertical B-Scan	x_position y_start y_increment y_numberofpoints galvanometer_setup_time daq_valid_time
Volume Scan	x_start x_increment x_numberofpoints y_start y_increment y_numberofpoints galvanometer_setup_time daq_valid_time

Table 5.1: Parameters needed to start each mode of operation in the control module

- `x_increment` and `y_increment` control the voltage step between each resting position for the given galvanometer. This can be either the steps between consecutive A-Scans, or consecutive B-Scans, in the case of `y_increment` in the Volume Scan.
- `x_numberofpoints` and `y_numberofpoints` control the total number of resting positions during the scan. This can be the total number of A-Scans in a B-Scan, or the total number of B-Scans in a Volume.

The values to be passed to the scripts in any of these cases are signed integers. The values which correspond to the limits in the target area are shown in Figure 5.3. For the horizontal galvanometer, these values are -32768 for the left side and 32767 for the right. For the vertical galvanometer, these values are 32767 for the upper limit and -32768 for the bottom limit. The maximum and minimum voltages at the output of the module's DACs are given by:

$$V_{Max} = V_{REF} \times \frac{32767}{32768} V_{Min} = -V_{REF} \tag{42}$$

With $V_{REF} = +2.5\ V$. The limits for the parameters are obtained from these limits. For the `position` parameters, the value has to be within the given module limits mentioned above, meaning that $-32768 \leq P_{position} \leq 32767$.

For the other three parameters, which are always used in conjunction, it's different. The three parameters need to follow two conditions to be valid: firstly, the `start` parameter always needs to be within the module

limits, $-32768 \leq P_{start} \leq 32767$; secondly, the value of the last point in the scan also has to be within the limits, $-32768 \leq P_{start} + P_{increment} \times P_{numberofpoints} \leq 32767$.

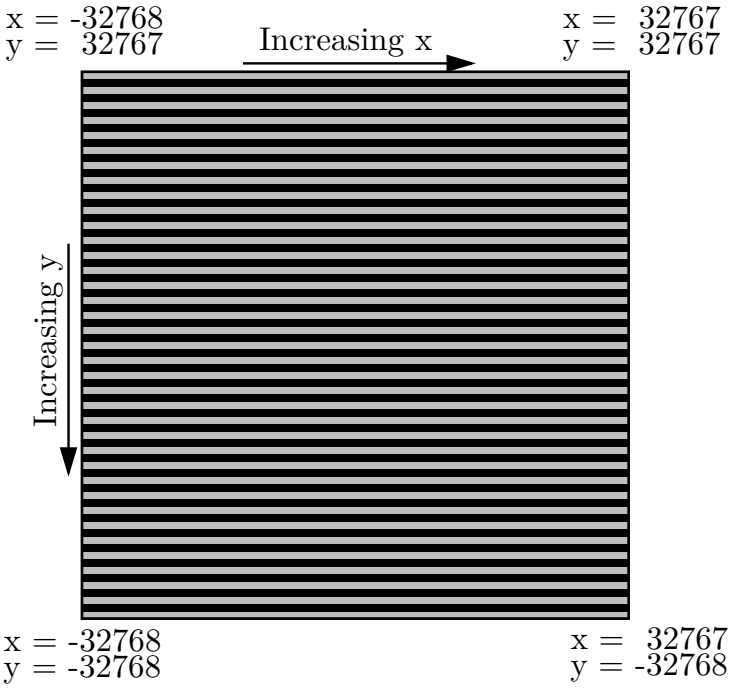

Figure 5.3: Representation of the value passed to the module and the corresponding location in the target area. The arrows indicate the initial direction (for the horizontal galvanometer x) and the direction taken when acquiring a volume (for the vertical galvonometer y).

The minimum differential voltage value which can be changed is associated with a change of one in the module's parameters. It corresponds to an increment of 1 LSB in the DAC ouput voltage, which is a value around $VREF/32768 \approx 76\ \mu V$. Depending on the voltage-to-degree scale chosen, this voltage difference can mean a correspondent angle shift between 0.000076° and 0.000152°. In Table 3.4 it can be seen that the resolution of the galvanometer scanning system is in fact 0.0008°, several times larger than the minimum value the module is able to provide. Thus it can be concluded that the minimum steps the module can provide are more than enough to control the galvanometers with maximum precision.

Temporal parameters are related to the durations of some actions, and affect the overall timeline of the acquisition. These include the other two parameters, `galvanometer_setup_time` and `daq_valid_time`, as well as two more which were posteriorly added, as will be explained in Section 6.1.2. All

these parameters are passed as a positive integer, in units of 20 ns.

- `galvanometer_setup_time` defines the time between the signal to send the galvanometers to their starting position and the signal to start acquisition. This allows the creation of a time margin to account for the positioning time of the galvanometers, so that acquisition does not start when they are still positioning.
- `daq_valid_time` states the elapsed time, after the signal from Axsun source, until the acquisition of data by the DAQ ends. The DACs from the control module are programmed automatically after this interval, to maximize preparation time of the galvanometers between successive acquisitions.

While the module is turned on, a set of LED indicators provide feedback on the current status of the module. Their meaning is described in Table 5.2.

LED	Meaning
LED 1	Glows while the FPGA is counting time, during the initial programming of the DAQs and during acquisition.
LED 2	Glows while the 50 MHz clock on the FPGA is valid. Module is operational if it is off.
LED 3	Glows while a Volume Scan is ongoing.
LED 4	Glows while a B-Scan is ongoing.
LED 5	Glows while a A-Scan is ongoing.

Table 5.2: LED feedback on the module's FPGA board

5.4 Improvements

Substituting the previous galvanometer control process by the newly developed control module provides two types of benefits: optimization and usability.

The acquisition process benefits from optimizations due to the control module. As it has already been mentioned, the scanning process was not taking full advantage of its potential for high-speed performance. The new control module improves on this issue. Scanning is done in two directions, discarding the possibility of dead times due to resetting the position of the galvanometers to start another scan. Both galvanometers are now controlled

from the same source, which also coordinates them with the triggers from the Axsun laser source. Currently, the speed of acquisition is mostly limited by hardware limitations. These limitations can be either the galvanometers' maximum speed or the fixed sweeping frequency of the laser source, depending on the parameters of acquisition. There is still an issue that causes sub-optimal acquisition times, but the difference is now constant for any acquisition, and in the order of milliseconds, as described in Section 6.1.2.

Usability wise, the fact that the module controls both galvanometers allows for a smoother experience for the user when setting up the acquisition parameters. Before this required fiddling with several settings, and possibly fine-tuning some parameters each time the galvanometers were started. This has been greatly simplified. The Python 2 scripts provided allow simply dictating parameters to the module, and it performs as expected. This aspect was further improved by integrating the control of the module within the OCT software.

6 | Software Integration

The addition of the camera module and the replacement of the of galvanometer control system require that the software on the host PC be adapted to seamlessly work with the new setup. The most urgent changes are:

- Adapt the reconstruction of B-Scans and Volumes to fit the new acquisition model;
- Add the capability to control the galvanometers behaviour directly from the software, with corrections related to the old behaviour;
- Create a new visualization window inside the software that relays images from the camera in real time.

The first item is fundamental to keep the OCT system working. Without correcting the process of acquisition and reconstruction for the new behaviour, it would not be possible to keep viewing A-Scans and B-Scans in live mode, and Volume acquisitions would require further preparation before being ready for any kind of usage. This is not a reasonable behavior, and thus needed correcting. In addition, some undesired behaviour was discovered, and had to be compensated through software.

The second item is not fundamental to test the working of the system, as galvanometers can be controlled from a command line. However, this is not practical, intuitive or user-friendly, as it requires additional effort and time, particularly for the calculation of the values to be passed to the control board. It would also be unpractical needing to use more than one interface to control the same system. As such, it is undesirable that the control is done in that way, and so the control was integrated in the existing software.

Lastly, there was a need to integrate the live-visualization that the camera offers into the software. Again, it could be done using an external program, but it makes no sense to use more than one software to control the system. In addition, this integration opens the way to new functionalities in the future, which may require the camera.

Besides these changes which were expected from the start, some issues and troubleshooting ended up requiring attention and further work so that the system can work without major problems.

Further changes that improve the overall functionality of the system and the user-friendliness of the process can also be implemented in the future. However, due to some constraining factors, mainly related to time, it was not possible to develop them during this work. They will however be discussed in Chapter 7.

6.1 Data acquisition and reconstruction

6.1.1 Direction tracking

The main reason for the initial changes in the acquisition and reconstruction of B-Scans is related to the change in the scanning behaviour of the horizontal galvanometer. Previously, the direction of scanning was constant, with the horizontal galvanometer scanning once in a direction and at the end returning as quickly as possible to the initial position, to start another scan. The new control model changed this behaviour, and the horizontal galvanometer currently scans in alternating directions. The signal output by the control module to the galvanometers input is shown in Figure **??**. Following this signal, it scans from the initial position through the desired range, during the ascending phase, until it finishes scanning the initial B-Scan, and after that it starts scanning at the same speed, but in reverse direction, during the signal descending phase. This removes the need to wait for the galvanometer to return to its initial position, allowing for seamless acquisition of sequential B-Scans.

This means that continuing building volumes or showing B-Scans in the same way as it was previously done would reverse each alternating B-Scan. For instance, two sequential B-Scans at the same vertical position would be equal. However, if the software was to be left unchanged, now the second B-Scan should appear to be a mirrored version of the first one. Such a behaviour is predictable and is consistently repeated, as it is expected by the way the galvanometers move. Consequently, it can be corrected by software, by tracking the direction of each individual B-Scan, and correcting its reconstruction depending on the direction it was scanned in.

It's worth noting that the correction is done differently for the two work modes currently available on the software, live mode and acquisition mode. This is required because of the way the data is copied to the computer.

Live mode exists to preview, aim and calibrate the system in real time.

It allows viewing the raw signal and FFT for the central A-Scan in a B-Scan, in addition to rendering of a B-Scan, in real time. It does not work continuously for every B-Scan, as it cannot compute all these previews fast enough. Instead, it copies a B-Scan to memory and works on computing the needed information to display in the software. Only when it finishes processing does it copy another B-Scan and repeats the process. Any B-Scan that arrives while the host PC is busy processing the relevant information is discarded. This workflow means that each B-Scan is individually copied to the host computer memory after its acquisition has ended, and subsequently processed, unless the computer is busy processing a previous B-Scan. In live mode, the focus is on generating information to view on real time, for immediate action. The greatest constraint which requires some data to be discarded is the processing time, which limits the B-Scan acquisition rate. As each processed B-Scan is dealt with individually, the direction of any B-Scan, even if they end up not being processed, needs to be tracked, in order to keep their state known.

Acquisition mode, on the other hand, is used to reliably generate a file with a given amount of quality data representative of the sample (an A-Scan, B-Scan or more likely a volume), for posterior study and analysis. In acquisition mode, the focus is instead on acquiring the needed data as quickly as possible, without losing or discarding anything along the way. For this end, any processing is only done once the acquisition is finished, to avoid delaying the acquisition process. The galvanometers always start from the stopped position and in the same direction, and the complete structure of the acquisition is always known (number of B-Scans, number of A-Scans per B-Scan, frame size). This means that in this case, tracking is not necessary, because the starting direction is known and the data is always continuous, as nothing is discarded.

For tracking the scanning direction in live mode two Boolean variables were implemented, `CurrentBScanReversed` and `ProcessedBScanReversed`. `CurrentBScanReversed` changes value whenever a B-Scan is copied from the DAQ board to the host computer's memory, keeping track of the current scanning direction. `ProcessedBScanReversed` has its value set when a B-Scan is about to be processed in live mode, and it is the variable which defines the acquisition direction of the B-Scan to be processed.

```
void  ApplicationIO::HandleDataAvailable(PacketStreamDataEvent & Event){

  CurrentBScanReversed = !CurrentBScanReversed; // Track state of BScan
   ↪  inversion
  Buffer Packet;
  Event.Sender->Recv(Packet); //Extract the packet form the Incoming Queue
```

```
bool ignoreDirection;
if(ReadyForNewPacket){
  IntegerDG Packet_DG(Packet);
  switch (Settings.ReversingMode) {
    case 1:
      ignoreDirection = !CurrentBScanReversed;
      break;
    case 2:
      ignoreDirection = CurrentBScanReversed;
      break;
    case 3:
      ignoreDirection = true;
      break;
    }


  if(!AcquisitionMode){ //  Live Mode
  if(!AcquisitionMode && ignoreDirection){ //  Live mode - Ignore
   ↪  reverse scans
    ProcessedBScanReversed = CurrentBScanReversed; // Save current Bscan
     ↪  state for processing
    ReadyForNewPacket = false;
    IppCopyInt32Buffer(&Packet_DG[0], &LiveData[0],
     ↪  Settings.AnalogInPacketSize/2);
    UI->DataProcessing();
    UI->BScanInc();
    TallyBlock(Packet_DG.SizeInBytes());
    }

  else if(AcquisitionMode){ //  Acquisition Mode

    //if (wait < 100 && !BackgroundAcquisition){
    //  wait++; //Wait for Y galvanometer to go to initial position
     ↪  (100*10us = 1ms)
    //  NumBScan = 0;
    //  }
    //else{
      if(NumBScan < Settings.BScans-2){ //  Copying B-Scans as they are
       ↪  acquired
        IppCopyInt32Buffer(&Packet_DG[0],
         ↪  &AcquisitionData[NumBScan*Settings.AnalogInPacketSize/2],
         ↪  Settings.AnalogInPacketSize/2); // /2 devido ao 2's
         ↪  complement
        UI->BScanInc();
        }

      else { //  Acquisition Finished
```

```
            IppCopyInt32Buffer(&Packet_DG[0],
             ↪  &AcquisitionData[NumBScan*Settings.AnalogInPacketSize/2],
             ↪  Settings.AnalogInPacketSize/2);
            Stream.Stop();
            UI->DataProcessing();
            }
        }
    }
}
```

`HandleDataAvailable` is called whenever data is ready to be transferred to the host computer's memory. In live mode, this is when a B-Scan is complete. In acquisition mode, it only happens after the whole sample has been scanned. Each time this function is called, the variable `CurrentBScanReversed` switches its value, which indicates whether the B-Scan has been acquired in reverse direction. Only after this is the current availability state checked. If the variable `ReadyForNewPacket` is false, nothing else is done. However, the current direction of the scanning was already declared by switching the value of `CurrentBScanReversed`. If `ReadyForNewPacket` is true, the acquisition continues. For acquisition mode this variable is true until all the data is collected.

In the user interface, there is a group of radio buttons which allow choosing what B-Scans can be shown to the user: either those acquired in the raising edge of the galvanometer control signal, those acquired in the declining edge of the galvanometer control signal or any B-Scan. This allowed testing the behaviour of the changes implemented here, but was left on due to usefulness related to other issues, which will be mentioned in the following sections. The variable `ignoreDirection` is responsible for implementing the desired behaviour, causing the B-Scan to be discarded when set to false.

When the software is not set for acquisition mode, it either ignores the B-Scan if it is on the undesired direction, or it copies it to a memory address in the host computer using `IppCopyInt32Buffer` and starts processing it immediately, by calling `UI->DataProcessing()`.

When set to acquisition mode, the rest of `HandleDataAvailable` responds exactly as it used to, by copying each B-Scan to memory and processing them all when the acquisition is complete. As the whole data is processed at once and the conditions for acquisition are always known, there is no need to track the state of each B-Scan.

While being processed, the data acquired was sequentially iterated, to divide the continuous data available at `&LiveData` and `&AcquisitionData` into B-Scans (for data acquired in acquisition mode), A-Scans and individual data points. Knowing this, one quick way to fix the issue of reversing the

images is by iterating it differently depending on the direction it was acquired. If one given B-Scan is known to have been acquired while scanning in reverse, this can be corrected by iterating the data read starting from the last A-Scan of that B-Scan until the first, while writing it where their correct positions would normally be.

```
while (iB < BScans){ //Iterate B-Scans if Acquisition Mode

  for (int iA = 0;  iA <  AScans; iA++) {  //Iterate A-Scans

    // If current Bscan is reversed, read AScans in reverse order
    if ((AcquisitionMode && (iB % 2 == 0))){
      iA_read = AScans - iA - 1;
    } else if(AcquisitionMode && (iB % 2 > 0)){
      iA_read = iA;
    } else if (!AcquisitionMode && ProcessedBScanReversed) {
      iA_read = AScans - iA - 1;
    } else {
      iA_read = iA;
    }

    iA_write=iA;
```

For this purpose, two additional auxiliary variables are defined to replace `iA` (the index of the currently processed A-Scan): `iA_read`, which provides the location of the A-Scan to be read from memory, and `iA_write`, which provides the location where the data is to be written. `iA_write` is alway equal to `iA`, and is only defined to for readability. `iA_read` changes depending on whether the B-Scan currently being processed needs to be reversed or not. For live mode, this is done resorting to the variables defined earlier. For acquisition mode, this is done by dividing the B-Scans in even and odd numbers. If the B-Scan has an odd number, it is reversed. Otherwise, it is not.

The process for reversing is simple: if the B-Scan is to be reversed, the order A-Scans are iterated starting on the last one of the B-Scan and ending on the first, by the lines above which state `iA_read = AScans - iA - 1`, where `AScans` is the total number of A-Scans.

It is worth mentioning that each time the galvanometers are stopped, the variables `CurrentBScanReversed` and `ProcessedBScanReversed` are reset to their default values, to ensure the same starting conditions each time the galvanometers start.

This solves the problem of correcting for the new behaviour of the control module, which sweeps the horizontal galvanometer alternately in both directions. The code shown above still does not reflect the final version. One

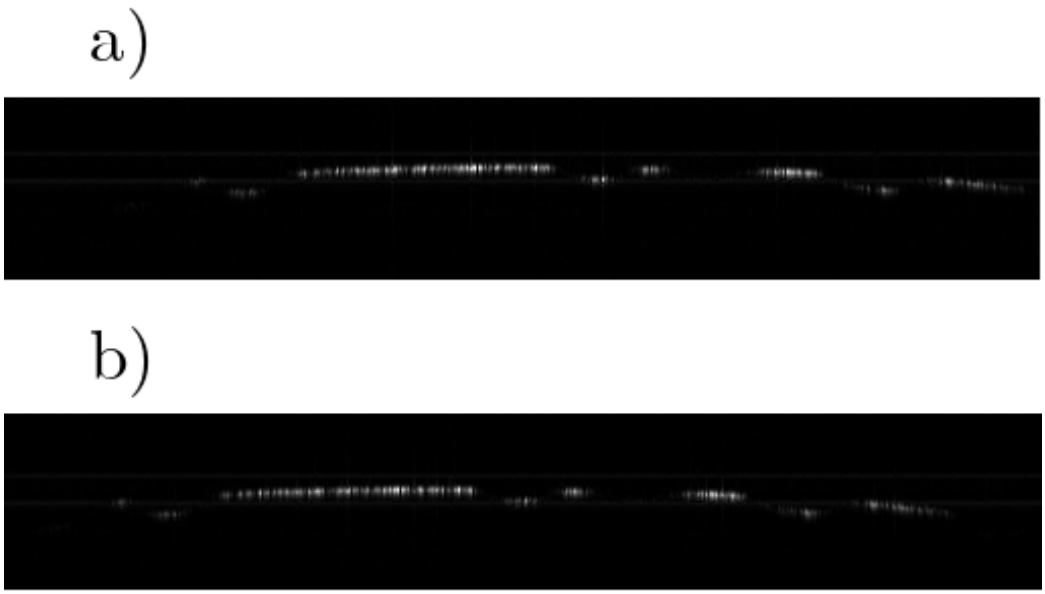

Figure 6.1: Part of two sequentially acquired B-Scans of a solid, opaque reflecting surface from a coin. The one from the top, a), was acquired first, and corresponds to an odd B-scan. The bottom image, b), corresponds to an even B-Scan, acquired while the galvanometer is scanning in backward toward its initial position. A clear lateral shift can be seen between the two.

more issue related to the control module had to be compensated through software, as explained in the next section.

6.1.2 Unmatched sequential B-Scans

The need to reverse B-Scans due to a different acquisition process was an expected consequence of implementing the new control module. It was only after the relevant corrections mentioned in the Section 6.1.1 were completed that some different, unexpected issues were detected.

When watching a sequence of B-Scans already corrected for the new acquisition method, it was possible to see that some of them appeared to be shifted. This is represented in Figure 6.1. It could be seen that the B-Scans were similar, but appeared to be shifted versions of each other. This was particularly clear when watching sequential B-Scans acquired at the same vertical location. In this case the B-Scan should be exactly equal. However, the distinctive characteristics of alternating B-Scans always appeared shifted.

In order to figure out the reproducibility of this issue, several acquisitions were made, varying different acquisition parameters, to see if any of them

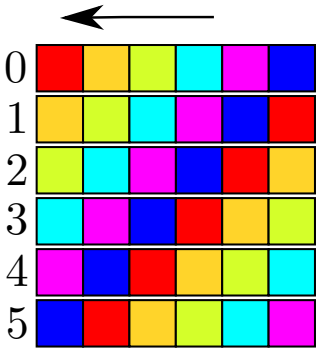

Figure 6.2: Demonstration of rotating a line of colored pixels. The arrow shows the direction of rotation, and the numbers indicate the rotation relative to the initial position.

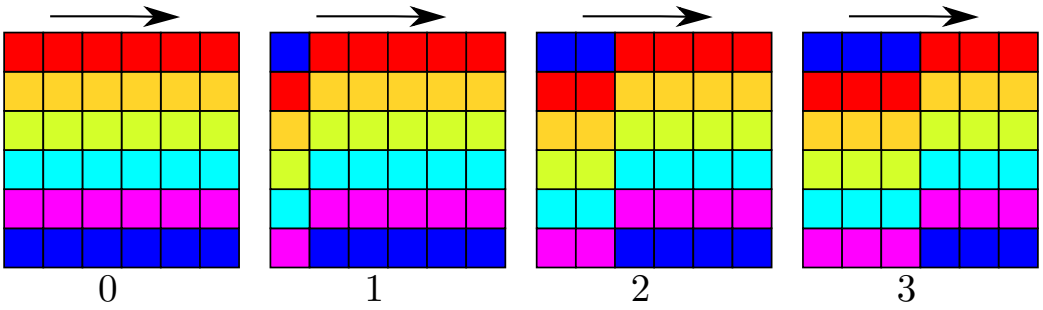

Figure 6.3: Demonstration of rotating a matrix of colored pixels. The arrow shows the direction of rotation, and the numbers indicate the rotation relative to the initial positions of the pixels.

produced any change in the results. To easily compare two B-Scans, a simple script was written in MATLAB to find out if they are shifted versions of each other, and the relative distance in pixels between them, where each pixel corresponds to an A-Scan.

For clarity, two B-Scans shall be considered, with the B-Scan acquired while scanning in the normal direction being referred to as B^N_{Scan} and the B-Scan acquired while scanning in reverse direction being referred to as B^R_{Scan}.

The script tests different rotations on the B^R_{Scan}, iterating through all possible values. Rotating in this context means moving each pixel to the side, creating a shifted version of a given array. This process is exemplified in Figure 6.2 for a line of pixels and on Figure 6.3 for a matrix of colored pixels, a closer analogy to an image. The arrow denotes the rotation direction. The values in one extremity are passed on to the other extremity when pushed beyond the limit of the array. For each rotated B-Scan, the total sum of the pixel-to-pixel difference between the rotated B^R_{Scan} and the original B^N_{Scan} is

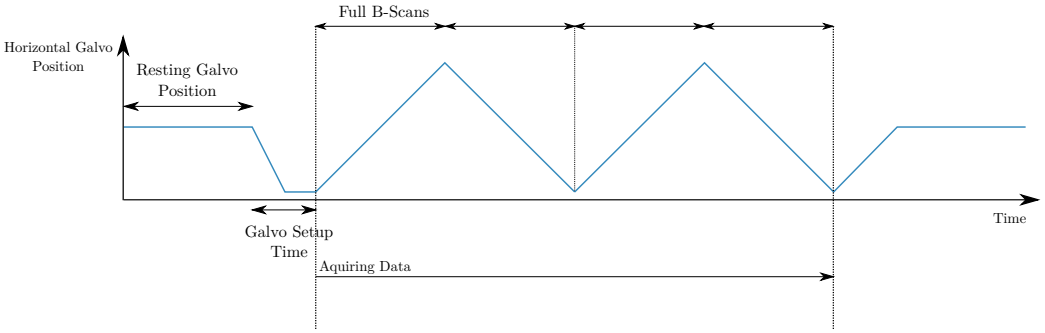

Figure 6.4: Expected behavior when acquiring consecutive B-Scans.

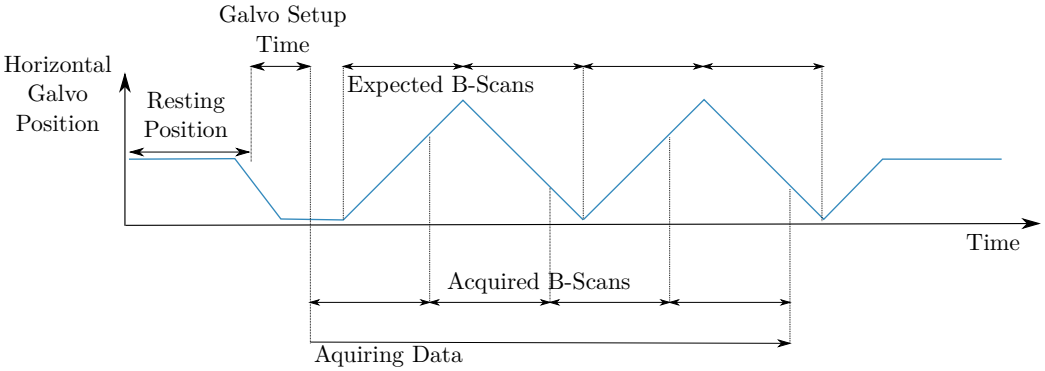

Figure 6.5: Observed behavior when acquiring consecutive B-Scans.

calculated. The rotation that produces the lowest difference is assumed to be the one that coincides with B^N_{Scan}, and the rotation value is the associated shift needed to superimpose the images.

This can be done with entire volumes instead of individual scans to reduce variations and the impact of spikes in individual pixels. B^N_{Scan} is replaced by all the odd B-Scans and B^R_{Scan} is replaced by all the even B-Scans. The volume made of the even B-Scans will obviously not be equal to the one with the odd B-Scans, unless the sample does not change in the vertical direction. However, the total sum of the difference in the pixels should still be lowest for the right rotation value. The sample is still the same, but as if it were sampled in interleaved lines, which should still maintain a good level of coherence. This only stands if the sample does not have high-frequency variations in the vertical direction.

Testing with these scripts for different conditions allowed reaching some conclusions related to the nature of the phenomenon. The shift was mostly constant independently of the scanning range, position, number of A-Scans, or the variables `galvanometer_setup_time` and `daq_valid_time`. When

acquiring B-Scans with a lower number of A-Scans, the variation was slightly larger, although the average value was the same. This was probably due to smaller B-Scans being more susceptible to small variations in the calculations. Also, it is worth noting that a small region on one of the sides of the image remained incoherent in alternating B-Scans, with a width equal to the shift distance, 40 pixels.

In addition, through some changes in the OCT software on the host computer it was possible to test if there were any data losses in the acquisition. Testing was done by seeing how the software would react by receiving one less A-Scan than it was expecting. Acquisition mode never finished in this test, showing that even if a single A-Scan were missing, acquisition mode would not work. This was shown to not be the case, and as such it meant the correct number of samples was being received, so the origin of the issue could not be this.

At this point, several facts were known:

- The shift was constant, independently of the values passed to the control board.
- The shift was equivalent to a significant amount of time, in the order of hundreds of microseconds.
- There was no loss of data.
- The rotation testing indicated that a 40 pixels rotation was needed to superimpose B-Scans acquired in alternating directions (as much as possible).
- The results of the correction by rotating all the even B-Scans still caused lack of coherence in one of the sides of the volume acquisition.

This issue was discussed with the developer of the control module to evaluate any possible causes that could be related to the control module. It was proposed that the problem could be due to the Galvanometers not having time to settle before inverting direction, or between A-Scans, with any delay being posteriorly compensated.

Thus, it was concluded that adding two new time-related parameters to control the signal could potentially solve the issue. If the cause of the problem was not the one that was discussed, it would at least help isolate it and identify it. They would allow setting a time between each A-Scan or each B-Scan for the galvanometers to stabilize. These parameters were:

- `point_hold_time`: this parameter defines the time that the galvanometer holds still in a stable position for the acquisition of an A-Scans. This is the time between the programming of the DACs which control the galvanometer, and effective start of the acquisition.

- `extremity_hold_time`: it works similarly to `point_hold_time`, but only at the end of each B-Scan, as opposed to before of each A-Scan.

Both parameters should be passed as integer values, where each unit corresponds to 20 ns, similarly to the time parameters that were already available.

These parameters can still be bypassed by setting them to 0, thus allowing for the galvanometers to behave as they did before these changes. Also, they only impact the data acquisition rate if they force the system to skip one or more cycles from the laser source.

Experimenting with these values it was possible to see that the issue at hand actually responded to changes in the `point_hold_time`, but was independent of the `extremity_hold_time`. Increasing values passed to `point_hold_time` led to a reduction on the observed shift between consecutive B-Scans, with a value corresponding to 280 μs completely removing the issue.

On one hand, this solved the issue, and provided further insight into the situation. However, this meant that each A-Scan would take 280 μs, an impractically long time. A volume acquisition with 128 B-Scans, with 512 A-Scans each would take approximately 18 seconds, whereas it theoretically could have taken around 0.655 s, if this issue didn't exist. So, a better solution would have to be found.

The `point_hold_time` influenced the issue, and the shift in the data seemed to be as if the acquisition started at the wrong time. A problem at the start of the acquisition would create a deviation which would remain constant for the rest of the acquisition.

Testing out this hypothesis was done in MATLAB. The conclusion reached was that ignoring the first twenty A-Scans, and reshaping it so that it started at the twenty-first A-Scan and ignored the last B-Scan (which would be incomplete) fixed the issue. This method allowed correcting the issue by simply acquiring an extra B-Scan. The previous example of 128 B-Scans with 512 A-Scans each then takes around 0.660 s, very close to the theoretical limit imposed by the light source. It assumes that the error is constant, but everything done so far indicates that to be the case.

The problem itself may be related to the galvanometers. It's possible, although not mentioned in the specifications, that the galvanometer does

not start moving instantly. When moving in small steps around 0.2°, the specified time needed is 300 μs. A value close to that may be needed for the galvanometers to go from standing still to start moving at the desired continuous sweep speed (which in reality is composed of smaller steps, typically smaller than 0.01°). The impact of the `point_hold_time` could be that the galvanometers actually approach the stationary regime, where they stop long enough during each measurement for the small step to happen.

It's worth noting that this issue might not be new to the OCT system. However, the reason it wasn't detected sooner may be related to the way the galvanometers used to be controlled. They were controlled by a manually configured signal generator, and it's possible that this effect could be overridden by the phase offset. It is also possible it simply wasn't visibly impacting acquisitions, as they did not rely on quickly alternating the horizontal galvanometer's scanning direction, which is how this issue was detected now.

Solving this in software avoids the great increase in acquisition time due to the usage of the `point_hold_time` parameter. A new variable was introduced to perform the needed correction in the acquisition process, `AScansOffset`. This variable is set on the user interface and controls the number of A-Scans to be discarded at the start of the acquisition, to compensate for the behaviour described above. In addition, one extra B-Scan is acquired in addition to the desired amount, to compensate for the missing values. However, only the first values of the last B-Scan are used.

These changes were implemented in `ProcessingData.h` as an addition to the ones mentioned in Section 6.1.1.

```
int igAS = AScansOffset; // Number of A-Scans to be ignored in the
 ↪  beggining of the acquisition.
int ignoreLastBscan = 0;

if (AcquisitionMode) ignoreLastBscan = 1;

while (iB < BScans - ignoreLastBscan){ //Iterate B-Scans if
 ↪  Acquisition Mode

  for (int iA = 0;  iA <  AScans; iA++) {  //Iterate A-Scans

    // If current Bscan is reversed, read AScans in reverse order
    // If in AcquisitionMode, ignore initial A-Scans defined by
    // igAS and also ignore the last B-Scan
    if ((AcquisitionMode && (iB % 2 == 0))){
      iA_read = AScans - iA - 1 + igAS;
    } else if(AcquisitionMode && (iB % 2 > 0)){
      iA_read = iA + igAS;
    } else if (!AcquisitionMode && ProcessedBScanReversed) {
```

```
    iA_read = AScans - iA - 1;
  } else {
    iA_read = iA;
  }

  iA_write=iA;
```

The problem was only fixed this way for the acquisition mode. The implemented method would require additional changes to work with live mode. In acquisition mode, as all the B-Scans are processed at once, all the data is accessible. In live mode, processing is done after acquiring each B-Scan, and it is only possible to access that one B-Scan. Thus, it is not possible to access the next B-Scan in order to complete the current one, as done for acquisition mode. However, that is not a problem. In live mode, as only one B-Scan is visualized at a time, the consequences of the mentioned effect are not so drastic. In addition, as mentioned in Section 6.1.1, it is possible to choose whether to only watch the B-Scans acquired with the galvanometers scanning in a given direction, thus assuring coherence among consecutively shown B-Scans.

6.2 Galvanometer control

The new control module was provided together with a set of Python 2 scripts to control the galvanometers. As mentioned at the beginning of this chapter, it is not ideal to have the user using a command line to control the galvanometers, nor having to calculate the values to pass beforehand. An obviously better solution is to integrate the control in the existing software already available in the host computer.

Some choices must be made relative to the implementation of this feature. The first one is to choose how the communication between the software and the module will be done. The second is to decide how values are to be represented in the user interface and controlled by the user. The third is related to the implementation of commands and the current workflow of the software.

Firstly, the decision about communicating with the module's hardware. In addition to the already existing Python 2 scripts, it should be possible to implement the same behaviour natively in C++, which would fit well with the code. Several libraries compatible with Multi-Protocol Synchronous Serial Engine (MPSSE) are mentioned in the Adafruit FT232H documentation, to be used with C, C++ or Python. This would likely be the best option when it comes to performance, as everything in the software would run natively

in C++. However, it would take some time to implement, and it is more complex than the alternatives.

Another option is to call a command line to execute the existing Python scripts. This is inelegant and likely the slowest method. It may also raise security issues, as the Python scripts could be changed at any time to run arbitrary code. However, it is relatively simple and quick to implement, requires no additional software or libraries (not more than what is already required by running the scripts), and should be compatible independently of any external factors.

A third option would be to embed Python within the software and run the control code from there. This would be faster than calling a command line, even if it was for calling the scripts as mentioned above. It would also be simpler, and clearer than translating everything to C++, if the code were to be included completely in the software. However, this requires compatibility among the components. For instance, if the OCT software is compiled for a 64-bit machine, a 64-bit version of Python and the libraries would be required. Although the scripts written in Python are architecture independent, both the libraries and Python itself is not. In the documentation provided with the control module, a specific version of libftdi was suggested, and it was a 32-bit binary version. The OCT software is built for 64-bit systems, and thus requires compatible libraries, which were not provided. It should be possible to find the source code and build it from source to meet the current requirements, or to find a different version compiled for 64-bit. In the provider indicated in the documentation, the only existing options were compiled binaries, either 32-bit for Python 2 or 64-bit for Python 3. However, in the end, the choice was made to call the scripts from a command line, at least for the time being. This was due to the simplicity of implementation, easiness of switching for different scripts if necessary, and time constraints. Considering that the scripts code ended up needing to be updated to match the changes mentioned in Section 6.1.2, choosing to call the external scripts instead of programming the control within the software was likely the right choice. Regardless, it works well, allows for the desired features and may be changed in the future for a better solution, if needed.

Having decided on how to implement the communication with the module, the next step is to decide how values should be selected by the user. Requiring the user to input the exact parameters is unnecessarily complicated. It would be easier to have the user input some value related to the actual position or working of the galvanometers, such as voltage or the angle, for controlling their positions and scanning ranges. Similarly, the time parameters should be set in the interface in either nanoseconds or microseconds, as working in units of 20 ns can be confusing. The `numberofpoints`

parameter, on the other hand, should be interfaced to the already existing variables for A-Scans and B-Scans.

The interface has consequently been altered to accept several values which allow controlling the galvanometers. Some of these values were already available due to already being needed previously.

In order to allow the user to input the necessary data, several textboxes were created, allowing to input numeric values. These are then read and used to calculate the parameter values to be passed as arguments. The number of A-Scans and B-Scans were already present. In addition, the maximum and minimum voltage values for the vertical galvanometer were also present, as this galvanometer used to be controlled through the software, as explained in Chapter 3. To keep it similar, two textboxes were added to control the minimum and maximum positions of the horizontal galvanometer, like the existing ones for the vertical galvanometer. All of these were changed to accept input as an angle, in degrees, instead of a voltage, with two other textboxes allowing to select the voltage-to-degree ratio currently used on the galvanometers. The maximum angle is dependent on the selected scale, as it is limited by the maximum voltage output of the control module's DACs.

This comes to a total of six textboxes which select the parameters related to the scanning ranges: Galvanometer Y Min, Galvanometer Y Max, Galvanometer X Min, Galvanometer X Max, Y Scale and X Scale. It's worth noting that some of the textboxes change label, availability and purpose according to the selected operation mode. The only mode in which they are all enabled is Volume Scan. Otherwise, if one of the galvanometers is kept still, the maximum value for that galvanometer is disabled and the textbox to select the minimum value changes to Galvanometer X Position, in the case of the horizontal galvanometer, or Galvanometer Y Position, in the case of the vertical galvanometer.

The time-related variables to be passed as arguments also need to be selected, even though they should mostly stay the same. These are:

- `galvanometer_setup_time`;
- `daq_valid_time`;
- `point_hold_time`;
- `extremity_hold_time`

All of these values can be inputted in textboxes near the textboxes for A-Scans and B-Scans. They should be inputted in microseconds. The A-Scan offset mentioned in Section 6.1.2 is also controlled by the user, on its own textbox.

As the values to be passed are not inputted directly, they need to be calculated by the software. This is achieved through the expressions in Table 6.1. The expressions for the time related values are not included, as for each of them it is simply a matter of multiplying the values from the textboxes by 50.

Argument	Formula
x_position	$-32768 + 65535 \times (2.5 + X_{Min} \times X_{Scale})/5$
x_start	$-32768 + 65535 \times (2.5 + X_{Min} \times X_{Scale})/5$
x_increment	$65535 \times ((X_{Max} - X_{Min}) \times X_{Scale})/(5 \times N_x)$
x_numberofpoints	N_x
y_position	$-32768 + 65535 \times (2.5 + Y_{Min} \times Y_{Scale})/5$
y_start	$-32768 + 65535 \times (2.5 + Y_{Min} \times Y_{Scale})/5$
y_increment	$65535 \times ((Y_{Max} - Y_{Min}) \times Y_{Scale})/(5 \times N_y)$
y_numberofpoints	N_y

Table 6.1: How arguments passed to the control module are calculated. X_{Min} is the value from Galvanometer X Minimum. X_{Max} is form Galvanometer X Maximum. X_{Scale} is from X Scale. Y_{Min}, Y_{Max} and Y_{Scale} are the same but for Galvanometer Y. N refers to the number of points to acquire, either B-Scans or A-Scans, depending on the mode.

Lastly, there is also the need to implement some way to actually start and stop the movement of the galvanometers. There are some conditions on the current workflow that limit the possibilities of implementing this behaviour without rewriting fairly large parts of the software. This is mainly due to the way live mode works. It is not possible at this time to stop and start again the galvanometers and continue obtaining coherent images without firstly stopping the data streaming, closing every visualization and deleting all the data from before the galvanometers were stopped.

Currently, the start and stop behaviour has been implemented in the interface in such a way that it does not interfere with the rest of the software, and as such there was no need to rewrite anything other than the control components themselves. However, it's not possible to quickly change the scanning parameters in live view as would be desirable.

One button was created for issuing the order to start moving the galvanometers. The button is called `Start Galvos`, and it calls a function that builds a string based on the acquisition parameters, and uses it as an argument for `CreateProcess`. This way, a new thread opens to run the constructed string, which calls the installed python executable for running the

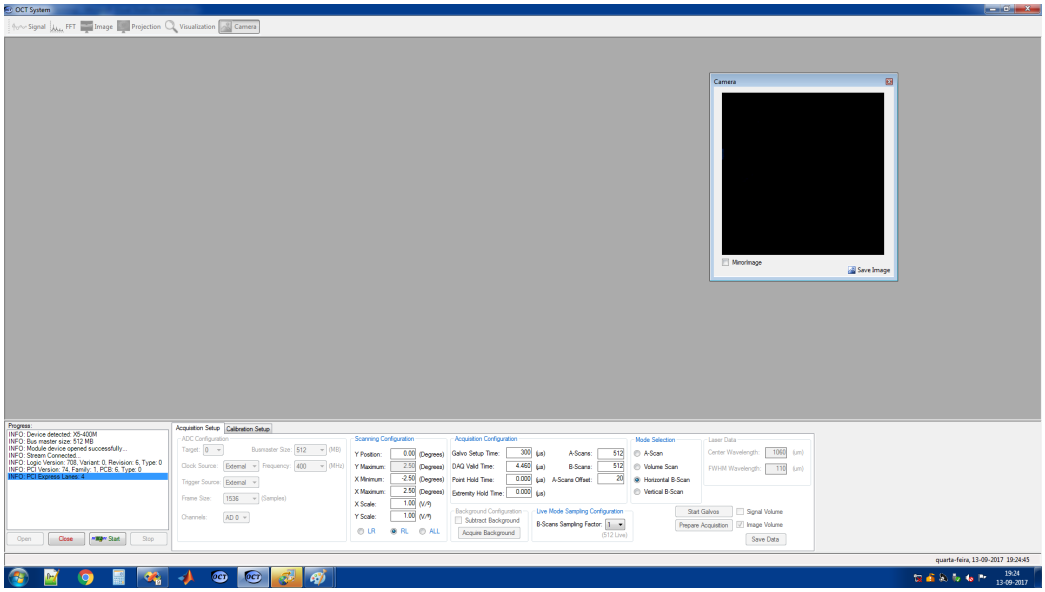

Figure 6.6: Interface of the OCT software.

chosen script with the relevant arguments.

There is no specific button for stopping the galvanometers. They are stopped whenever that behaviour is required by another action. They are stopped when live mode stops. They are also stopped when the button `Prepare Acquisition` is clicked, to allow setting up the parameters for the acquisition. In essence, the galvanometers are stopped whenever acquisition is stopped, or if they needed to change any parameters about their scanning.

The current behaviour for the galvanometers is as follows: after clicking `Open` to open the connection to the acquisition board and clicking `Start`, the data stream is started. No A-Scans arrive yet, as no triggers are reaching the board, as they only reach the board while the control module is active. At this point, the scanning and acquisition parameters can be changed. The button `Start galvanometers` is then after the parameters are set, in order to start the galvanometers. With this, the galvanometers start moving and the acquisition of A-Scans starts. From here, the possibilities are two: either the stream is stopped by clicking `Stop`, thus allowing to change the parameters for the live mode, or the button `Prepare acquisition` is clicked, to prepare the software for acquiring a given amount of data (A-Scan, B-Scan or Volume Scan) into a file, for storage and future usage. This allows changing some parameters before the acquisition. In this case, after the acquisition is finished, the stream of data stops automatically, and the file can then be saved.

This way, all the module's parameters can be controlled from the software. Although the user interface is not yet ideal, it is certainly and improvement. Figure 6.6 shows the current state of the software's user interface, with the changes relating to control a live preview already present.

6.3 Live preview

The main purpose of setting up the module described in Chapter 4 was to be able to observe the OCT's target area in real time. This means that its visualization should be set up within the system's software in the host computer.

The requirements of this integration are fairly simple. There should be a visualization mode allowing access to a real-time feed from the webcam mounted on the OCT, and it should be possible to save a frame from the live feed at any given time. In addition, the capability to reverse the feed horizontally was implemented, so that the user can choose to have it act as a mirror or as a front view of the target.

Several possible solutions exist for this purpose. However, the choice fell upon Open Source Computer Vision Library (OpenCV). This is a modern, actively developed library, widely used in scientific and commercial applications. It was chosen mainly for two reasons:

- Its relative simplicity, as it implements many commonly required features, such as accessing webcams, without requiring an unnecessary amount of code, allowing for software to be more maintainable and readable;
- Its versatility and overall capabilities, as it opens doors to what can be done with the software in the future.

The preview is done in a picturebox, `cameraPictureBox`, inside its own form window. The code for this runs on a separate thread, which remains active while `CameraAlive` remains true.

```
public: void RefreshCamera(){

      VideoCapture cameraCapture;
      cameraCapture.open(0);

      if (!cameraCapture.isOpened())
        {
        //cout << "Unable to open the camera\n" << endl;
```

```
    MessageBox::Show("Failed to open capture.");
    exit(-1);
    }
  Mat webcamImage;
  Mat flippedImage;
  Mat webcamImageCropped;
  cv::Rect cropArea(200,70,300,300);
  while (*CameraAlive) {
    cameraCapture.read(webcamImage);
    webcamImageCropped = webcamImage(cropArea);
    if (checkBoxMirror->Checked==false) {
      cv::flip(webcamImageCropped, flippedImage, 1);

    } else {
      flippedImage=webcamImageCropped;
    }
    //imwrite("cap.jpg",webcamImage);
    //}
    System::Drawing::Graphics^ graph =
     ↪  cameraPictureBox->CreateGraphics();
    System::IntPtr ptr(flippedImage.ptr());
    System::Drawing::Bitmap^ b = gcnew
     ↪  System::Drawing::Bitmap(flippedImage.cols,
     ↪  flippedImage.rows, flippedImage.step,
     ↪  System::Drawing::Imaging::PixelFormat::Format24bppRgb,
     ↪  ptr);
    System::Drawing::RectangleF rect(0, 0,
     ↪  cameraPictureBox->Width, cameraPictureBox->Height);
    cameraPictureBox->Image = b;
    //graph->DrawImage(b, rect);
    System::Threading::Thread::Sleep( 10 );
    }
  }
```

The software assumes there is only one webcam connected to the host computer, and connects to it through `cameraCapture.open(0)`, where zero is the number which identifies the camera. Currently it is always zero, as only one camera is connected. This can later be changed if the need arises, by adding some way to select from existing cameras and passing their number as an argument. Right now this behaviour is adequate, as no other cameras exist.

`cv::Rect cropArea(200,70,300,300)` is used to select the area where to crop the frames acquired from the camera. The captured frames have a size of 640×480 pixels, as it is highest maximum resolution the camera allows. A large part of this image is of no interest, as only a smaller area in the center of approximately 300×300 pixels contains the relevant target. Therefore,

cropping the images allows saving space in the user interface, which would otherwise be wasted.

The process for repeatedly drawing the image in the picturebox is contained inside a while loop. The image is read from the camera to the variable `webcamImage` by calling `cameraCapture.read`. The image is then cropped according to the area previously defined.

An if clause checks if the image is to be mirrored and proceeds to do it if necessary through `cv::flip(webcamImageCropped, flippedImage,1)`. This is used to copy the image from `webcamImageCropped` to `flippedImage`, applying the relevant transformation, where the last argument defines the flipping direction. In this case, the last argument defines the flip to be horizontal, and `flippedImage` is a horizontally mirrored version of `webcamImageCropped`. If the image is not to be mirrored, the `flippedImage` is equal to `webcamImageCropped`.

OpenCV keeps images in a Mat format, which is not immediately compatible with the forms in the software. Therefore, the image needs to be converted to a compatible format, such as to a Bitmap, before it can be displayed. This is achieved with `System::Drawing::Bitmap`. This constructor initializes a new Bitmap. The arguments passed define the width, height, stride, pixel format, and pixel data. The width and height are defined by the number of rows and columns in the image; stride is the byte offset between two consecutive lines, typically equal to the number of bytes in the pixel format multiplied by the width of the Bitmap; the pixel format defines the format to be used for the new Bitmap; and the pixel data is a pointer to an array of bytes containing the data of the image. The first three arguments are provided by the Mat class, the last one is created with `System::IntPtr`, and the format is chosen to be `Format24bppRgb`, where each pixel is composed of 24 bits, 8 for red, green and blue, respectively.

After conversion, the image is then drawn in the pictureBox and the thread is told to sleep for a given amount of time in milliseconds, 10 ms in this case.

This process does not affect significantly the acquisition process. In fact, the software allows to keep track of the data acquisition speed in live mode. It can be seen that the other forms of getting live information, such as windows for watching live B-Scans or the acquired signal, affect significantly the acquisition speed, reducing it by more than half. The impact of live previewing through the camera, even including the cropping and conversion between formats, has such a negligible impact that it can remain active during Acquisition Mode without impacting the quality or speed of data acquisition.

The window for watching the live preview of the target can be opened by clicking on the correspondent toolstrip button. Unlike the other preview

windows, this one is able to remain opened in Acquisition Mode.

In the future, should the hardware used be upgraded, the code might also need updating, in order to allow to fully take advantage of the hardware.

7 | Conclusions

The primary goals of this work have been achieved, both relating to the illumination and camera module and the integration of the new control module with the system.

The module for streaming a live preview of the target to the host computer is operational, allowing perpendicular illumination and with minimal interference on the OCT beam's path. Testing it on live specimens was not possible during the course of this work. Nonetheless, the module is capable of producing images of the target capable of resolving details in the order of approximately 100 μm. It also projects light uniformly with independent control of the illuminated area diameter, perpendicularly to the target, allowing light to cross perfectly through holes smaller of smaller size than 2 mm in the target area of the OCT. At least two of the components will likely need to be replaced in the future, to improve quality. Although it is perfectly possible to preview the target area with reasonable quality as it is, it would not be difficult to improve current conditions by replacing the beamsplitter and the camera. Both can be directly replaced without much extra work. Replacing the beamsplitter for another with a more appropriate bandwidth would improve the lighting by not cutting colors from the light. Similarly, a better camera could benefit the module, by increasing both resolution and overall image quality. The currently used camera was designed as an affordable webcam a few years ago. Currently even similar devices provide far better specifications, so it should not be difficult to improve. However, as stated before, the purpose of the module is not on providing high quality images for scientific purposes, at least for the time being. Its purpose is to provide a practical way to position specimens and improve the process of aiming the OCT toward the desired areas of the target.

The integration of both the new illumination and camera module and the new control module has also been completed. It is now possible to control most relevant aspects of the system from the software on the host computer. This includes the scanning ranges, the acquisition mode, the start and stop of galvanometer movement and the live preview of the target. In addition,

the process of data acquisition was changed to fit the new scanning method provided by the control module and the unforeseen delay when starting the galvanometers.

7.1 Future Work

The first necessity of current iteration of the OCT system is testing with the appropriate specimens. Although the camera works reasonably well in the conditions it was tested in, it needs to be tested with small animals, to find out if the setup is enough to perform visualization of the retinal fundus. The new configuration also needs to have its performance reevaluated, as the intensity of the laser beam has been diminished.

As mentioned, the camera and illumination module would greatly benefit from an appropriate beamsplitter, with 50:50 transmission and reflection for light in the whole visible range, and a better suited camera. This would not require much work, and a new beamsplitter would be an opportunity to improve the alignment of the module even further. As the currently used beamsplitter has a diameter of 50 mm, it does not fit in the current mounting cages available at the OCT lab. Considering that the beamsplitter is the connecting point for the camera, the illumination system, and the rest of the OCT, this means that none of these components are connected between them and thus they need to be independently aligned. Using a smaller beamsplitter in a proper cage mount would allow connecting all the modules, making aligning the components far simpler.

A different, smaller change would be to change the way to control the light intensity in the illumination module. It is currently controlled by a potentiometer which requires a precision screwdriver to change the light intensity. Ideally, this could be done from within the software, to adjust while previewing the resulting image.

One important improvement would be to add the ability to show the scanned area in the preview window. When the OCT components, lenses and distances are stable, it would be possible to implement a way to show the currently scanned area to the user in real time. As mentioned in Chapter 4, without the IR filter, it was possible to observe the laser performing B-Scans or A-Scans in real-time. A more sophisticated approach, that wouldn't be affected by the optical components present in the beam's path, would be to do it in software. A possible process for calibration would be the following: using a fluorescing target, the target would be put in position as if it were the first surface of a sample to be analyzed. With it in position, the laser would be directed to several positions, including the extremities and the center of its

full scanning range. The fluorescing target would allow the positions of the laser on the target to be viewable through the camera. In the host computer's software the association would be made between the current position of the laser as known by the galvanometers and by the camera. This association would be done be identifying the illuminated spots on the target through the camera, by an algorithm that recognized the illuminated spots on the fluorescing target, which then extrapolated to the whole area. After this, by selecting a given scanning range, visual feedback about the given range could be provided on the preview window. It would also be possible to make it so the user could select an area and it would be translated to a scanning range/area.

Regarding the control module, the process for starting, stopping and changing the galvanometer's movement could be improved. As it stands, it works well and it would be difficult to do it differently without significant changes. However, there are two problems with the current process.

The first problem is that it is not intuitive or very practical. The galvanometers need to be stopped to change the scanning ranges or any other parameters. That means the live mode needs to be stopped every time some parameter needs adjustment. The current control mode requires that the galvanometers be stopped and restarted to change the parameters, that is a fact. But the control could be implemented more swiftly. However, that would require significant changes to the software. The software was not designed to account for this control module, and as such, performs in ways that currently are confusing and unnecessarily complicated.

The second problem relates to the communication method, which is not optimal. Currently a command line is called to execute the python scripts by calling the installed python interpreter. This is probably the least efficient way to perform this task. The time needed for the computer to communicate with the module cannot be bypassed, but calling the commands natively in C++ or in embedded python would make the process much faster, as the command line sometimes takes a few seconds to open. Changing this would require one of two things: either translating the code issued by the python scripts to C++ using the appropriate library, or finding/compiling a version of the python library compatible with 64-bit architecture, so that it could be embedded in python directly into the code, avoiding the need for loading the command shell and the python interpreter.

Bibliography

[1] BP Abbott et al. "Observation of gravitational waves from a binary black hole merger". In: *Physical review letters* 116.6 (2016), p. 061102.

[2] *"AFG3000 Series Quick Start User Manual"*.

[3] José Agnelo. "Swept Source Optical Coherence Tomography for Small Animals: System Control and Data Acquisition". MA thesis. University of Coimbra, IBILI, 2013.

[4] OCT Axsun. "Swept Source Engine Operators' Manual (Rev. 09). Axsun Technologies". In: *Inc., Massachusetts, USA* (2010).

[5] Asima Bajwa, Rabia Aman, and Ashvini K Reddy. "A comprehensive review of diagnostic imaging technologies to evaluate the retina and the optic disk". In: *International ophthalmology* 35.5 (2015), pp. 733–755.

[6] Heiner Barfuss and Ernst Brinkmeyer. "Modified optical frequency domain reflectometry with high spatial resolution for components of integrated optic systems". In: *Journal of Lightwave Technology* 7.1 (1989), pp. 3–10.

[7] Barry C Barish and Rainer Weiss. "LIGO and the Detection of Gravitational Waves". In: *Physics Today* 52 (1999), pp. 44–50.

[8] AN Bashkatov et al. "Optical properties of human skin, subcutaneous and mucous tissues in the wavelength range from 400 to 2000 nm". In: *Journal of Physics D: Applied Physics* 38.15 (2005), p. 2543.

[9] João Bernardino. "Swept Source OCT for retinal imaging on small animals: performance, phase stabilization and optical setup". MA thesis. University of Coimbra, IBILI, 2016.

[10] Irving J Bigio and Sergio Fantini. *Quantitative Biomedical Optics: Theory, Methods, and Applications*. Cambridge University Press, 2016.

[11] Brett E Bouma and Guillermo J Tearney. *Handbook of optical coherence tomography*. CRC Press, 2001.

[12] Mark E Brezinski. *Optical coherence tomography: principles and applications*. Academic press, 2006.

[13] Adam P Bruckner. "Picosecond light scattering measurements of cataract microstructure". In: *Applied optics* 17.19 (1978), pp. 3177–3183.

[14] Patrícia Carvalho. "Optical COherence Tomography Layout Simulation Using Matlab®". MA thesis. University of Coimbra, IBILI, 2016.

[15] Barry Cense et al. "Ultrahigh-resolution high-speed retinal imaging using spectral-domain optical coherence tomography". In: *Optics Express* 12.11 (2004), pp. 2435–2447.

[16] SR Chinn, EA Swanson, and JG Fujimoto. "Optical coherence tomography using a frequency-tunable optical source". In: *Optics letters* 22.5 (1997), pp. 340–342.

[17] Michael A Choma et al. "Sensitivity advantage of swept source and Fourier domain optical coherence tomography". In: *Optics express* 11.18 (2003), pp. 2183–2189.

[18] Johannes F De Boer et al. "Improved signal-to-noise ratio in spectral-domain compared with time-domain optical coherence tomography". In: *Optics letters* 28.21 (2003), pp. 2067–2069.

[19] *"Digital Delay / Pulse Generator DG535 Specifications"*.

[20] Wolfgang Drexler et al. "Optical coherence tomography today: speed, contrast, and multimodality". In: *Journal of biomedical optics* 19.7 (2014), pp. 071412–071412.

[21] MA Duguay and AT Mattick. "Ultrahigh speed photography of picosecond light pulses and echoes". In: *Applied optics* 10.9 (1971), pp. 2162–2170.

[22] VF Duma and Adrian G Podoleanu. "Theoretical approach on a galvanometric scanner with an enhanced duty cycle". In: *Proc. SPIE*. Vol. 7139. 2008, p. 71390D.

[23] Wf Eickhoff and Rf Ulrich. "Optical frequency domain reflectometry in single-mode fiber". In: *Applied Physics Letters* 39.9 (1981), pp. 693–695.

[24] Adolf F Fercher et al. "In vivo optical coherence tomography". In: *American journal of ophthalmology* 116.1 (1993), pp. 113–114.

[25] Adolf F Fercher et al. "Optical coherence tomography-principles and applications". In: *Reports on progress in physics* 66.2 (2003), p. 239.

[26] Adolph F Fercher et al. “Measurement of intraocular distances by backscattering spectral interferometry”. In: *Optics Communications* 117.1 (1995), pp. 43–48.

[27] AF Fercher, K Mengedoht, and W Werner. “Eye-length measurement by interferometry with partially coherent light”. In: *Optics letters* 13.3 (1988), pp. 186–188.

[28] J Fujimoto and W Drexler. “Introduction to optical coherence tomography”. In: *Optical coherence tomography*. Springer, 2008, pp. 1–45.

[29] James G Fujimoto et al. “Femtosecond optical ranging in biological systems”. In: *Optics letters* 11.3 (1986), pp. 150–152.

[30] James Fujimoto and Eric Swanson. “The Development, Commercialization, and Impact of Optical Coherence TomographyHistory of Optical Coherence Tomography”. In: *Investigative Ophthalmology & Visual Science* 57.9 (2016), OCT1–OCT13.

[31] JG Fujimoto et al. “High resolution in vivo intra-arterial imaging with optical coherence tomography”. In: *Heart* 82.2 (1999), pp. 128–133.

[32] Ying Geng et al. “Adaptive optics retinal imaging in the living mouse eye”. In: *Biomedical optics express* 3.4 (2012), pp. 715–734.

[33] HH Gilgen et al. “Submillimeter optical reflectometry”. In: *Journal of Lightwave Technology* 7.8 (1989), pp. 1225–1233.

[34] U Glombitza and Ernst Brinkmeyer. “Coherent frequency-domain reflectometry for characterization of single-mode integrated-optical waveguides”. In: *Journal of Lightwave Technology* 11.8 (1993), pp. 1377–1384.

[35] Ireneusz Grulkowski et al. “Retinal, anterior segment and full eye imaging using ultrahigh speed swept source OCT with vertical-cavity surface emitting lasers”. In: *Biomedical optics express* 3.11 (2012), pp. 2733–2751.

[36] E. Hecht. *Optics*. Pearson education. Addison-Wesley, 2002. ISBN: 9780321188786.

[37] Michael R Hee et al. “Optical coherence tomography of age-related macular degeneration and choroidal neovascularization”. In: *Ophthalmology* 103.8 (1996), pp. 1260–1270.

[38] Michael R Hee et al. “Optical coherence tomography of central serous chorioretinopathy”. In: *American journal of ophthalmology* 120.1 (1995), pp. 65–74.

[39] Michael R Hee et al. “Topography of diabetic macular edema with optical coherence tomography”. In: *Ophthalmology* 105.2 (1998), pp. 360–370.

[40] David Huang et al. “Optical coherence tomography”. In: *Science (New York, NY)* 254.5035 (1991), p. 1178.

[41] Robert Huber, Desmond C Adler, and James G Fujimoto. “Buffered Fourier domain mode locking: unidirectional swept laser sources for optical coherence tomography imaging at 370,000 lines/s”. In: *Optics letters* 31.20 (2006), pp. 2975–2977.

[42] Thorlabs Inc. *AL2520M - Ø25 mm S-LAH64 Mounted Aspheric Lens, f=20 mm, NA=0.54, Uncoated*. 2014. URL: https://www.thorlabs.com/thorproduct.cfm?partnumber=AL2520M (visited on 08/14/2017).

[43] Thorlabs Inc. *AL2520M-A - Ø25 mm S-LAH64 Mounted Aspheric Lens, f=20 mm, NA=0.54, ARC: 350-700 nm*. 2015. URL: https://www.thorlabs.com/thorproduct.cfm?partnumber=AL2520M-A (visited on 08/14/2017).

[44] Thorlabs Inc. *DMLP950 - ø1” Longpass Dichroic Mirror, 950 nm Cutoff*. 2014. URL: https://www.thorlabs.com/thorproduct.cfm?partnumber=dmlp950.

[45] Thorlabs Inc. *VRC2D05 - ø1/2” Visible and IR Alignement Disk (400 - 640, 800 - 1700 nm*. 2014. URL: https://www.thorlabs.com/thorproduct.cfm?partnumber=VRC2D05.

[46] JA Izatt and MA Choma. “Theory of optical coherence tomography”. In: *Optical coherence tomography*. Springer, 2008, pp. 47–72.

[47] Joseph A Izatt et al. “Optical coherence tomography and microscopy in gastrointestinal tissues”. In: *IEEE Journal of Selected topics in quantum electronics* 2.4 (1996), pp. 1017–1028.

[48] Steven L Jacques. “Optical properties of biological tissues: a review”. In: *Physics in medicine and biology* 58.11 (2013), R37.

[49] R Leitgeb, CK Hitzenberger, and Adolf F Fercher. “Performance of fourier domain vs. time domain optical coherence tomography”. In: *Optics express* 11.8 (2003), pp. 889–894.

[50] R Leitgeb et al. “Spectral measurement of absorption by spectroscopic frequency-domain optical coherence tomography”. In: *Optics letters* 25.11 (2000), pp. 820–822.

[51] Benjamin M. Potsaid et al. “Ultrahigh speed 1050nm swept source / Fourier domain OCT retinal and anterior segment imaging at 100,000 to 400,000 axial scans per second”. In: 18 (Sept. 2010), pp. 20029–48.

[52] Robert W Massof and Fred W Chang. “A revision of the rat schematic eye”. In: *Vision research* 12.5 (1972), pp. 793–796.

[53] D Merino et al. “Improvement of in vivo en-face OCT retinal images using adaptive optics”. In: *5th International Workshop on Adaptive Optics for Industry and Medicine*. International Society for Optics and Photonics. 2005, pp. 601802–601802.

[54] Albert A Michelson and Edward W Morley. “On the Relative Motion of the Earth and of the Luminiferous Ether”. In: *Sidereal Messenger, vol. 6, pp. 306-310* 6 (1887), pp. 306–310.

[55] *Módulo para controlo do sistema de aquisição de dados do OCT v2.1.*

[56] N Nassif et al. “In vivo high-resolution video-rate spectral-domain optical coherence tomography of the human retina and optic nerve”. In: *Optics express* 12.3 (2004), pp. 367–376.

[57] João Oliveira. “Development of an Optical COherence Tmography for Small Animal Retinal Imaging”. MA thesis. University of Coimbra, IBILI, 2012.

[58] *Optics Guide 5*. Melles Griot, 1990.

[59] Edmund Optics. *20 mm Square IR Cut-Off Filter | Edmund Optics*. 2017. URL: https://www.edmundoptics.com/optics/optical-filters/shortpass-edge-filters/20mm-square-ir-cut-off-filter.

[60] Edmund optics. *Sinusoidal Targets*. 2017. URL: https://www.edmundoptics.com/test-targets/resolution-test-targets/sinusoidal-targets/.

[61] Sergio Ortiz et al. “Optical coherence tomography for quantitative surface topography”. In: *Applied optics* 48.35 (2009), pp. 6708–6715.

[62] *PDB47xC Operation Manual*.

[63] André Pedrosa. “Swept Source Optical Coherence Tomography for Small Animals - Performance Parameters and Optic Modelling”. MA thesis. Univesity of Coimbra, IBILI, 2015.

[64] A Gh Podoleanu. “Optical coherence tomography”. In: *Journal of Microscopy* 247.3 (2012), pp. 209–219.

[65] Scott Prahl. “Optical absorption of water”. In: *Oregon Medical Laser Center* 11 (1998).

[66] Carmen A Puliafito et al. “Imaging of macular diseases with optical coherence tomography”. In: *Ophthalmology* 102.2 (1995), pp. 217–229.

[67] Lukas Reznicek et al. “Megahertz ultra-wide-field swept-source retina optical coherence tomography compared to current existing imaging devices”. In: *Graefe’s Archive for Clinical and Experimental Ophthalmology* 252.6 (June 2014), pp. 1009–1016. ISSN: 1435-702X. DOI: 10.1007/s00417-014-2640-4. URL: https://doi.org/10.1007/s00417-014-2640-4.

[68] João Rodrigues. “Swept Source Optical Coherence Tomography High Rate Acquisition Setup, Image Processing and Paralelism”. MA thesis. Univesity of Coimbra, IBILI, 2013.

[69] Richard B Rosen et al. “En-face flying spot OCT/ophthalmoscope”. In: *Optical Coherence Tomography: Technology and Applications* (2015), pp. 1797–1832.

[70] Joel S Schuman et al. “Optical coherence tomography: a new tool for glaucoma diagnosis.” In: *Current opinion in ophthalmology* 6.2 (1995), pp. 89–95.

[71] David J Segelstein. “The complex refractive index of water”. PhD thesis. University of Missouri–Kansas City, 1981.

[72] Eric A Swanson et al. “In vivo retinal imaging by optical coherence tomography”. In: *Optics letters* 18.21 (1993), pp. 1864–1866.

[73] GJ Tearney et al. “Optical biopsy in human urologic tissue using optical coherence tomography”. In: *The Journal of urology* 157.5 (1997), pp. 1915–1919.

[74] Guillermo J Tearney et al. “In vivo endoscopic optical biopsy with optical coherence tomography”. In: *Science* 276.5321 (1997), pp. 2037–2039.

[75] Peter H Tomlins and RK Wang. “Theory, developments and applications of optical coherence tomography”. In: *Journal of Physics D: Applied Physics* 38.15 (2005), p. 2519.

[76] Valeriĭ Viktorovich Tuchin and V Tuchin. *Tissue optics: light scattering methods and instruments for medical diagnosis*. Vol. 642. SPIE press Bellingham, 2007.

[77] Nuno Viseu. “High Speed Data Acquisition in Swept Source Optical Coherence Tomography”. MA thesis. University of Coimbra, IBILI, 2016.

[78] Julia Welzel et al. “Optical coherence tomography of the human skin”. In: *Journal of the American Academy of Dermatology* 37.6 (1997), pp. 958–963.

[79] Wolfgang Wieser et al. “Multi-megahertz OCT: High quality 3D imaging at 20 million A-scans and 4.5 GVoxels per second”. In: *Optics express* 18.14 (2010), pp. 14685–14704.

[80] Maciej Wojtkowski et al. “In vivo human retinal imaging by Fourier domain optical coherence tomography”. In: *Journal of biomedical optics* 7.3 (2002), pp. 457–463.

[81] Maciej Wojtkowski et al. “Ultrahigh-resolution, high-speed, Fourier domain optical coherence tomography and methods for dispersion compensation”. In: *Optics express* 12.11 (2004), pp. 2404–2422.

[82] *X5-400M Users's Manual*.

[83] S Yun et al. “High-speed optical frequency-domain imaging”. In: *Optics express* 11.22 (2003), pp. 2953–2963.